

Structure of potassium isotopes studied with collinear laser spectroscopy

CERN-THESIS-2015-235
01/04/2015



Jasna Papuga

Dissertation presented in partial
fulfillment of the requirements for the
degree of Doctor in Science

April 2015

Structure of potassium isotopes studied with collinear laser spectroscopy

Jasna PAPUGA

Examination committee:

Prof. dr. M. Huyse, chair

Prof. dr. G. Neyens, supervisor

Prof. dr. R. Raabe

Prof. dr. N. Severijns

Prof. dr. P. Van Duppen

Prof. dr. A. Vantomme

Prof. dr. K. Blaum

(Max-Planck-Institute for Nuclear Physics,
Heidelberg, Germany)

Dissertation presented in partial
fulfillment of the requirements for
the degree of Doctor
in Science

April 2015

© 2015 KU Leuven – Faculty of Science
Uitgegeven in eigen beheer, Jasna Papuga, Celestijnenlaan 200D box 2418, 3001 Leuven (Belgium)

Alle rechten voorbehouden. Niets uit deze uitgave mag worden vermenigvuldigd en/of openbaar gemaakt worden door middel van druk, fotokopie, microfilm, elektronisch of op welke andere wijze ook zonder voorafgaande schriftelijke toestemming van de uitgever.

All rights reserved. No part of the publication may be reproduced in any form by print, photoprint, microfilm, electronic or any other means without written permission from the publisher.

Preface

This thesis is based on the data from the potassium campaign performed at the collinear laser spectroscopy set-up at ISOLDE (CERN). The aim of these studies was the investigation of the nuclear structure of the neutron-rich potassium isotopes beyond $N = 28$, by measuring their nuclear spin, magnetic moment and mean square charge radius. The analysis of the data yielded firmly assigned ground-state spins for the neutron-rich $^{48-51}\text{K}$ isotopes. Their magnetic moments have been compared to large-scale shell-model calculations, and a good agreement has been observed for all isotopes from ^{38}K up to ^{51}K . A detailed discussion of the composition of the wave function as a function of neutron number has been performed. The measured optical isotope shifts relative to ^{47}K allowed us to deduce the change in the difference in mean square charge radii and extend the information towards $N = 32$. Finally, the direct measurement of the isomer shift in ^{38}K revealed a significant difference in the mean square charge radius of its two long-lived states. The results were discussed and published in four articles. Three of them form the core of this thesis, while the article discussing the nuclear radii is included in the Appendix.

- **Spins and Magnetic Moments of ^{49}K and ^{51}K : establishing the $1/2^+$ and $3/2^+$ level ordering beyond $N = 28$**
J. Papuga, M. L. Bissell, K. Kreim, K. Blaum, B. A. Brown, M. De Rydt, R. F. Garcia Ruiz, H. Heylen, M. Kowalska, R. Neugart, G. Neyens, W. Nörtershäuser, T. Otsuka, M. M. Rajabali, R. Sánchez, Y. Utsuno and D. T. Yordanov
Physical Review Letters **110**, 172505 (2013)
- **Shell structure of potassium isotopes deduced from their magnetic moments**
J. Papuga, M. L. Bissell, K. Kreim, C. Barbieri, K. Blaum, M. De Rydt, T. Duguet, R. F. Garcia Ruiz, H. Heylen, M. Kowalska, R. Neugart, G. Neyens, W. Nörtershäuser, M. M. Rajabali, R. Sánchez, N. Smirnova, V.

Somà and D. T. Yordanov
Physical Review C **90**, 034321 (2014)

- **Proton-Neutron Pairing Correlations in the Self-Conjugate Nucleus ^{38}K Probed via a Direct Measurement of the Isomer Shift**

M. L. Bissell, J. Papuga, K. Kreim, K. Blaum, M. De Rydt, R. F. Garcia Ruiz, H. Heylen, M. Kowalska, R. Neugart, G. Neyens, W. Nörtershäuser, F. Nowacki, M. M. Rajabali, R. Sánchez, K. Sieja and D. T. Yordanov
Physical Review Letters **113**, 052502 (2014)

The thesis is structured in six chapters. Chapter 1 starts with the introduction to the shell model, which plays a crucial role in the motivation and the discussion. The overview of the potassium region and the motivation for our work is also presented in the same chapter. Theory of the nuclear moments and radii together with the atomic hyperfine structure are described in Chapter 2. In Chapter 3, the experimental set-up, analysis and the final results are presented. Chapter 4 is based on two articles focusing on the discussion of the evolution of the $\pi(2s_{1/2} - 1d_{3/2})$ gap and the configuration of the ground-state wave functions in the potassium isotopic chain. Additionally, details about the shell-model calculations are given. The article about the direct measurements of the isomer shift in ^{38}K is presented as a separate discussion in Chapter 5. The thesis ends with a summary and conclusions in Chapter 6.

Our results for nuclear radii in the form of an article are included in Appendix A.

- **Nuclear charge radii of potassium isotopes beyond $N = 28$**
K. Kreim, M. L. Bissell, J. Papuga, K. Blaum, M. De Rydt, R. F. Garcia Ruiz, S. Goriely, H. Heylen, M. Kowalska, R. Neugart, G. Neyens, W. Nörtershäuser, M. M. Rajabali, R. Sánchez Alarcón, H. H. Stroke and D. T. Yordanov
Physics Letters B **731** (2014) 97-102

Abstract

By exploring the structure of different nuclei, one can learn about the interaction between the nucleons, their building blocks. In this field of research, there is a strong interplay between experiment and theory. In particular, theory has a crucial role in the interpretation of the experimental results, while new experimental results provide testing ground and directions for theorists. In the light- and mid-mass regions of the nuclear chart, the shell model is very successful and widely used for calculations of the ground- as well as excited-states properties. It is based on associated larger energy gaps between single particle energy levels for isotopes with certain proton (Z) and neutron (N) numbers, which are called "magic numbers". It was believed that these numbers (8, 20, 28,...) are preserved for all nuclei throughout the nuclear chart. However, during the last decades studies of the isotopes with an unbalanced number of protons and neutrons revealed that in these isotopes the shell gaps could change when compared to the stable isotopes. This effect is known as the shell evolution.

In general, the potassium isotopes with 19 protons are excellent probes for the shell-model theory. In the region below Ca ($Z < 20$), the inversion of the ground- and the first-excited states ($3/2^+$ and $1/2^+$, respectively) for isotopes with $20 \leq N \leq 28$ was discovered. In the Cl chain ($Z = 17$), it happens at $N = 24$, while for K isotopes, the inversion takes place at $N = 28$. This has drawn appreciable attention in the last decade from both experimentalists and theorists. The effect is the consequence of the degeneracy (or even inversion) of the $\pi 2s_{1/2}$ and $\pi 1d_{3/2}$ orbitals when the $\nu 1f_{7/2}$ orbit is being filled. "What will happen with this particular gap when the next neutron orbit, $\nu 2p_{3/2}$, is being filled?" and "What are the forces responsible for this?" were open questions which we addressed in our studies.

The experiment was carried out on the COLLAPS beam-line located at CERN-ISOLDE, where collinear laser spectroscopy was performed on a bunched beam of the radioactive K atoms. The hyperfine structure of the potassium isotopes

from $N = 19$ up to $N = 32$ was measured and the analysis yielded the nuclear spins, magnetic moments and the mean square charge radii. In addition, shell-model calculations with different effective interactions were carried out, where only one of them predicted the correct ground-state spin for ^{49}K ($I = 1/2$) and all agreed for ^{51}K ($I = 3/2$). The evolution of the $\pi(2s_{3/2} - 1d_{3/2})$ gap was investigated in more detail using the spin-tensor decomposition method. Moreover, the evolution of the energy gap was also investigated using *ab initio* calculations where $3N$ forces were included. The obtained results are in a reasonable agreement with experimental data, considering the fact that this interaction was fitted only to data up to mass $A = 4$.

Magnetic moments (g factors) are sensitive to the occupation of particular single particle orbits and the configuration of the wave function. Thus, the discussion based on the comparison between the experimental results and the shell-model calculations is reported. It is shown that only ^{48}K and ^{49}K have a more fragmented ground-state wave function. Additionally, the ground-state spin of $^{48,50}\text{K}$ was established firmly for the first time, to be $I = 1$ and $I = 0$, respectively.

The directly measured isomer shift between the ground state ($I^\pi = 3^+$) and isomeric state ($I^\pi = 0^+$) in ^{38}K resulted in a significant difference in the mean square charge radius, contradicting the previous conclusion based on an indirect measurement. The shell-model calculations, which accounted for the excitation of protons and neutrons across Z and $N = 20$ shell gaps, were performed in order to support the intuitive interpretation of this increase of the charge radius.

Beknopte samenvatting

Door de structuur van verschillende kernen te bestuderen kunnen we vanalles leren over de interactie tussen de nucleonen, de bouwstenen van de kern. Dit vereist een sterke wisselwerking tussen experiment en theorie. Theorie is vaak essentieel voor de interpretatie van experimentele resultaten en omgekeerd bieden experimentele resultaten een testbank voor modellen en wijzen ze de weg voor verbeteringen en uitbreidingen van de theorieën. Een voorbeeld van een succesvol en veel gebruikt model is het schillemenmodel. Dit model kan worden gebruikt om eigenschappen van de grond- en geëxciteerde toestanden te berekenen in het licht- en mediummassagebied van de kernkaart. De basis voor dit model zijn de grote energiekloven tussen de eendeeltjesenergieën voor sommige proton- (Z) en neutrongetallen (N), ook wel magische getallen genoemd. Men veronderstelde dat deze getallen (8, 20, 28, ...) dezelfde zouden zijn over de gehele kernkaart. In de laatste decennia is het echter duidelijk geworden dat de magische getallen verschillen voor kernen dicht bij stabiliteit vergeleken met de zogeheten exotische kernen, kernen met een onevenwicht tussen het aantal protonen en neutronen. Deze observatie is ook gekend als schillenevolutie.

Kaliumisotopen hebben 19 protonen en bieden goede mogelijkheden om het schilllemenmodel te toetsen. Ze behoren immers tot het gebied ten zuiden van Ca ($Z < 20$) waar een inversie van grond- en eerste geëxciteerde toestand (respectievelijk spin $3/2^+$ en $1/2^+$) is waargenomen voor kernen met $20 < N < 28$. In de Cl-keten ($Z = 17$) gebeurt deze inversie bij $N = 24$, dit in tegenstelling tot de K-keten waar men zoiets pas ziet bij $N = 28$. Deze observatie heeft de laatste decennia de aandacht getrokken van zowel experimentele als theoretische fysici. Een verklaring voor de inversie kan gevonden worden in de ontaardheid (of zelfs inversie) van de proton $2s_{1/2}$ en $1d_{3/2}$ orbitalen wanneer het neutron $1f_{7/2}$ orbitaal wordt gevuld. Wat er zou gebeuren wanneer het volgende neutron orbitaal, $p_{3/2}$, zou worden gevuld was echter onduidelijk. Ook de precieze krachten verantwoordelijk voor de inversie waren onbekend. Het onderzoek in deze thesis houdt zich dan ook bezig met deze vragen.

Het experiment vond plaats aan de COLLAPS bundellijn in CERN-ISOLDE, waar collineaire laserspectroscopie op gepulste bundels radioactieve K-atomen is uitgevoerd. De hyperfijnstructuur van de kaliumisotopen van $N = 19$ tot en met $N = 32$ werd opgemeten en uit de analyse volgden de kernspins, magnetische momenten en de gemiddelde kwadratische ladingssstralen. Verder werden ook schillenmodelberekeningen uitgevoerd met verscheidene effectieve interacties. Deze slaagden er allemaal in om de spin van de ^{51}K grondtoestand correct als $I = 3/2$ te voorspellen, maar de $I = 1/2$ grondtoestand van ^{49}K werd slechts door 1 interactie succesvol berekend. De evolutie van de proton ($s_{1/2}$ - $d_{3/2}$) energieën werd in meer detail onderzocht door gebruik te maken van de spin-tensordecompositie methode. Daarboven werd het verloop van het energieverlieschil ook bestudeerd aan de hand van ab initio berekeningen waar $3N$ krachten in rekening werden gebracht. De overeenkomst tussen de voorspelling van deze laatste interactie en de experimentele resultaten zijn verrassend goed, aangezien alleen kernen tot en met $A = 4$ zijn gebruikt om modelparameters te fitten.

Magnetische momenten (g factoren) zijn gevoelig voor de exacte bezetting van de één-deeltjesorbitalen en de samenstelling van de golffunctie. Dit biedt een uitstekende kans om deze experimentele observabelen te vergelijken met de schillenmodelberekeningen. In de discussie werd aangetoond dat de golffuncties van de hele gemeten kaliumreeks puur zijn met uitzondering van ^{48}K en ^{49}K waarvoor de golffunctie gefragmenteerd is. Verder zijn voor het eerst met zekerheid de grondtoestandspins toegekend voor $^{48,50}\text{K}$, respectievelijk $I = 1$ en $I = 0$.

De direct gemeten isomeerverschuiving tussen de grondtoestand ($I^\pi = 3^+$) en de isomere toestand in ^{38}K toont aan dat er significant verschil is in gemiddelde kwadratische ladingssstraal, in tegenspraak met een eerdere conclusie gebaseerd op indirect metingen. Om een intuïtieve interpretatie van deze toename in ladingssstraal te ondersteunen, werden schillenmodelberekeningen uitgevoerd die excitaties van protonen en neutronen over $Z = 20$ en $N = 20$ toelieten. Deze bevestigen dat een verhoogd aantal proton-neutron correlaties in de 0^+ isomeer aan de basis ligt van de grotere ladingssstraal.

Contents

Preface	i
Abstract	iii
Beknopte samenvatting	v
Contents	vii
1 Motivation	1
1.1 The nuclear shell model	1
1.2 Shell evolution: Island of inversion	6
1.3 The region of potassium isotopes	8
1.4 Evolution of π ($1d_{3/2} - 2s_{1/2}$)	11
2 Measurements of nuclear moments and charge radii	15
2.1 Nuclear moments	15
2.1.1 Magnetic dipole moment	16
2.1.2 Electric quadrupole moment	17
2.1.3 The Mean Square Charge Radius	20
2.2 Atomic Hyperfine Structure	21
2.2.1 Magnetic dipole hyperfine parameter	21

2.2.2	Electric quadrupole hyperfine parameter	22
2.2.3	Isotope shift	24
3	Experimental results	29
3.1	The ISOLDE facility	29
3.2	Collinear laser spectroscopy beam line	30
3.2.1	Basic ideas	30
3.2.2	COLLAPS beam line	32
3.2.3	Conversion of raw data	36
3.2.4	Voltage calibration	39
3.3	Line shape of the fitting	40
3.4	Results from the two experiments	42
3.5	$I = 0$ spectra	49
3.6	Systematic uncertainties	51
3.7	Hyperfine structure anomaly	52
4	Nuclear structure of potassium isotopes based on spins and magnetic moments	59
4.1	Monopole interaction	59
4.2	Large-scale shell-model calculations	62
4.2.1	Spin-tensor decomposition	67
4.3	Article I	71
4.4	Article II	84
5	Isomer shift in ^{38}K	113
5.1	Article III	113
6	Conclusion	127

A Radii of potassium isotopes beyond $N = 28$	131
A.1 Article IV	131
A.2 Unpublished results - Mean square charge radii of $^{48,51}\text{K}$ for different spins	145
B Multiple Voigt line shape	147
C Additional spectra	149
D Shell-model calculation	151
D.1 Centroids	151
D.2 Wave function configuration	152
Bibliography	157

Chapter 1

Motivation

The atomic nucleus has a complex structure consisting of protons and neutrons. Within the shell model it can be described as individual nucleons moving in the potential which they create. An exact solution to this many-body problem involving the strong nuclear force is not existing to date, but several semi-empirical models exist. Experimental studies of the nuclear structure in different regions of the nuclear chart provide input for improvements and testing of those nuclear models. However, besides the descriptive power of these theoretical models, one also requires predictive power. Thus, theorists use the experimental results as test for their model and to re-tune eventually some fit parameters.

One of the most successful nuclear models for low and medium mass nuclei is the shell model. Due to its crucial role in the motivation and the discussion of results from this thesis, a brief introduction of the concept will be given here. In addition, an overview of the ground state properties already known for potassium isotopes together with the open questions will be presented as well.

1.1 The nuclear shell model

Based on experimental evidences such as the excitation energy of the first-excited 2^+ state in even-even nuclei shown in Fig. 1.1, the shell structure of the nuclei was proposed by M. Goeppert-Mayer [1] in parallel with Haxel and co-workers [2] in the beginning of the 1950's. The model was called the nuclear shell model and it was based on the assumption that the protons and neutrons

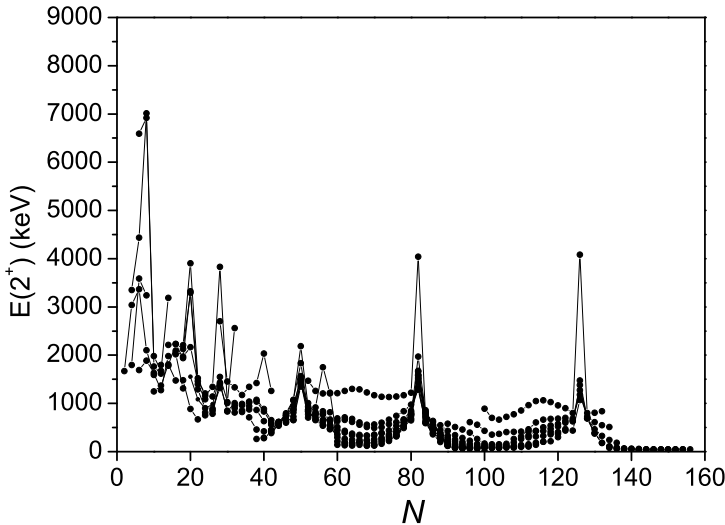


Figure 1.1: Systematics of the excitation energy of the first-excited 2^+ state in even-even nuclei ($2 \leq Z \leq 100$). Clear indication of the shell gaps at $N = 8, 20, 28, 50, 82$ and 126 is obtained. Data taken from [3].

in such nuclei that are difficult to excite, are filling quantum orbitals from which it is difficult to excite a nucleon to the next level, such that these nuclei are more stable.

The Hamiltonian which describes a system of A independent particles can be expressed as [4]

$$H = \sum_{i=1}^A T_i + \frac{1}{2} \sum_{i,j} V_{ij}(\mathbf{r}_i - \mathbf{r}_j), \quad (1.1)$$

where T_i is the kinetic energy of the i^{th} nucleon and $V_{ij}(\mathbf{r}_i - \mathbf{r}_j)$ is a two-body interaction between the i^{th} and j^{th} nucleon. Due to the unknown form of the two-body nucleon-nucleon interaction, solving the Schrödinger equation for the Hamiltonian defined in Eq. (1.1) is impossible. Thus, one rewrites the Hamiltonian in such way that the nucleon-nucleon interaction is replaced by the average potential field induced by all nucleons, and the remaining term (H_{res}) is considered as a perturbation to this mean-field interaction. The Hamiltonian

can thus be written as

$$H = \underbrace{\sum_{i=1}^A (T_i + U(\mathbf{r}_i))}_{H_0} + \underbrace{\left(\sum_{i>j=1}^A V_{ij}(\mathbf{r}_i - \mathbf{r}_j) - \sum_{i=1}^A U(\mathbf{r}_i) \right)}_{H_{\text{res}}}, \quad (1.2)$$

where the first sum is defined as H_0 and depicts a nucleus where each individual nucleon orbits independently in the common mean-field potential $U(\mathbf{r})$, while the second sum labeled with H_{res} is called the residual interaction and represents a small perturbation on H_0 . The $U(\mathbf{r})$ term is a one-body potential common for all nucleons.

In what follows, the motion of an independent nucleon in the nuclear potential will be briefly discussed. A good approximation for the mean-field potential is the Woods-Saxon (W.S.) potential, which is expressed as a function of the distance from the nuclear center [5]:

$$U_{\text{W.S.}}(\mathbf{r}) = \frac{U_0}{1 + e^{\frac{r-R}{a}}}, \quad (1.3)$$

where U_0 is depth of the potential well, $R = r_0 A^{1/3} = 1.25 A^{1/3}$ is the nuclear radius and a is a diffuseness parameter. However, with this potential there is only a numerical solution to the Schrödinger equation, but not analytical. Therefore, a harmonic oscillator (H.O.) potential, which allows an analytical solution of the Schrödinger equation, will be considered in the rest of the text. It is defined as

$$U_{\text{H.O.}}(\mathbf{r}) = U(\mathbf{r}) = \frac{1}{2} m \omega^2 r^2 \quad (1.4)$$

where m is the nucleon mass, ω represents the oscillator frequency and r is the distance from the center of the nucleus. Both potentials are shown in Fig. 1.2

Solving the Schrödinger equation for the case where H_{res} is neglected, the energy eigenvalues can be obtained as [4]:

$$E_0 = \hbar \omega \left(N + \frac{3}{2} \right) = \hbar \omega \left(2n + l - \frac{1}{2} \right) \quad (1.5)$$

where $N = 0, 1, 2, \dots$ is the major oscillator quantum number and l is the orbital quantum number taking values from $N, N-2, \dots, 1$ or 0 . The notation for the orbits with different l are as follows: $l = 0, 1, 2, 3, 4, \dots$ correspond to s, d, p, f, \dots . The last parameter is $n = \frac{N-l+2}{2}$ which represents the number of nodes of the wave function. The schematic representation of the single-particle energies of the harmonic oscillator are presented in Fig. 1.3 (left side).

However, the agreement with the experimental data was not satisfying, because only the first three major shell gaps (at Z or $N = 2, 8$ and 20) were reproduced.

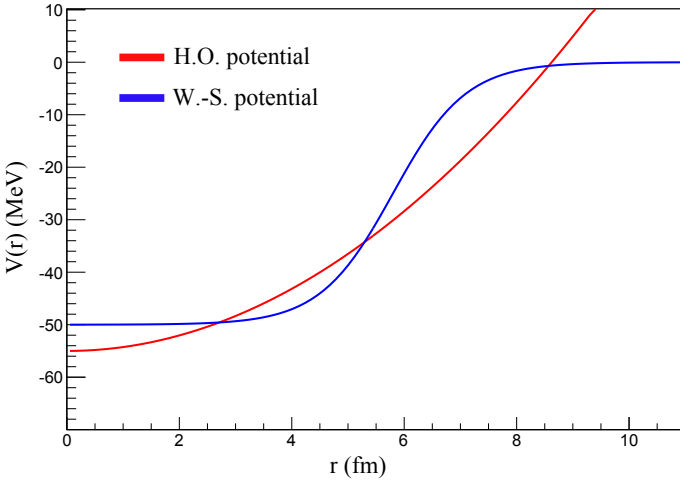


Figure 1.2: The harmonic oscillator (red line) and the Woods-Saxon potential (blue line). Adapted from [5].

In order to obtain better agreement, two additional terms were added. The first term is l^2 which breaks the degeneracy for $\Delta l = -2\Delta n$ [6]. Its attractive influence is more pronounced for the particle with higher l , thus it lowers the energy of these levels. This is depicted in Fig. 1.3 (middle). The second term is the spin-orbit term ($\mathbf{l} \cdot \mathbf{s}$), which splits the orbits according to the relative orientation between the orbital angular momentum and the intrinsic spin as $\mathbf{j} = \mathbf{l} \pm \mathbf{s}$ producing more bound states with the parallel alignment. This is shown in Fig. 1.3 (right). The energy gap at $Z, N = 28$ is the first gap arising due to the spin-orbit term.

The final form of the potential is given by:

$$U(\mathbf{r}) = \frac{1}{2}m\omega^2r^2 + \alpha l^2 + \beta \mathbf{l} \cdot \mathbf{s}. \quad (1.6)$$

Using this potential, the concept of the shell structure of nuclei was also theoretically explained by two independent works, M. Goeppert Mayer [1, 7] and O. Haxel and co-authors [2]. By introducing a spin-orbit term next to the harmonic oscillator potential, they were able to reproduce the experimentally observed numbers related to the larger energy gaps between the orbitals. These particular numbers are 2, 8, 20, 28, 50, 82 and 126, and they were called "magic numbers".

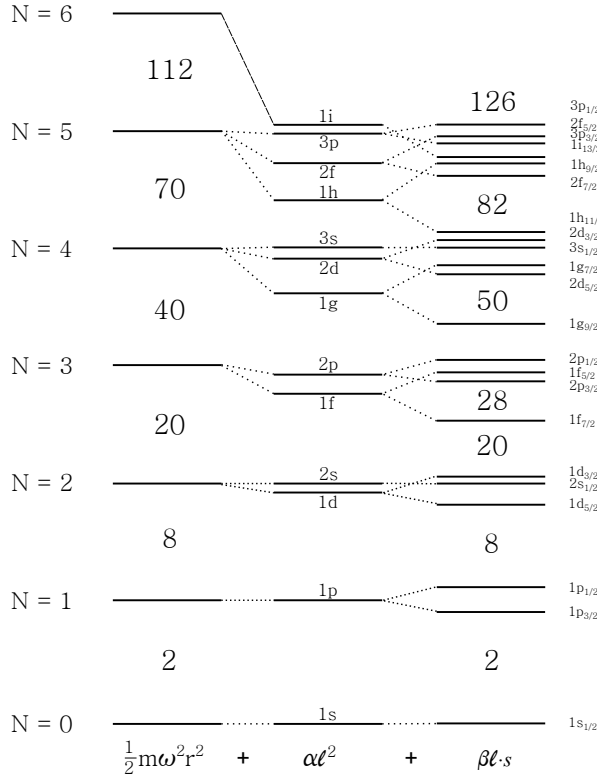


Figure 1.3: Schematic representation of the evolution of the single-particle levels for different terms included. Starting from only harmonic oscillator potential, then a l^2 term is added and finally, a spin-orbit term is also included. The figure is adapted from [6].

For the next few decades, it was believed that magic numbers are the same in all nuclei¹, irrespective of their proton-to-neutron ratio. The development of new facilities where radioactive beams with larger N/Z ratios and shorter half-lives were produced, enabled the study of more exotic nuclei. These studies have shown that the original magic numbers were not preserved in regions far from stability. In addition, new shell closures appeared. At that point, a new quest for experimentalists as well as theorists was established where the goal was to answer the question: What drives the shell evolution?

¹It should be noticed that M. Goeppert Mayer in her work from 1949 already suggested that Z or N equal 14 could provide extra stability, which would imply change of the original "magic numbers".

In order to investigate the nuclear shell structure, one should look into the detailed information that can be derived from certain experimental observables which are measured with high precision. Different techniques yield different observables which can be incorporated into one complete picture. For example, mass measurements give insight into the proton or neutron separation energy, which after the closed shell decreases drastically, pointing to the presence of a less bound nucleon in the next orbit. Another parameter is the energy of the first 2^+ state and the transition strength towards it, often denoted in literature as $E(2^+)$ and $B(E2 : 0^+ \rightarrow 2^+)$, respectively. The difference in the mean square charge radii $\delta\langle r^2 \rangle$ is another observable related to the size of nuclei in an isotopic chain. The decrease of $\langle r^2 \rangle$ is expected at a closed shell and experiments revealed a steep increase in the isotopes beyond a closed shell. Furthermore, based on the experimental magnetic moments, the configuration of the wave function of the particular state can be derived by comparing to large-scale shell-model calculations. Quadrupole moments can reveal an onset of collectivity related to correlations between nucleons. An extensive overview of this topic can be found in Ref. [8].

1.2 Shell evolution: Island of inversion

The effect of the changes in the nuclear structure which result in a disappearance of the standard shell closures and the appearance of new ones, is called the shell evolution. The first indication that this effect exists, appeared around the $N = 20$ region. In what follows, more details related to that particular shell gap will be presented. We will not go into the details of the experimental techniques nor the theory behind the observed shell evolution, but rather give an intuitive explanation which will help to understand similar effects occurring in other regions of the nuclear chart.

The $N = 20$ shell gap is created between the $\nu 1d_{3/2}$ and $\nu 1f_{7/2}$ neutron orbits (see Fig. 1.3), thus below is the *sd* shell with positive parity orbits and above is the *fp* shell with the opposite parity. It is the last magic number which can be obtained by simply using the harmonic oscillator for the potential.

The first two isotopes where the reduction of the $N = 20$ gap was found, were ^{31}Na ($Z = 11$) and ^{32}Mg ($Z = 12$). For these isotopes, unexpected spectroscopic information was obtained, not consistent with the presence of a magic number of 20 neutrons: the ground-state spin of ^{31}Na was determined to be $3/2$ [9] and a low excitation energy of the lowest 2^+ state in ^{32}Mg was observed [10]. In the shell-model framework, these effects were explained by Poves and Retamosa who used the $\pi 1d_{5/2}^{Z-8} \otimes \nu 1d_{3/2}^{N-18}(1f_{7/2}2p_{3/2})^2$ orbitals in the valence space of their

calculations [11], thus allowing to produce 2^+ states by exciting two neutrons across the $N = 20$ shell gap. By then assuming a smaller $N = 20$ shell gap, they were able to reproduce the experimental data. The smaller gap means that less energy is needed for the excitation of a neutron, and because at least two neutrons need to be excited (due to the parity change), these particle-hole excitations lead to additional correlations and deformation. Thus, although a significant amount of the energy is required to promote 2 neutrons from the sd into fp orbitals ($2E_{N=20}$), this will be counterbalanced with the correlation energy which is gained after the excitation [12]. Due to the fact that the leading component in the ground-state wave function originates from the intruder ($fp; 2p - 2h$) instead of the normal ($sd; 0p - 0h$) configuration, this region is called "Island of inversion" [13].

Mapping of the "island" via systematic studies showed that this region is around isotopes with $8 < Z < 14$ and $N = 20$. In Fig. 1.4 the experimental excitation energy of the 2_1^+ state together with the $B(E2 : 0^+ \rightarrow 2^+)$ for even-even $N = 20$ isotones with $10 \leq Z \leq 22$ are presented (data are taken from [14] and [3]).

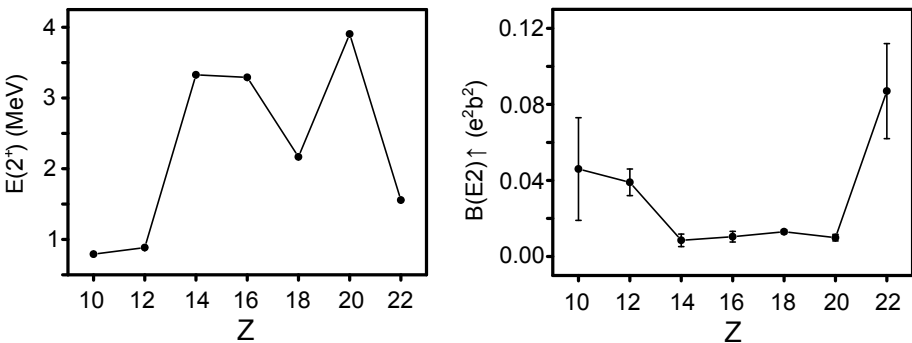


Figure 1.4: Excitation energies of the first-excited 2^+ states and the transition probabilities for $N = 20$ even-even isotones with $10 \leq Z \leq 22$. Data taken from [14] and [3].

Based on the high $E(2^+)$ and low $B(E2 : 0^+ \rightarrow 2^+)$, it is clear that the $N = 20$ shell gap is strong in the region where protons occupy the $2s_{1/2}$ and $1d_{3/2}$ orbitals corresponding to the isotopes between ^{34}Si ($Z = 14$) and ^{40}Ca ($Z = 20$).

However, in the case where there are only 2 or 4 protons located in the $\pi 1d_{5/2}$ orbital, the situation drastically changes. The 2^+ state is found to be at 792 (4) keV [15] and 885.7 (20) keV [10] in ^{30}Ne ($Z = 10$) and ^{32}Mg ($Z = 12$), respectively. The increase in $B(E2 : 0^+ \rightarrow 2^+)$ for these two isotopes points to the occupation of $\nu(fp)$ orbitals [12].

What causes such strong changes in the nuclear structure? It is the proton-neutron interaction which is maximal between the orbits where $\Delta n = 0$ and $\Delta l = 0$ due to the large spacial overlap between these orbitals [16]. This interaction also depends on the occupation of the orbits. Thus, for the spin-orbit partners, namely $\pi 1d_{5/2}$ and $\nu 1d_{3/2}$, this interaction is dominant for ^{10}Ne , ^{11}Na and ^{12}Mg isotopes with neutron numbers around $N = 20$. Due to the strong attractive interaction between these orbits, the $\nu 1d_{3/2}$ orbital gets less bound when the $\pi 1d_{5/2}$ orbit is emptied from Al ($Z = 13$) down to F ($Z = 9$). Thus the $N = 20$ gap is reduced in this region, allowing more easily excitations of neutrons into the pf shell. At the same time, a new shell gap at $N = 16$ is created for isotopes with $Z < 13$. This effect is depicted in Fig. 1.5.

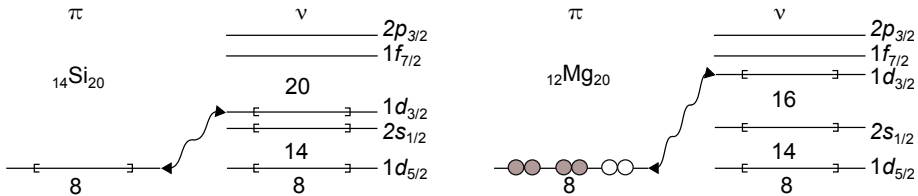


Figure 1.5: Structure of ^{34}Si and ^{32}Mg as an example of shell evolution due to the proton-neutron interaction, where the classical $N = 20$ gap disappeared and $N = 16$ appeared as a new shell gap.

A systematic investigation of the exotic nuclei from this region via various experimental observables together with the development of the nuclear theory led to the solution of the mystery around $N = 20$ as well as to the better understanding of the proton-neutron interaction. In addition, in different parts of the nuclear chart, other unexpected features were revealed, caused by a similar mechanism. For example, the weakening of the $N = 28$ shell gap for $Z < 20$ isotopes, where in $^{42,44}\text{S}$ ($Z = 16$) a more collective character than expected was determined [17, 18], or even disappearance of the same gap in ^{42}Si ($Z = 14$) [19]; in ^{75}Cu ($Z = 29$) the inversion between the $\pi 1f_{5/2}$ and $\pi 2p_{3/2}$ was obtained [20], etc. A detailed review can be found in Ref. [8].

1.3 The region of potassium isotopes

The 19 protons in the potassium isotopes occupy the πsd shell, leaving one hole with respect to $Z = 20$, whilst the neutrons are located in the $1d_{3/2}, 1f_{7/2}, 2p_{3/2}$ orbit (Fig 1.6).

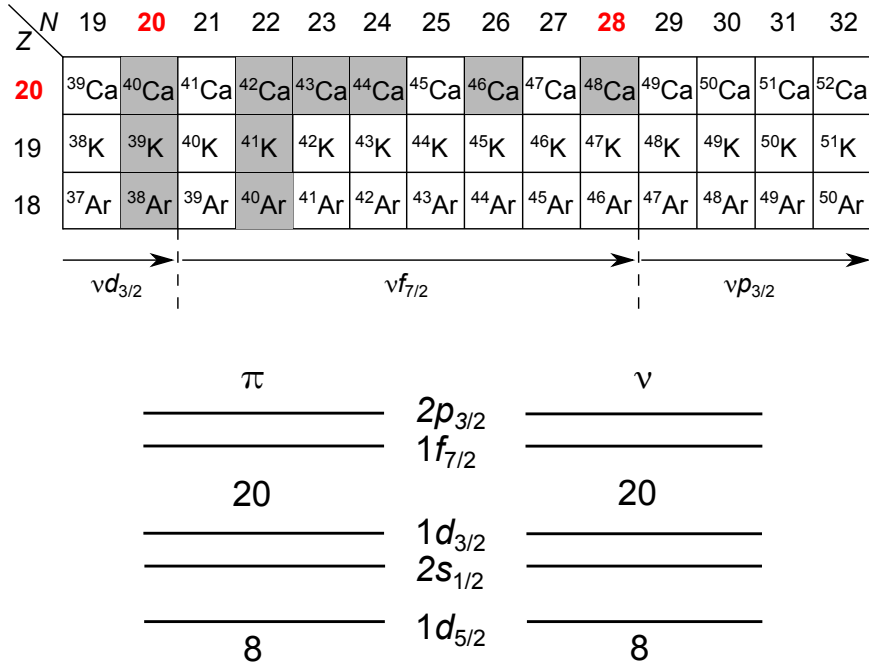


Figure 1.6: (Upper panel) Potassium isotopes ($Z = 19$) together with the Ar ($Z = 18$) and Ca ($Z = 20$) from the same region ($19 \leq N \leq 32$). Suitable neutron orbits are marked as well. Stable isotopes are indicated by gray boxes. (Lower panel) The same region in the shell model framework.

Although these isotopes are excellent probes for the nuclear theories, not much spectroscopic information is known about the neutron-rich isotopes with $N > 28$.

In the case of odd- A K isotopes, the nuclear spin originates from a hole in the πsd shell, while the even number of neutrons are coupled to zero spin (in a shell model interpretation where particles tend to appear in pairs of zero spin). For isotopes with $N \leq 26$, the nuclear spins and parities of the ground states were firmly assigned to be $I^\pi = 3/2^+$, which corresponds to the expected value due to the hole in the $\pi 1d_{3/2}$ orbit. In addition, the spin/parity of the first-excited states were determined to be $I^\pi = 1/2^+$ and their excitation energies were found to strongly decrease from ^{39}K to ^{45}K [21, 22, 23]. The determination of the flipped nuclear spins of the ground- and first-excited state in ^{47}K revealed interesting features in the neutron-rich potassium isotopes [23]. For $^{49,51}\text{K}$ conflicting data for the ground-state spin were published. From β -decay studies of ^{49}K to ^{49}Ca , a spin/parity for the ground-state was suggested to be $(3/2^+)$ [24]. In contrast to that, more recent results from in-beam γ

spectroscopy using deep-inelastic transfer reactions favor $(1/2^+)$ [25]. In the latter, a quite extensive level scheme of ^{49}K was proposed, but all the spins were only tentatively assigned, due to not having a firm ground state spin assignment. For ^{51}K , Perrot *et al.* [26] proposed $I^\pi = (3/2^+)$ based on β -decay studies and no excited states were obtained to date. In general, the spin of $3/2$ arises from a hole in $\pi 1d_{3/2}$ and spin $1/2$ originates from a hole in $\pi 2s_{1/2}$. States have positive parity inherited from the positive parities of πsd orbitals.

For even- A potassium isotopes, the situation is more complex due to the coupling between the odd-proton and the odd-neutron which gives a larger number of possible spins and a high density of low lying states. A ground-state spin/parity of 3^+ and 4^- was measured for ^{38}K and ^{40}K , respectively [14]. A nuclear spin/parity of $I^\pi = 2^-$ was determined for $^{42,44,46}\text{K}$ [14]. Similarly to the odd- A neutron-rich isotopes, conflicting results for spins of $^{48,50}\text{K}$ were published. In particular, the spin $I = 2$ was assigned from β -decay studies where ^{48}K was produced in $\text{Ca}(n, p)$ reaction [27]. More recent data from deep-inelastic transfer reactions suggested a spin/parity $I^\pi = 1^-$ [28]. ^{50}K was investigated via β -decay studies, yielding different results, $I^\pi = 0^-$ in Ref. [29] and in a more recent publication $I^\pi = 1^-$ [30]. For these isotopes, the positive parity states arise from the coupling of an odd-proton and an odd-neutron from the sd orbitals (^{38}K). In contrast to that, an unpaired neutron occupying the fp orbits and coupling to a proton in the sd orbits yields states of negative parity .

In addition, the difference in mean square charge radii, $\langle r^2 \rangle$, were known from ^{37}K up to ^{47}K [31, 32]. By measuring the hyperfine structure for the exotic isotopes beyond $N = 28$, the isotope shift can be obtained and the difference in the mean square charge radii can be deduced. By thus covering the entire chain of isotopes, up to and including $N = 32$, the effect of the shell closure at $N = 28$ and an potential effect at $N = 32$ will be checked. Additionally, comparing the potassium radii to the results of other elements in the Ca region, the Z dependence can be investigated.

Finally, magnetic moments of potassium isotopes were known from ^{35}K up to ^{47}K [33, 34, 35, 31, 36, 37]. Thus, a part of our goal was also to measure the magnetic moments for isotopes beyond $N = 28$ and based on the g factors, make conclusions about the ground-state wave function configuration.

In Table 1.1, information about nuclear spins, masses and half-lives of the potassium chain, as known prior to our experiments, is listed.

Table 1.1: Summarized information about K isotopes before our experiment, where the nuclear spins for neutron-rich isotopes are only tentatively assigned, with conflicting values from different experiments. Masses are taken from Ref. [38] and the half-lives from Ref. [14].

Isotope	I^π	m (u)	$T_{1/2}$
^{38}K	3^+	37.96908112 (21)	7.636 (18) min
^{39}K	$3/2^+$	38.963706486 (5)	stable
^{40}K	4^-	39.96399817 (6)	$1.248(3) \cdot 10^9$ y
^{41}K	$3/2^+$	40.961825258 (4)	stable
^{42}K	2^-	41.96240231 (11)	12.360 (12) h
^{43}K	$3/2^+$	42.9607347 (4)	22.3 (1) h
^{44}K	2^-	43.9615870 (5)	22.13 (19) min
^{45}K	$3/2^+$	44.9606915 (6)	17.81 (61) min
^{46}K	2^-	45.9619816 (8)	105 (10) s
^{47}K	$1/2^+$	46.9616616 (15)	17.50 (24) s
^{48}K	$(1^-, 2^-)$	47.9653412 (8)	6.8 (2) s
^{49}K	$(1/2^+, 3/2^+)$	48.9682108 (9)	1.26 (5) s
^{50}K	$(0^-, 1^-)$	49.972380 (8)	472 (4) ms
^{51}K	$(3/2^+)$	50.975828 (14)	365 (5) ms

1.4 Evolution of π ($1d_{3/2} - 2s_{1/2}$)

The proton-neutron interaction influences the evolution of the $1/2^+$ and $3/2^+$ states for isotopes with $20 \leq N \leq 28$ in the region below Ca ($Z < 20$). More precisely, it was observed that while the $\nu 1f_{7/2}$ orbital is filled, the energy gap between these two states shrinks. This energy shift was for the first time discussed by Bansal and French [39] in 1964 and 15 years later by Pellegrini [40]. Only with the more systematic studies performed in last decade [41], it was possible to obtain a more general picture of the evolution of these two levels in several odd- Z isotopes with neutron number between 20 and 28. In Fig. 1.7 the energy splitting between first excited $1/2^+$ and $3/2^+$ states, $\Delta(1/2^+ - 3/2^+)$, as a function of N is presented for P ($Z = 15$), Cl ($Z = 17$) and K ($Z = 19$) isotopes where the experimental results taken from [42, 19, 43, 44] are compared to the shell model calculations using two different effective interactions. In the extreme single particle shell-model framework, for all these isotopes (odd-even), the nuclear spins of $1/2$ and $3/2$ correspond to a particle or hole ² in the $\pi 2s_{1/2}$ and $\pi 1d_{3/2}$ orbital, respectively. It should be noted that some of the spins in P and

²Particles and holes are equally treated in the shell model.

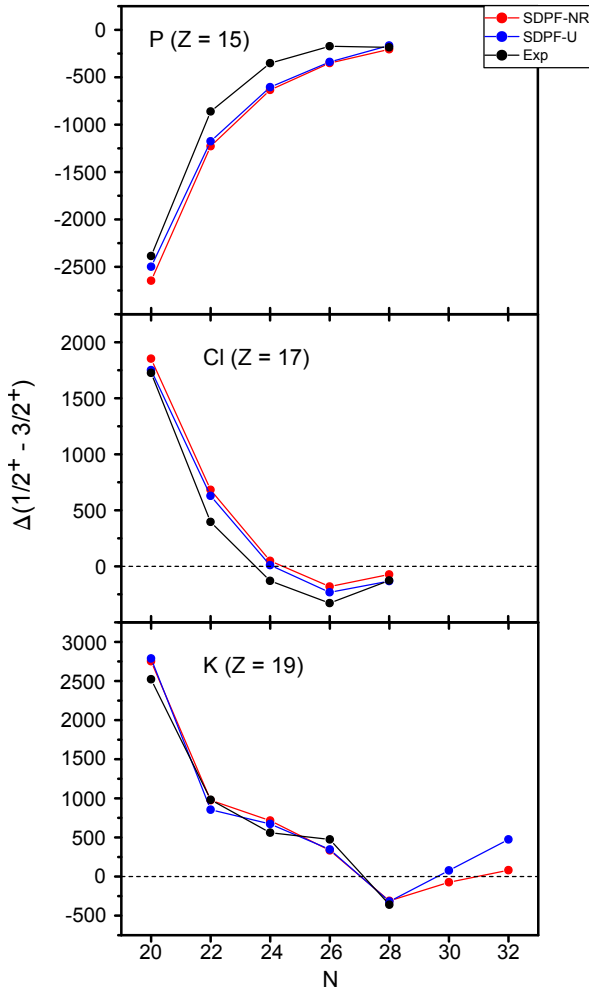


Figure 1.7: Experimental results for the energy splitting between the first excited $1/2^+$ and $3/2^+$ states in P, Cl and K neutron-rich isotopes compared to the shell-model calculations. The experimental data are taken from [42, 19, 43, 44, 21, 22, 23].

Cl were not unambiguously deduced based on experimental evidences, but rather tentatively assigned from the comparison with the shell-model calculations.

A strong shell effect is observed for all three isotopes at $N = 20$, where the first excited state appears only around 1.7 MeV for ^{37}Cl and around 2.5 MeV in the

cases of ^{35}P and ^{39}K . A clear drop in energy of the first excited state is present as more and more neutrons are added into the $1f_{7/2}$ for phosphor isotopes. In the case of chlorine, even a flip of the ground-state spin from $3/2$ to $1/2$ is observed at a half filled $\nu 1f_{7/2}$. The nuclear spin and parity of the ground state for all potassium isotopes up to $A = 45$ is known to be $I^\pi = 3/2^+$, while for the first excited state, it is $I^\pi = 1/2^+$. By filling the $\nu 1f_{7/2}$ orbital, a decrease of the excitation energy is observed. This points to the effect caused by the proton-neutron interaction between the $\pi 1d_{3/2}$ and $\nu 1f_{7/2}$ orbitals. As more neutrons are added into the $1f_{7/2}$, the interaction becomes stronger resulting in a more bound $\pi 1d_{3/2}$ orbital. Consequently, the $\pi 1d_{3/2}$ lies closer in energy to the $\pi 2s_{1/2}$ and as a consequence a decrease of the $1/2^+$ excitation energy is observed. At $N = 28$ where the $\nu 1f_{7/2}$ orbital is completely filled, the proton $2s_{1/2}$ and $1d_{3/2}$ orbitals are degenerate (or even inverted). The nuclear spin of the ground state of ^{47}K is $I = 1/2$.

For isotopes with $29 \leq N \leq 32$, the neutrons start to fill the $2p_{3/2}$ orbit. Although the shell-model calculations could reproduce the experimental results for the K chain very well, they predict different spins for the ground state of ^{49}K and very different excitation energy of the $1/2^+$ state in ^{51}K .

A part of our goal is to measure the ground-state properties of the neutron-rich K isotopes and provide unambiguous conclusions related to the evolution of the $1/2^+$ and $3/2^+$ states beyond $N = 28$.

Chapter 2

Measurements of nuclear moments and charge radii

Nuclear moments and charge radii as probes of the nuclear structure will be introduced in the first part of this chapter. The main properties of these observables as well as the physics which we can learn based on the results in the context of the nuclear structure will be presented. In the second part of this chapter, the hyperfine interaction will be introduced and the atomic hyperfine structure will be demonstrated. It will be shown how we can extract observables from the first part (nuclear moments and radii) based on the hyperfine splitting of the atomic levels.

The most frequent literature used in this chapter is [4, 45, 5, 46]. For more specific cases, the references are given in the text.

2.1 Nuclear moments

Based on their origin, we can distinguish two types of nuclear moments: magnetic dipole moments which arise from the currents in nuclei and the electric moments which are associated with the nuclear charge distribution. Thus, they are sensitive to different information related to the structure of the nucleus. More precisely, the magnetic dipole moment (via the g factor; $\mu = gI$ where I is the nuclear spin) provides information about the wave function and the occupation of the different orbits, while the deformation of the nucleus can be addressed via the electric quadrupole moment.

2.1.1 Magnetic dipole moment

In classical mechanics, the magnetic dipole moment of a particle with mass m , charge e and velocity v which moves in circles of radius r is given as $\vec{\mu} = \frac{e}{2m}\vec{L}$, where $\vec{L} = \vec{r} \times m\vec{v}$ is the angular momentum.

Treating the same particle in the quantum mechanical approach, the expression for the magnetic dipole moment, later called magnetic moment, is given as $\vec{\mu} = g \frac{e\hbar}{2m} \vec{I}$, where \vec{I} is the nuclear spin. Considering the nucleus, we have to take into account that it is a complex system composed of two different types of particles, charged and neutral. The magnetic moment of the nucleus is originating from two effects: the orbiting motion of the protons and from the intrinsic angular momentum, also called intrinsic spin, of all nucleons. Therefore, the magnetic dipole operator can be written as

$$\hat{\mu} = \frac{\mu_N}{\hbar} \left(\sum_i^A g_l^i \hat{l}^i + \sum_i^A g_s^i \hat{s}^i \right), \quad (2.1)$$

where \hat{l}^i and \hat{s}^i are the orbital angular momentum operator and spin operator of the i^{th} nucleon, respectively; $\mu_N = \frac{e\hbar}{2m_p} = 5.05078317(20) \cdot 10^{-27} \text{ JT}^{-1}$ [47] is the nuclear magneton; g_l and g_s are the orbital and spin gyromagnetic ratios. The gyromagnetic ratio, called g factor, is a dimensionless factor.

The experimentally observed g factors for a free proton and a free neutron are listed below [48, 47]:

$$\begin{aligned} g_l^\pi &= 1 & \text{and} & \quad g_s^\pi = +5.585694700(18) & \text{protons} \\ g_l^\nu &= 0 & \text{and} & \quad g_s^\nu = -3.82608545(90) & \text{neutrons} \end{aligned} \quad (2.2)$$

where $g_l^\nu = 0$ comes from the fact that the neutron is not an electrically charged particle, and thus does not possess an orbital magnetic moment which would arise from orbital motion. In addition, for point-like charged particles with spin 1/2 it is expected to have $g_s = 2$. However, the measured intrinsic magnetic moments of the proton and neutron point to the presence of internal structure and to the fact that nucleons are not truly elementary particles.

The single-particle magnetic moment of an unpaired nucleon placed in an orbit with $j = l \pm s$ can be calculated according to the following formulas (Ref. [4]):

$$\begin{aligned} \mu &= j g_l + \frac{g_s - g_l}{2} & \text{for} & \quad j = l + 1/2 \\ \mu &= j g_l - \frac{g_s - g_l}{2} \frac{j}{j+1} & \text{for} & \quad j = l - 1/2. \end{aligned} \quad (2.3)$$

Using the free g factors listed in Eq. (2.2), the free magnetic moments or so-called Schmidt values can be obtained for a single proton and neutron. However,

due to the interaction among the nucleons in a nucleus, one can not treat the nucleons as free particles. Therefore, when comparing experimental values to single particle magnetic moments, one should use effective g factors (g^{eff}): in the medium mass region $g_s^{\text{eff}} \approx 0.7 g_s^{\text{free}}$; $g_l^{\pi, \text{eff}}$ around 1.1 and $g_l^{\nu, \text{eff}}$ around -0.1. Also in shell-model calculations, effective g factors are to be used. They are typically deduced from a fit to available experimental data in the region of interest and dependent on the model space¹ and on the interaction which is used in the calculations. A larger model space will cause less quenching and vice versa.

Using the relation for the nuclear spin $\vec{I} = \vec{L} + \vec{S}$, where $\vec{L} = \sum_i^A l^i$ and $\vec{S} = \sum_i^A s^i$, Eq. (2.1) can be rewritten as follows:

$$\hat{\mu} = \frac{\mu_N}{\hbar} g \hat{I}. \quad (2.4)$$

The measured magnetic moment presents the expectation value of $\hat{\mu}_z$ in the $|I, M = I\rangle$ state

$$\mu = \langle I, M = I | \hat{\mu}_z | I, M = I \rangle. \quad (2.5)$$

It is commonly expressed in units of μ_N , while \hbar can be omitted.

In case of odd-odd nuclei, the magnetic moment can be deduced by taking into account the separate contribution from the odd proton (μ_π) and the odd neutron (μ_ν) (Ref. [4]):

$$\mu = \frac{I}{2} \left[\frac{\mu_\pi}{I_\pi} + \frac{\mu_\nu}{I_\nu} + \left(\frac{\mu_\pi}{I_\pi} - \frac{\mu_\nu}{I_\nu} \right) \frac{I_\pi(I_\pi + 1) - I_\nu(I_\nu + 1)}{I(I + 1)} \right] \quad (2.6)$$

The additivity rule for the magnetic moment can be applied under the assumption that the coupling between the unpaired proton and neutron is weak.

2.1.2 Electric quadrupole moment

The electric quadrupole moment originates from the asymmetrical charge distribution, thus it is a measure of the deviation from the spherical shape of the nucleus. Its operator in the Cartesian coordinate system is defined as

$$\hat{Q}_z = \sum_{i=1}^A \left(\frac{e_i}{e} \right) (3z_i^2 - r_i^2) \quad (2.7)$$

¹For orbitals which are considered in the calculations; more details are given in the section 4.2 related to the shell-model calculations.

where e_i ($i = \pi, \nu$) is the charge of the nucleon in units of e with coordinates (x_i, y_i, z_i) and $r^2 = x^2 + y^2 + z^2$. The same operator in the spherical coordinate system can be written as a tensor of rank 2 and it is given below:

$$\hat{Q}_2^0 = \sqrt{\frac{16\pi}{5}} \sum_{i=1}^A \left(\frac{e_i}{e}\right) r_i^2 Y_2^0(\theta_i, \phi_i) \quad (2.8)$$

where $Y_2^0(\theta_i, \phi_i)$ is the spherical harmonic of rank 2 and the polar angles (θ_i, ϕ_i) are associated with the position of the i^{th} nucleon. For simplicity, the polar angles will be omitted in the following. Similar to the magnetic moment, the quadrupole moment which is observed in the experiments, called spectroscopic quadrupole moment Q_s , is defined as an expectation value of Q_2^0 in the nuclear state with $M = I$. Applying the Wigner-Eckart theorem, one derives

$$Q_s = \underbrace{\begin{pmatrix} I & 2 & I \\ -I & 0 & I \end{pmatrix}}_{3j \text{ symbol}} \underbrace{\sqrt{\frac{16\pi}{5}} \langle I || \sum_{i=1}^A \left(\frac{e_i}{e}\right) r_i^2 Y_2^0 || I \rangle}_{Q_0} \quad (2.9)$$

where Q_0 is the intrinsic quadrupole moment. For nuclei with $I = 0$ and $\frac{1}{2}$, the $3j$ symbol and thus Q_s will be identical to zero.

Intuitively, one could expect that the quadrupole moment operator acts only on the charged particles (protons) and in that case, charges for nucleons are given as $e_\pi = 1 e$ and $e_\nu = 0 e$. This would imply that Q would not change in an isotopic chain regardless of the number of neutrons, which contradicts observation. Thus, similar to effective g factors for magnetic moments, effective charges have to be considered. Depending on the region in the nuclear chart where shell-model calculations are applied, the effective charges are: $e_\pi = (1.35 - 1.6) e$ and $e_\nu = (0.35 - 0.5) e$. Quadrupole moments are usually expressed in $e \text{ fm}^2$ or $e \text{ b}$, where $b = 100 \text{ fm}^2$.

For nuclei that can be described by a closed shell with nuclear spin $I = 0$ and a valence particle or a hole, the single particle quadrupole moment can be defined. The quadrupole moment of a single particle located in the orbit described with quantum numbers $|nljm\rangle$ can be given as

$$Q_{\text{s.p.}}(j) = \begin{pmatrix} I & 2 & I \\ -I & 0 & I \end{pmatrix} \sqrt{\frac{16\pi}{5}} \left(\frac{e_i}{e}\right) \langle jj || Y_2^0 || jj \rangle \langle nl | r^2 | nl \rangle \quad (2.10)$$

where the spherical harmonic Y_2^0 acts only on the angular momentum part and $\langle nl | r^2 | nl \rangle = \langle r^2 \rangle$ is the mean square charge radius of the orbital. Including the reduced matrix elements, the final form can be obtained:

$$Q_{\text{s.p.}}(j) = -\frac{2j-1}{2j+2} \left(\frac{e_i}{e}\right) \langle r^2 \rangle. \quad (2.11)$$

Considering the sign of Q , the shape of the nucleus can be associated with the particle (hole) orbiting in the equatorial plane: in case of $Q < 0$, a particle is orbiting around a spherical core, giving rise to the oblate shape (flattened form) of the nucleus because $3z^2 < r^2$; while in case of $Q > 0$, the nucleus has prolate shape (elongated form) originating from a moving hole with $3z^2 > r^2$.

For nuclei where more valence particles (n) are placed in the same orbit characterized with j^n and coupled to the total spin I , the quadrupole moment can be described in the seniority scheme proposed by de-Shalit and Talmi [49] as

$$Q_n = \langle j^{n,\nu} | \hat{Q} | j^{n,\nu} \rangle = \frac{2j+1-2n}{2j+1-2\nu} \langle j^\nu | \hat{Q} | j^\nu \rangle, \quad (2.12)$$

where n presents the number of particles in the same orbit and ν is the number of unpaired particles from the same orbit, called the seniority number. For the case where $\nu = 1$, $\langle j^\nu | \hat{Q} | j^\nu \rangle = Q_{s.p.}(j)$ and Eq. (2.12) shows linearity with n and the single-particle moment.

The quadrupole moments of odd-odd nuclei where an unpaired proton and neutron are coupled to spin I can be calculated from the additivity rule (Ref. [4])

$$\begin{aligned} Q = & (-1)^{j_\pi+j_\nu+I} \cdot (2I+1) \left(\begin{array}{ccc} I & 2 & I \\ -I & 0 & I \end{array} \right) \\ & \times \left\{ \begin{array}{ccc} j_\pi & I & j_\nu \\ I & j_\pi & 2 \end{array} \right\} \frac{Q_\pi}{\left(\begin{array}{ccc} j_\pi & 2 & j_\pi \\ -j_\pi & 0 & j_\pi \end{array} \right)} \\ & + \left\{ \begin{array}{ccc} j_\nu & I & j_\pi \\ I & j_\nu & 2 \end{array} \right\} \frac{Q_\nu}{\left(\begin{array}{ccc} j_\nu & 2 & j_\nu \\ -j_\nu & 0 & j_\nu \end{array} \right)}, \end{aligned} \quad (2.13)$$

where $j_{\pi,\nu}$ and $Q_{\pi,\nu}$ are the spin and quadrupole moment of the odd-proton (odd-neutron). Curly brackets denote $6j$ symbol, while the regular ones $3j$ symbol.

Deformation of the nucleus

In nuclei further from the closed shells, more valence particles will define the nuclear structure, causing the break-down of the single-particle representation. The interaction among these nucleons will lead to a non-spherical charge distribution, inducing a deformation of the nucleus. In this picture, the intrinsic quadrupole moment Q_0 can be related to the deformation parameter β , which describes the elongation of a spheroid (Ref. [45]), as:

$$Q_0 = \frac{3}{5\pi} Z R_0^2 \beta (1 + 0.16\beta), \quad (2.14)$$

where R_0 represents the radius of the spherical nucleus of the same volume. We will see further that also the nuclear mean square charge radius can be related to this parameter. Considering the β parameter, we can distinguish two types of shape: $\beta > 0$ corresponds to prolate shape which is popularly called the rugby ball, while $\beta < 0$ leads to the oblate shape also known as the disc.

The relation between the observed and the intrinsic quadrupole moment for a axial deformed nucleus can be given as

$$Q_s = \frac{3K^2 - I(I+1)}{(I+1)(2I+3)} Q_0, \quad (2.15)$$

where K is the projection of the nuclear spin on the deformation axis. This is applied with an assumption that the deformation of the nucleus is axially symmetric (which is not always valid) and with the nuclear spin having a well-defined direction with respect to the symmetry axis of the deformation [45].

2.1.3 The Mean Square Charge Radius

Since the boundaries of the nucleus are not well defined, it is impossible to determine its radius exactly. As an alternative, one can work with the average radius, called the mean square charge radius, defined as

$$\langle r^2 \rangle = \frac{\int \rho(r) r^2 d^3r}{\int \rho(r) d^3r}, \quad (2.16)$$

In case $\rho(r)$ represents the distribution of the charge density of the protons in the nucleus then this is the mean square charge radius. The integral in the denominator is then the total charge of the nucleus, Ze . The charge density distribution is commonly presented with the Fermi function as:

$$\rho(r) = \frac{\rho_0}{1 + e^{\frac{r-R_{1/2}}{a}}} \quad (2.17)$$

where ρ_0 is the nuclear density for $r = 0$, called the central density, $R_{1/2}$ is the radius for which the nuclear density reaches half of the starting value and the parameter a is defined as $a \approx \frac{t}{4 \ln 3}$ with t being the skin thickness parameter. The last parameter represents the range or the radius in which the nuclear density drops from 90 % to 10 % of the density at the center of the nucleus.

In the liquid-drop model, the proton distribution is considered to be homogeneous over the nuclear volume. Thus, one assumes that the radius of the proton distribution corresponds to the radius of the mass distribution

given as $R = R_0 A^{1/3}$, where $R_0 \approx 1.2 \text{ fm}$ and A is the mass number. Within this model, the mean square charge radius can be presented as [45]:

$$\langle r^2 \rangle_{\text{LD}} = \frac{3}{5} R_0^2 A^{2/3}. \quad (2.18)$$

So far we considered only spherical nuclei, however, the majority of the nuclei from the nuclear chart are not spherical. Using the quadrupole deformation parameter β as a measure of deformation, the mean square charge radius of these nuclei can be expressed as

$$\langle r^2 \rangle = \underbrace{\frac{3}{5} R^2}_{\langle r^2 \rangle_{\text{sph}}} + \underbrace{\frac{3}{4\pi} \beta^2}_{\frac{5}{4\pi} \langle r^2 \rangle_{\text{sph}}}, \quad (2.19)$$

where $\langle r^2 \rangle_{\text{sph}}$ is the mean square charge radius of a spherical nucleus with the same volume.

2.2 Atomic Hyperfine Structure

The interaction between a nucleus and its surrounding atomic electrons is known as the hyperfine interaction and for nuclei with $I \geq 0$ it can be expressed as

$$H_{\text{hf}} = H(E0) + H(M1) + H(E2) + \dots, \quad (2.20)$$

where $H(E0)$, $H(M1)$ and $H(E2)$ stands for the electric monopole, magnetic dipole and electric quadrupole interaction, respectively. This interaction gives rise to an additional energy splitting of the electronic levels, called hyperfine splitting.

2.2.1 Magnetic dipole hyperfine parameter

The magnetic dipole interaction originates from the effect of the magnetic field arising from the electrons on the magnetic moment, and in the Hamiltonian this translates into a coupling of the nuclear spin (\vec{I}) and the angular momentum of the electrons around the nucleus (\vec{J}). It can be described as

$$H(M1) = A \vec{I} \cdot \vec{J}. \quad (2.21)$$

The new quantum number of the electrons+nucleus system which arises from this coupling is called the total angular momentum F , $\vec{F} = \vec{I} + \vec{J}$. This causes

the splitting of the electronic levels into $2J + 1$ ($2I + 1$) hyperfine states in case of $J < I$ ($I < J$) for different F quantum numbers. The magnetic hyperfine splitting can be quantified as

$$E_F(A) = \frac{A}{2} \underbrace{[F(F+1) - I(I+1) - J(J+1)]}_{C} \cdot h = \frac{AC}{2} \cdot h \quad (2.22)$$

where h is the Planck's constant and A is the magnetic dipole hyperfine parameter defined as

$$A = \frac{\mu B(0)}{IJ}, \quad (2.23)$$

where μ is the magnetic moment and $B(0)$ is the magnetic field originating from the electrons at the nuclear center ($r = 0$). It should be noted that there is no magnetic dipole interaction present in case of $I = 0$ or $J = 0$.

2.2.2 Electric quadrupole hyperfine parameter

The interaction between the quadrupole moment of the nucleus (Q) and the electric field gradient generated by electrons at the position of the nucleus (V_{zz}) causes an additional hyperfine splitting of the atomic fine structure levels. This splitting can be described via the following formula:

$$E_F(B) = B \frac{\frac{3}{4}C(C+1) - I(I+1)J(J+1)}{2I(2I-1)(2J-1)} \cdot h \quad (2.24)$$

where B is the electric quadrupole hyperfine parameter defined as

$$B = eQV_{zz}. \quad (2.25)$$

There are two limiting factors for the determination of the B parameter: first, only electronic configurations with $J > 1/2$ have $V_{zz} \neq 0$ and second, there is $Q \neq 0$ for isotopes with $I \neq 0, \frac{1}{2}$.

The hyperfine splitting of the electronic levels with $J_1 = J_2 = 1/2$ for isotopes with $I = 3/2$ is shown in Fig. 2.1. For potassium isotopes, the magnetic hyperfine parameter of the ground state, $A(S_{1/2})$, was found to be between 200 - 700 MHz and even up to 2000 and 3000 MHz for ^{47}K and ^{49}K , respectively. On the other hand, the hyperfine parameter of the excited state, $A(P_{1/2})$, is an order of magnitude smaller. This fine structure transition is not sensitive to the quadrupole splitting. In transitions where the quadrupole interaction is present, the contribution of the quadrupole interaction is often very weak and the extracted value for B hyperfine parameter is of the order of 10 – 100 MHz.

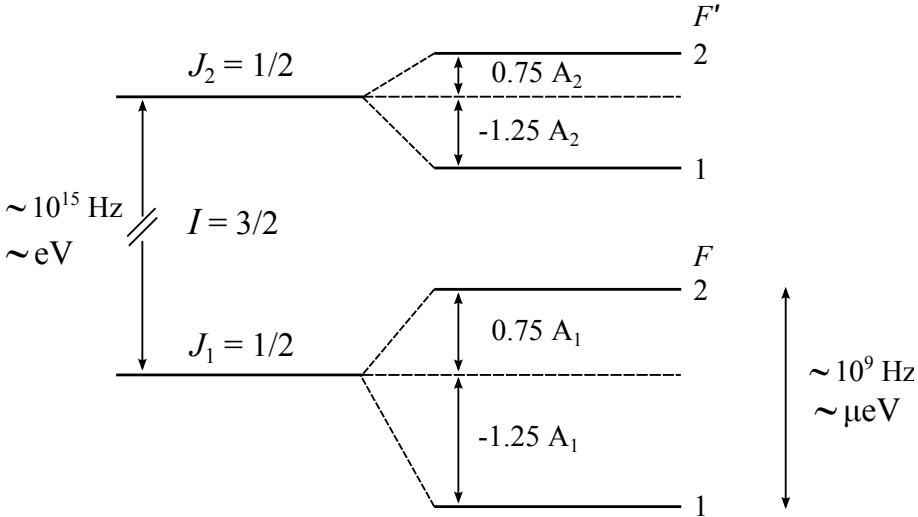


Figure 2.1: Hyperfine splitting for $I = 3/2$ isotope with $J_1 = J_2 = 1/2$ electronic states. For this transition, there is no quadrupole interaction.

Coupling the two electron angular momenta (\vec{J}_1, \vec{J}_2) into the total angular momentum $\vec{J} = \vec{J}_1 + \vec{J}_2$, one can arrive to the selection rules for transitions between fine structure and hyperfine structure levels. Based on the triangular condition $|J_2 - J_1| \leq J \leq J_1 + J_2$ and that $J_1 + J_2 + J$ has to be an integer number one finds that

$$\Delta F = 0, \pm 1 \quad \text{and} \quad F + F' \geq 1. \quad (2.26)$$

The relative intensities of the peaks in the hyperfine spectrum, which correspond to the dipole transition strengths between components labeled with F and F' , are given by the following formula [50]:

$$I_{F \rightarrow F'} \propto (2F + 1)(2F' + 1) \left\{ \begin{array}{ccc} J' & F' & I \\ F & J & 1 \end{array} \right\}^2. \quad (2.27)$$

They are also called the Racah intensities and were used in the spin determination of ^{48}K published by K. Kreim and co-authors [51] which is included in this thesis as the Article IV (Appendix A.1).

By fitting the position of the peaks in the hyperfine spectra, we are able to obtain the hyperfine parameters of the ground and excited states, the isotope shift² with

²Isotope shift is defined as the difference in transition frequency between two atomic states relative to a reference value.

respect to some reference frequency and the nuclear spin. In order to extract information such as magnetic and quadrupole moments, relative measurements are used. This is possible due to the fact that $B(0)$ from Eq. (2.23) and V_{zz} from Eq. (2.24) are constant for the entire isotopic chain, in a first order approximation.

Magnetic moments from the experimental results are deduced via the following formula:

$$\mu = \frac{IA}{I_{\text{ref}}A_{\text{ref}}} \mu_{\text{ref}}, \quad (2.28)$$

while the quadrupole moment were obtained by:

$$Q = \frac{B}{B_{\text{ref}}} Q_{\text{ref}} \quad (2.29)$$

2.2.3 Isotope shift

In addition to the hyperfine parameters, we also determined the transition frequency between two atomic states relative to a reference value, known as the center of gravity (COG), ν^A . Due to the difference in the mass and size of the nucleus for different isotopes, the monopole interaction between the electron cloud and the nuclear charge distribution is changing from isotope to isotope, yielding a shift of the fine structure energy levels, in particular for levels where the electrons penetrate the nuclear volume ($S_{1/2}$ and $P_{1/2}$). Thus, a difference in the frequency between two isotopes defines the isotopes shift (IS):

$$\delta\nu^{AA'} = \nu^{A'} - \nu^A \quad (2.30)$$

where A, A' are the atomic mass numbers of the involved isotopes.³

The IS has two components, the mass shift ($\delta\nu_{MS}$) and the field shift ($\delta\nu_{FS}$), thus it can be expressed as

$$\delta\nu^{AA'} = \delta\nu_{MS} + \delta\nu_{FS} \quad (2.31)$$

In what follows, these two contributions will be described in more detail.

Mass shift

The mass shift arises from the motion of the electrons and the nucleus around their common center of mass. It is commonly presented as a sum of two shifts,

³The use of the same symbol (A) for the hyperfine parameter and the atomic mass number should be clear at this point.

the normal mass shift ($\delta\nu_{NMS}$) and the specific mass shift ($\delta\nu_{SMS}$). The former term originates from the effect of the reduced mass correlation of the electrons-nucleus system on the transition frequency, while the latter is related to the changes in the correlation between the electrons from isotope to isotope, when neutrons are changing. In both cases the mass shift is proportional to the reduces mass. The mass shift can be expressed as

$$\delta\nu_{MS}^{AA'} = \underbrace{K_{NMS} \frac{m_{A'} - m_A}{m_{A'} m_A}}_{\delta\nu_{NMS}} + \underbrace{K_{SMS} \frac{m_{A'} - m_A}{m_{A'} m_A}}_{\delta\nu_{SMS}} = K_{MS} \frac{m_{A'} - m_A}{m_{A'} m_A} \quad (2.32)$$

where K_{MS} is the mass shift constant and can be written as a sum of the normal and specific mass shift constants: $K_{MS} = K_{NMS} + K_{SMS}$. The normal mass shift constant, K_{NMS} , is calculated from $K_{NMS} = m_e \nu_0$ where m_e is the mass of the electron and ν_0 is the transition frequency. For K isotopes it was calculated to be $K_{NMS} = 213.55 \text{ GHz}\cdot\text{u}$. The specific mass constant involves the correlation between the momenta of the electrons and its calculation is not trivial. In case of potassium, we used the value reported in Ref. [52] $K_{SMS} = -15.4(38) \text{ GHz}\cdot\text{u}$.

Field shift

The change of the electrostatic potential experienced by electrons moving in the region with an extended nuclear charge distribution causes a small shift of the atomic levels, called the field shift, $\delta\nu_{FS}^{AA'}$. It is commonly expressed as:

$$\delta\nu_{FS}^{AA'} = F \lambda^{AA'}, \quad (2.33)$$

where F is the electronic form factor which is element and transition dependent. For K isotopes this was calculated using *ab initio* atomic structure calculations and it was found to be $F = -110(3) \text{ MHz fm}^{-2}$ [52]. The nuclear parameter $\lambda^{AA'}$ is defined as

$$\lambda^{AA'} = \delta\langle r^2 \rangle^{AA'} + \frac{C_1}{C_2} \delta\langle r^4 \rangle^{AA'} + \frac{C_1}{C_3} \delta\langle r^6 \rangle^{AA'} + \dots \quad (2.34)$$

where C_i are coefficients tabulated in [53] for $30 \leq Z \leq 103$ and $\delta\langle r^2 \rangle = \langle r^2 \rangle^A - \langle r^2 \rangle^{A'}$ is the difference in the mean square charge radius between two isotopes. For lighter masses, a good approximation is made by taking only the first term in Eq. (2.34) as $\lambda^{AA'} \approx \delta\langle r^2 \rangle^{AA'}$ and rewriting the field shift as

$$\delta\nu_{FS}^{AA'} = F \delta\langle r^2 \rangle^{AA'}. \quad (2.35)$$

Assuming that the electron wave function is almost constant in the nucleus and $\psi(r) = \psi(0)$ in the nuclear volume, in the non-relativistic approach the field shift can be expressed as [54]:

$$\delta\nu_{FS}^{AA'} = -\frac{2\pi Ze^2}{3}\Delta|\psi(0)|^2\delta\langle r^2 \rangle, \quad (2.36)$$

where $\Delta|\psi(0)|^2$ is the difference in the electron density at the nucleus between the upper and lower atomic states. For heavier elements, the last formula has to be treated in the relativistic approach and it becomes more complex.

Finally, we are able to rewrite Eq. (2.31) in a way that the isotope shift carries the information about the change of mean square charge radii:

$$\delta\nu^{AA'} = K_{MS} \frac{m_{A'} - m_A}{m_{A'} m_A} + F\delta\langle r^2 \rangle^{AA'}. \quad (2.37)$$

The dominant role of the mass shift in the isotope shift decreases with Z due to its $\sim \frac{1}{m^2}$ dependence, while the field shift influences more the isotope shift for the higher masses. Considering the isomer shift, the shift in the frequency between the ground and an isomeric excited state of the same nucleus, the mass shift is zero. The isomer shift of ^{38}K between ground ($I = 3$) and isomeric state ($I = 0$) will be discussed in this thesis in Chapter 5. It probes directly the difference in the mean square charge radius of the two long-lived states in this $N = Z$ isotope and is therefore very sensitive to proton-neutron correlations.

Knowing the mass shift constant and the electronic factor, it is trivial to calculate the change in the mean square charge radii between two isotopes, from the experimentally determined isotope shift, using Eq. (2.37).

If the electronic factor and the mass shift constants are known for another transition of the same element, and if also the isotope shifts have been measured for that transition, then it is possible to use the King plot to extract the F and K_{MS} for the transition of interest, relative to those of the other transition. For two transitions (i, j) where F_i and $K_{MS,i}$ are known, one can write:

$$\begin{aligned} i: \quad \delta\nu_i^{AA'} &= F_i \delta\langle r^2 \rangle^{AA'} + K_{MS,i} \frac{m_A - m_{A'}}{m_A m_{A'}} \\ j: \quad \delta\nu_j^{AA'} &= F_j \delta\langle r^2 \rangle^{AA'} + K_{MS,j} \frac{m_A - m_{A'}}{m_A m_{A'}}. \end{aligned} \quad (2.38)$$

Combining these two equations into one, one obtains the following expression:

$$\underbrace{\frac{m_A m_{A'}}{m_A - m_{A'}} \delta\nu_i^{AA'}}_Y = \underbrace{\frac{F_i}{F_j}}_\alpha \underbrace{\frac{m_A m_{A'}}{m_A - m_{A'}} \delta\nu_j^{AA'}}_X + K_{MS,i} - \underbrace{\frac{F_i}{F_j} K_{MS,j}}_\beta \quad (2.39)$$

Plotting mass-corrected IS_i vs mass-corrected IS_j and performing a linear fit allows us to extract the gradient (α) and intercept (β). Based on this

information, we are able to deduce the electronic factor and mass shift of the transition of interest, relative to those of the reference transition. It should be noted that in order to be able to use the King plot analysis, the mean square charge radii of at least three isotopes have to be already measured. More information about the King plot analysis can be found in Ref. [55].

Chapter 3

Experimental results

The experimental results for this thesis were obtained at the beam-line for collinear laser spectroscopy called COLLAPS located at ISOLDE in CERN. This chapter will give a brief overview of the experimental set-up, followed by the details related to the potassium experiments such as bunching and voltage calibration. Furthermore, the procedure of the analysis including the suitable line-shape and an issue with the $I = 0$ spectra will be also discussed. The chapter will be finished with the estimated systematic uncertainties and hyperfine structure anomaly.

3.1 The ISOLDE facility

The ISOLDE facility [56, 57] is an Isotope Separation On Line (ISOL) type of facility for studies in nuclear physics at the European Organization for Nuclear Research known as CERN. The potassium experimental campaign from where the data for this thesis were obtained consisted of two experiments held in November 2010 and June 2012.

The primary beam of high energy protons (1.4 GeV) from the Proton Synchrotron Booster (PSB) was bunched, with a minimal bunch spacing of 1.2 s and a bunch length of $2.4 \mu\text{s}$. Each bunch contained up to $3 \cdot 10^{13}$ protons, thus providing a maximum beam current of around $2 \mu\text{A}$. When the protons hit the radioactive target, a large variety of nuclei are produced via different mechanisms: fission, fragmentation and spallation. During the potassium experiments, a UC_x target (45 g/cm^2) was used at a temperature around 2000°C . After diffusion out of

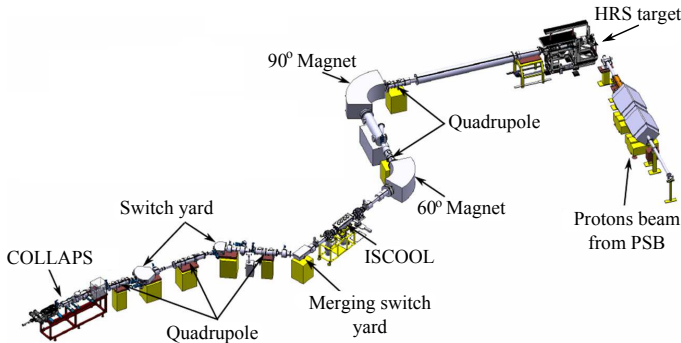


Figure 3.1: Schematic representation of the ISOLDE hall and location of the set-up to collinear laser spectroscopy COLLAPS.

the target, the reaction fragments were ionized by the surface ion source and guided to the High Resolution Mass Separator (HRS). After the isotope of interest was selected, the beam was guided to the gas-filled Paul trap called ISCOOL [58] which cools and bunches the beam. Finally, the ions were guided to the permanent beam line for collinear laser spectroscopy called COLLAPS. Schematic representation of the ISOLDE beam line finishing with the COLLAPS set-up is presented in Figure 3.1.

3.2 Collinear laser spectroscopy beam line

3.2.1 Basic ideas

Before the detailed description of the COLLAPS beam line, the principle of the collinear laser spectroscopy technique will be briefly described. This technique is based on the overlap of an atomic/ionic beam with a laser beam. By tuning the laser frequency such that it matches the excitation energy between the atomic/ionic ground state and some excited state, it is possible to resonantly excite the atom/ion. If a very high-resolution laser light is used (such as provided by a continuous laser system) and if all ions have a similar velocity, then it is possible to excite a single atomic hyperfine structure transition (e.g. shown in Fig. 2.1). Thus by scanning the laser frequency and observing the subsequent decay of the fluorescent photons, it is possible to observe the hyperfine structure, from which the nuclear structure information can be extracted.

Instead of scanning a laser frequency, one can alternatively modify the beam energy (velocity) and used the Doppler-shifted laser frequency observed by the beam to scan over the hyperfine levels.

The experiment is performed on an ensemble of atoms/ions. The thermal movements of the atoms in the ensemble cause the Doppler broadening of the spectral line. This effect originates from the fact that due to the velocity distribution along the propagation axis, the resonant frequency will be slightly different for every velocity range. The velocity distribution of a gas at certain temperature T is given by the Maxwell-Boltzmann distribution, and causes the spectral line with a Doppler width [45]:

$$\delta\nu_D = \frac{\nu_0}{c} \sqrt{\frac{8k_B T \ln 2}{m}} = \frac{\nu_0}{c} \delta v \quad (3.1)$$

where ν_0 is transition frequency, m is mass of the atom, k_B is the Boltzmann constant. δv represents the relative spread in the velocity of the ions, which is not zero due to the high cavity temperature. The Doppler width for ions in a hot cavity is often of the order of 1 GHz or more. In order to overcome this Doppler broadening, the method of collinear laser spectroscopy is used. In this case the ion beam is accelerated to an energy $E = mv^2/2$, with the ions now having an average velocity v . The Doppler shifted laser frequency observed by the accelerated ion beam is now given by

$$\Delta\nu_D = \nu_0 \frac{v}{c}. \quad (3.2)$$

with v the mean velocity of the accelerated ion beam. The key point is in fact that the ions are released from the target with a certain spread of the kinetic energy δE . By applying an acceleration voltage, all ions from the ensemble will experience the same increase in their kinetic energy (eV) although the energy spread remains constant:

$$\delta E = \delta \left(\frac{mv^2}{2} \right) = mv\delta v = const. \quad (3.3)$$

This implies that if the ions are accelerated, their velocity spread is decreasing. Combining Eq. (3.1), Eq. (3.2) and $v = \sqrt{2eVm^{-1}}$ into the last equation, one obtains the Doppler width as a function of the energy spread and acceleration voltage:

$$\delta\nu_D = \nu_0 \frac{\delta E}{\sqrt{2eVm c^2}}. \quad (3.4)$$

For our experiment ($\nu_0 = 3.89285710^{14}$ Hz, $\delta E = 1.5$ eV and $V = 40$ keV) the Doppler width is estimated to be around 10 MHz. This value is similar to the

natural line width ($\delta\nu_N$), which is calculated as $\delta\nu_N = 1/(2\pi\tau)$ where τ is the half-life of the excited state in the used transition. For our case, $\tau = 2.6 \cdot 10^{-8}$ s and thus $\delta\nu_N = 6$ MHz.

3.2.2 COLLAPS beam line

The COLLAPS beam line is situated at the beginning of the experimental hall of the ISOLDE facility. The beam from ISCOOL was kicked by 10° from the main beam line by electrostatic deflectors. In the COLLAPS beam line, the ions first reached the post-acceleration region. This consists of four ring electrodes and provides the acceleration/deceleration voltage for the Doppler tuning. Next, the ions entered the charge exchange cell (CEC) where they are neutralized via the collisions with the potassium vapor. During the experiments, a neutralization efficiency between 50% to 80% was obtained.

Due to the overlap with the laser light, the atoms were excited and after the deexcitation, photons were emitted. They were recorded by four photomultiplier tubes (PMT's) placed in two rows perpendicular to the beam line. The schematic representation of the COLLAPS beam line and the detectors is given in Fig. 2 in the Article II (section 4.4).

During the potassium experiments, the continuous wave (cw) Titanium:sapphire (Ti:Sa) laser was pumped with laser light of 532 nm and 10 W from a solid-state laser (Coherent Verdi V18) providing CW light of 769.9 nm to excite the $4s\ ^2S_{1/2} \rightarrow 4p\ ^2P_{1/2}$ transition in K isotopes. The frequency of the laser was recorded and saved automatically as a wave number (λ^{-1}) by a wave-meter, 4 times per second. From this data, the stability of the laser wavelength could be monitored, the average value of the wave number was calculated and used in the analysis. During the run in 2010 the laser had to be relocked, changing the value from $13003.12010(60)\text{ cm}^{-1}$ to $13003.11095(13)\text{ cm}^{-1}$. In the next run, the wavenumber was set to $13003.09882\text{ cm}^{-1}$ and remained constant within $1.6 \cdot 10^{-4}\text{ cm}^{-1}$ throughout the experiment. Considering the power of the laser, we can distinguish two sets of data. In the first experiment (data from 2010), low laser power in the range from 0.1 mW up to 0.7 mW was used, while during the second experiment the higher power, from 1 mW up to 1.3 mW, was used. Higher laser power induces power broadening of the transition, which has an influence on the deduced A hyperfine parameters, as discussed later in this chapter.

A significant improvement of the sensitivity of the technique was achieved by using a bunched radioactive beam [59] from ISOLDE. The key point is to accept signals from the PMT's only during the time that the ion bunch passes in front of them. As the ion bunches released by ISCOOL are typically of $6\ \mu\text{s}$ long,

this reduces the background photon counts by a factor 10^4 , considering that the time between bunches is typically of the order of 100 ms. Time gating is performed using the time-of-flight (TOF) spectrum, such that the gates were set individually for every isotope. The delay time (t_d) between the bunch released from ISCOOL and its arrival in front of the PMT's was about $45\ \mu\text{s}$ and the width (t_w) of the bunches about $6\ \mu\text{s}$. The start for the TOF spectra was triggered by the same TTL signal which opened the ISCOOL. The signal was recorded by a multi-channel scaler (Stanford Research Systems SR430) where as an input signal the ungated signal from one of the PMT's was used. As an example, a typical TOF spectrum for $A = 50$ is shown in Fig. 3.2.

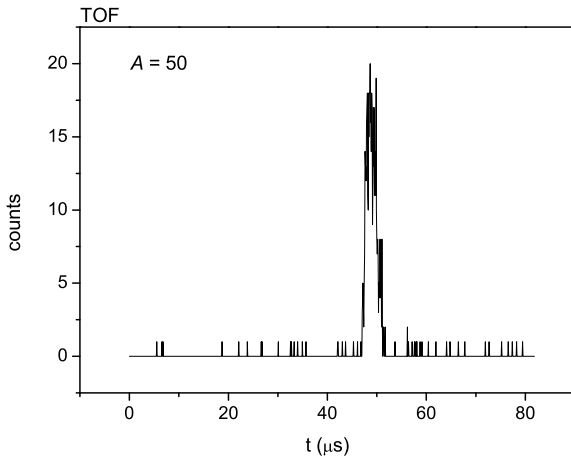


Figure 3.2: Time-of-flight spectrum (TOF) for $A = 50$. Based on this spectrum, settings for ${}^{50}\text{K}$ for a bunching mode were set: delay on the gates $47.5\ \mu\text{s}$ and the width of the time gate to $4\ \mu\text{s}$.

During the first experiment in 2010, the bunch sequence has been kept constant for all isotopes. The typical release time of K ions from the target and ion source is of the order of a few hundred ms [60]. Therefore, after each proton pulse, only 6 bunches of 45 ms accumulation time each have been collected, and released within $100\ \mu\text{s}$. The bunching cycle was stopped after 270 ms (so 6 bunches), and started again after a next proton pulse. This is presented in Fig. 3.3.

Due to the large background observed during the measurement on ${}^{51}\text{K}$, we were not able to obtain the hfs spectrum for this isotope. More precisely, the background photon counts for ${}^{49}\text{K}$ was around 2.5 counts per proton pulse,

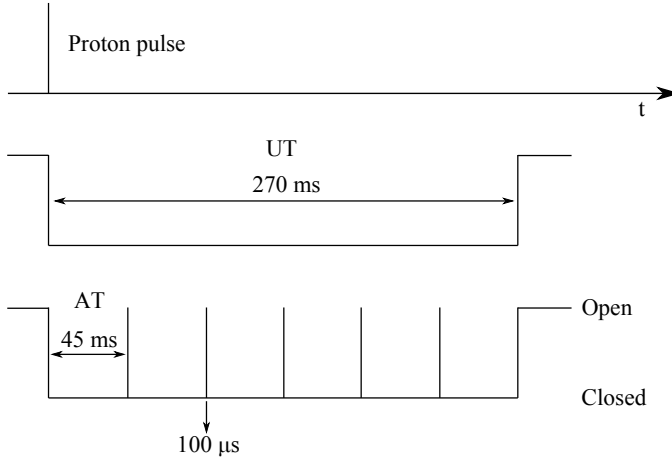


Figure 3.3: Schematic representation of the multiple bunching. Useful time (UT) represents the time when the bunching is performed after the proton pulse and accumulation time (AT) represents the time when the buncher is closed.

while for ^{51}K it was around 7 counts per pulse. The numbers represent the averaged sum from all PMT's for the gated signal. The background from the scattered laser light was measured by blocking the ion beam and performing a regular hfs scan. The average PMT's count for this configuration was less than 1 per proton pulse, meaning that this effect is negligible. Thus, the source of the higher background signal of ^{51}K is from the non-resonant excitation in the CEC of contaminating ions present in the beam. With the efficiency of our set-up, which was estimated to be around $4 \cdot 10^{-5}$ (1 fluorescent photon per 30000 ions), and the estimated yield of ^{51}K to be around 3000 ions per proton pulse, we would need 10 proton pulses to obtain 1 resonance photon on the top of about 80 counts in the background.

Thus, after the run, an additional test was performed to investigate the possibility of the background reduction with a RG715 filter (SCHOTT). This filter blocks all frequencies lower than the frequency of the fluorescent transition in ^{51}K (769.9 nm). Based on the specification of the filter the transparency for 715 nm should be around 50%, while for 620 nm and 815 nm it is 10^{-3} and 96%, respectively. For the frequency of the potassium transition (769.9 nm), the transparency is around 90%. During the test, the filter was placed on the PMT from the right side in the second row (R2) with respect to the incoming beam. Additionally, the protons were stopped, thus we expected to see the beam containing only the stable or long-lived K isotopes and isobaric contamination. The recorded time-of-flight (TOF) spectra for $A = 39$ and $A = 51$ by the PMT

with (R2) and without (L2, left side in the second row) the filter are shown in Fig. 3.4.

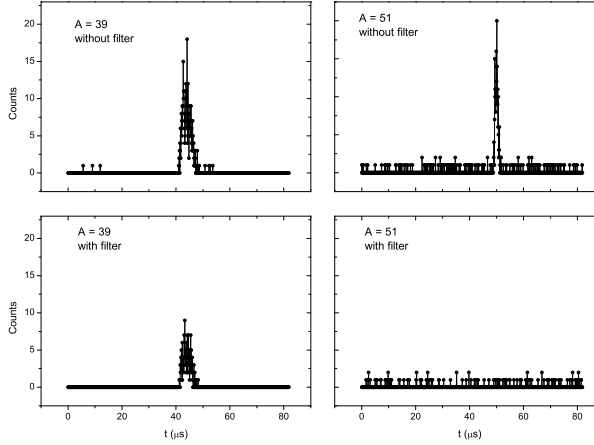


Figure 3.4: TOF spectra of mass $A = 39$ and $A = 51$ recorded by PTM without filter (upper row; L2 PMT) and with filter (lower row; R2 PMT). In case of $A = 51$, the filter blocked light originating from the isobaric contamination. The signal for $A = 39$ was reduced due to the transmission loss and the small solid angle induced by the filter.

In case of $A = 39$, a reduction of the signal from the ^{39}K fluorescence by a factor of two is obtained due to the losses in the filter itself as well as due to the fact that the filter reduced the solid angle (1.5 inch diameter). From TOF spectra of $A = 51$, where no stable K is present, the observed signal must come from excitations of long-lived beam contaminants in the CEC. Comparison of data with and without filter illustrates that the filter blocked the signal originating from the long-lived beam contaminants.

In 2012, we had another experiment with the main goal to measure the hfs of ^{51}K . In order to maximally optimize the conditions during the experiment for the most exotic isotope, in addition to the larger RG715 filter (3 inch diameter) enabling a larger solid angle which was mounted at the front of all PMT's, the release curve of $A = 51$ was recorded, providing information about how fast potassium is released from the target. It was measured with a continuous beam impinging on the movable secondary electron multiplier (SEM) which is placed

at the end of the COLLAPS beam line. The release curve of $A = 51$ is shown in Fig. 3.5.

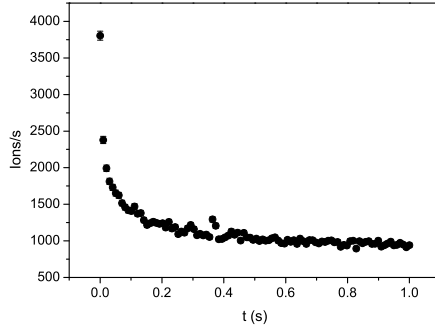


Figure 3.5: Release curve of $A = 51$. Useful time (UT) for measurements of this isotope was limited to 181 (15) ms.

Based on the obtained results, the accumulation time for ^{51}K was reduced to 200 ms (bunch time per proton pulse), while for the other isotopes it was kept around 400 ms (4 or 7 bunches of 60 or 100 ms each). The overview of the information used for the setting of the bunching mode for all studied isotopes during both experiment are presented in Table 3.1.

3.2.3 Conversion of raw data

The raw experimental data are saved as PMT counts versus a scanning voltage (V_{scan}), which is used to scan over the hyperfine structure using the Doppler shift of the observed laser frequency. In order to convert voltage to frequency, the relativistic Doppler formula was used [45]:

$$\nu = \nu_{\text{laser}} \sqrt{\frac{1 - \beta}{1 + \beta}}, \text{ with } \beta = \sqrt{1 - \frac{m^2 c^4}{(eV_{\text{total}} + mc^2)^2}} \quad (3.5)$$

where ν_{laser} is the laser frequency used during the experiment, m is the atomic mass taken from AME2012 [38] and V_{total} represents the total voltage experienced by the ions. The latter parameter can be expressed as:

$$V_{\text{total}} = V_{\text{ISCOOL}} + V_{\text{offset}} + f_{\text{kepco}} \cdot V_{\text{scan}} \quad (3.6)$$

where V_{ISCOOL} is the applied voltage after the ISCOOL cooler/buncher, V_{offset} is a fixed offset voltage applied for every isotope, in order to account for the

Table 3.1: Overview of the gate and bunch settings during the experiments. t_d is the delay time on the gates, t_w is the gate's width, AT stands for the accumulation time per bunch, NB is the number of bunches per proton pulse and UT is useful time after proton pulse.

Run	isotope	t_d (μ s)	t_w (μ s)	AT (ms)	NB	UT (ms)
2010	^{38}K	41.5	4	45	6	270
	^{39}K	40	8	45	6	270
	^{42}K	42.5	6.5	45	6	270
	^{44}K	43	8	45	6	270
	^{46}K	43	8	45	6	270
	^{47}K	45	7	45	6	270
	^{48}K	45	7	45	6	270
	^{49}K	47	4	45	6	270
	^{50}K	47.5	4	45	6	270
	^{38}K	41.5	4	100	4	400
2012	^{39}K	41	7	60	7	420
	^{42}K	42.5	6.5	60	7	420
	^{47}K	46	6	60	7	420
	^{50}K	47.5	4	100	4	400
	^{51}K	48	4	100	2	200

mass shift. The next parameter is an amplification factor (called kepco factor) which is used to amplify the scanning voltage. The scanning voltage (V_{scan}) is the voltage applied for scanning, in the range of ± 10 V with a precision (minimal step) of 0.01 V. During the K experiments, most of the data were scanned with the settings where the step size was between 0.02 V and 0.035 V. Finally, a total range of ± 500 V can be scanned.

Information about V_{ISCOOL} is written in the logbook during the experiment. In Figure 3.6, V_{ISCOOL} as a function of time, is shown. The total shift obtained during the experiment in 2010 was around 3 V and about 2.25 V in 2012. In order to avoid the influence of such long-term drifts on the deduced isotopes shift, the hyperfine spectrum of the reference isotopes (^{47}K) was always measured after the scan of an isotope of interest.

To determine the kepco factor, a calibration measurement of the real voltage versus the scan voltage is performed at regular time intervals during the experiment. From these curves f_{kepco} is deduced as the slope of each linear fit. The kepco factor used in the analysis was taken as an average number from all kepco scans performed during the experiment. For data obtained in 2010 it is found to be 50.4244 (8) and for 2012 50.4245 (16).

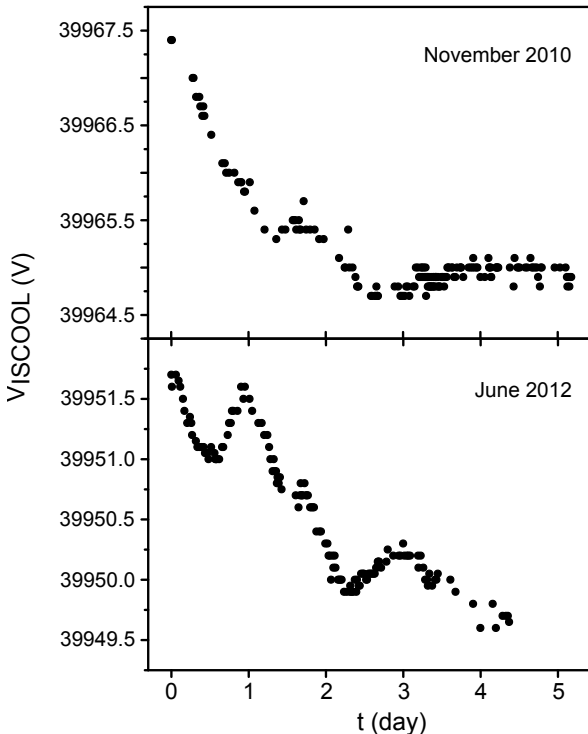


Figure 3.6: Shift in the Viscool recorded during the experiments. The total decrease in 2010 was about 3 V and in 2012 about 2.25 V.

After the conversion from voltage to frequency, the transition frequency of ^{39}K 389 286 058.716 (62) MHz [61] was subtracted from all frequencies. This means that all our hyperfine spectra are presented relative to that particular frequency. After the data were converted, the next step was finding the HFS peak positions, which can be described with the following formula:

$$\nu_{peak} = c_1 A(S_{1/2}) + c_2 A(P_{1/2}) + \nu_{centroid} \quad (3.7)$$

where the fit parameters are $A(S_{1/2})$ and $A(P_{1/2})$, the hyperfine parameters, and $\nu_{centroid}$ is the centroid (transition) frequency. The constants $c_{1,2}$ are calculated from Eq. (2.22) and they depend on the nuclear spin I. The peaks were fitted with a simple Voigt function, using the MINUIT package in ROOT [62]. After the individual files were fitted, the weighted mean value of the $A(S_{1/2})$ and $A(P_{1/2})$ parameters were calculated. It should be noticed that the final statistical uncertainty on the parameters from the individual files was calculated as the uncertainty from the fit multiplied by $\sqrt{\chi^2_{red}}$ in case of

$\chi^2_{red} > 1$. The uncertainty on the weighted mean value was taken as the higher number from the calculated statistical uncertainty:

$$\sigma_{stat} = \frac{1}{\sqrt{\sum_i \omega_i}} \quad (3.8)$$

and scatter error representing the scattering of the data around the weighted mean value:

$$\sigma_{scat} = \sqrt{\frac{1}{(N-1) \sum_i \omega_i} \sum_i \omega_i (x_i - \bar{x})^2} \quad (3.9)$$

where $\omega_i = 1/\sigma_i^2$.

In order to determine the isotope shift (IS) from Eq. (2.30), during the experiment the scans of the reference isotope (^{47}K) were saved before or after every scan of the isotope of interest. After the individual IS was determined, the weighted mean value with the uncertainties was found using the same equations. In addition, the systematic uncertainty on the isotope shift were also calculated in section 3.6.

3.2.4 Voltage calibration

The laser spectroscopy experiments aim for high precision results and as such, knowing the energy of the ion beam accurately is vital. From the specification of the voltage readout of ISCOOL, V_{ISCOOL} is obtained with 0.2% relative precision, which gives an error of about 80 V on 40 kV used during the experiments. Thus it is impossible to know V_{ISCOOL} to the required precision of about 1 V. Therefore we will use earlier measured isotope shifts to determine the correct absolute ISCOOL voltage. From earlier experiments it was known already that the value given by the readout is about 13 V higher than the real value. In order to determine this off-set more accurately, the conversion of the hyperfine spectra was performed using 4 different off-set values $V_{\text{ISCOOL}}^{\text{corr}} = V_{\text{ISCOOL}} - x$ where $x = 10, 12, 15, 18$ V and for each data set the isotope shift was determined. The data from 2010 were compared to the literature values [31]. It was found that the optimal correction voltage was 12.1 (13) V and in the final analysis -12 V was subtracted from V_{ISCOOL} . For the data from 2012, the results were compared to our results from the previous experiment. The optimal correction voltage of -14.8 (18) V was found, so the final analysis was performed with a correction voltage of -15 V. In Fig. 3.7 the difference in the isotope shift between the results before and after the calibration of V_{ISCOOL} is shown.

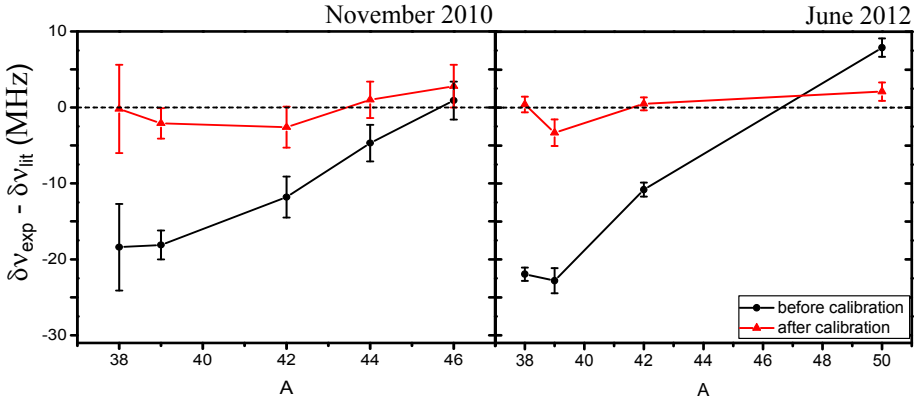


Figure 3.7: Difference in the isotope shift before (black symbols) and after (red symbols) voltage calibration. Left panel: Experimental isotope shift from data from 2010 compared to the literature values taken from [31]. Calibration was done by subtracting 12 V from V_{ISCOOL} . Right panel: Difference in the isotope shift between the data from 2012 and 2010. The optimal rescaling voltage was found to be -15 V. Lines are drawn only to guide the eye.

3.3 Line shape of the fitting

The Doppler broadening described in section 4.2.1 will be reflected in a larger Full Width at Half Maximum (FWHM) of the spectral line with a Gaussian profile. In addition, higher laser power causes the so-called power broadening described by a Lorentzian [63]. Thus, for the analysis of the hyperfine structure spectra, the Voigt function as a convolution of the Gaussian $G(t; \sigma)$ and Lorentzian $L(x - t; \Gamma_L)$ was used, as given by

$$V(x; \sigma, \Gamma_L) = \int_{-\infty}^{+\infty} G(t; \sigma) L(x - t; \Gamma_L) dt. \quad (3.10)$$

The Gaussian can be expressed as

$$G(t; \sigma) = \frac{1}{\sqrt{2\pi}\sigma} e^{-(x/2\sigma)^2} \quad (3.11)$$

where σ is related to the Full Width Half Maximum (FWHM) of the Gauss function via $\Gamma_G = 2\sqrt{2 \ln(2)}\sigma \approx 2.35482\sigma$.

The Lorentzian can be written as

$$L(x; \Gamma_L) = \frac{1}{\pi} \frac{\Gamma_L/2}{(\Gamma_L/2)^2 + x^2} \quad (3.12)$$

where Γ_L is a FWHM of the Lorentz function.

Due to the complexity of the integral given in Eq. (3.10), a number of different methods for approximation of the Voigt function have been developed over the years [64, 63, 65, 66]. According to the work of Thompson and co-authors [67], the FWHM of the Voigt function can be expressed as

$$\begin{aligned}\Gamma_V = & \left(\Gamma_G^5 + 2.69269 \Gamma_G^4 \Gamma_L + 2.42843 \Gamma_G^3 \Gamma_L^2 \right. \\ & \left. + 4.47163 \Gamma_G^2 \Gamma_L^3 + 0.07842 \Gamma_G \Gamma_L^4 + \Gamma_L^5 \right)^{1/5}.\end{aligned}\quad (3.13)$$

Instead of defining the Voigt function in the code, we used a pre-defined one from the ROOT library, preventing mistakes in the definition and in the error calculation on the fit parameters.

An example of all three functions is plotted in Fig. 3.8 : Voigt (black), Gauss (blue) and Lorentz (red).

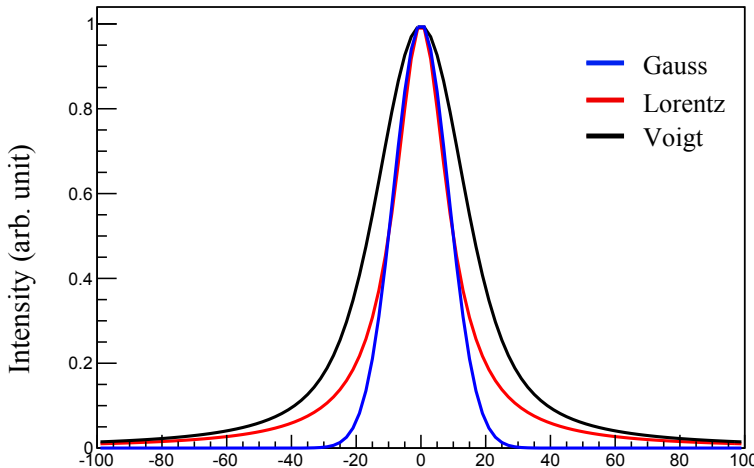


Figure 3.8: Comparison between three functions: Gauss (blue), Lorentz (red) and Voigt (black) for $\Gamma_G = \Gamma_L = 20$ MHz and $\Gamma_V = 32$ MHz. Intensities are normalized to 1.

In the plot, FWHM of the Gauss and Lorentz functions are given as $\Gamma_G = \Gamma_L = 20$ MHz yielding $\Gamma_V = 32$ MHz.

In the analysis, the Gaussian and Lorentzian widths were left as a free parameters in the fit, together with the background constant, the hyperfine parameters and the peaks intensities.

In parallel, K. Kreim carried out the analysis, where for every peak in the hfs spectrum a sum of one main peak and three sides peaks arising from the collisional excitations in the CEC was fitted [68]. The amplitude of the side peaks was fixed from the Poisson distribution and their relative positions were fixed to the excitation from $4s\ ^2S_{1/2} \rightarrow 5p\ ^2P_{1/2}$ corresponding to 3.06 eV from [69]. The extracted hyperfine parameters and the isotope shifts from the two measurements will be compared.

3.4 Results from the two experiments

In what follows, the results from both experiments of the potassium campaign are presented. In addition, the results obtained from the two different fit functions (single and multiple Voigt; details about multiple Voigt are given in Appendix B) are also compared. For isotopes where the hfs was measured during both experiments, the weighted mean value is shown.

The hyperfine parameters of the ground state, $A(S_{1/2})$, are presented in Table 3.2. Very good agreement is found for the results from different runs as well as different analysis. It should be noted here that in Article I (section 4.3), where the hyperfine parameters of $^{39,47,49,51}\text{K}$ were published, only the results from the simple Voigt analysis were considered. However, in the second publication included here as Article II (section 4.4) where the entire set of hyperfine parameters was published, for a few isotopes the results from both analysis were taken into account for earlier unpublished results on $^{38g,42,44}\text{K}$.

Table 3.2: Experimental results for the $A(S_{1/2})$ parameter from two sets of data (from 2010 and 2012) analyzed with a single Voigt, are compared to the results from multiple Voigt analysis (MV) and the literature values (^{38}K from [70], ^{42}K from [36] and others from [31]). Statistical uncertainties are given in the brackets.

isotope	I	$A(S_{1/2})$ (MHz)			Published	Literature
		2010	2012	MV		
^{38}K	3	+404.3 (4)	+404.2 (2)	+404.34 (13)	+404.3 (3)	+404.369 (3)
^{38m}K	0	0	0	0	0	-
39 K	3/2	+231.0 (3)	+231.8 (3)	+231.01 (27)	+231.0 (3)	+231.0 (3)
42 K	2	-503.8 (3)	-503.9 (3)	-503.59 (8)	-503.7 (3)	-503.550779 (5)
44 K	2	-379.0 (2)	-	-378.71 (15)	-378.9 (4)	-378.1 (11)
46 K	2	-462.8 (2)	-	-462.82 (14)	-462.8 (3)	-465.1 (12)
47 K	1/2	+3413.11 (50)	+3413.16 (21)	+3412.79 (17)	+3413.2 (3)	+3420.2 (29)
48 K	1	-795.9 (3)	-	-795.84 (29)	-795.9 (3)	-
48 K	2	-477.6 (2)	-	-	-	-
49 K	1/2	+2368.2 (14)	-	+2366.2 (11)	+2368.2 (14)	-
50 K	0	0	0	0	0	-
51 K	3/2	-	+302.5 (13)	+302.47 (143)	+302.5 (13)	-
51 K	5/2	-	+201.6 (9)	+201.65 (95)	+201.6 (9)	-
51 K	7/2	-	+151.3 (7)	-	+151.3 (7)	-

In the case of ^{39}K , the result from 2012 was not taken into account for the final value because it was obtained with high laser power. We have two sets of data for ^{39}K taken with two different laser powers. In the first case a laser power between 0.1 and 0.3 mW was used, while the other data set was recorded at a laser power of 1–1.3 mW. At the larger laser power a significant power broadening is observed leading to a larger Lorentz line width, due to which the upper hyperfine splitting is not resolved. For the files shown in Fig. 3.9, for low laser power $\Gamma_L = 11.5(22)$ MHz and $\Gamma_G = 33.1(20)$ MHz, while for the high laser power $\Gamma_L = 44.7(18)$ MHz and $\Gamma_G = 30.3(25)$ MHz were obtained. The deduced A parameter for the ground state splitting is slightly higher in the latter case, and this is consistently the case in all data files taken at high laser power.

The data for low and high laser powers, lead to $A(S_{1/2}) = 231.0(3)$ MHz and 231.8(3) MHz respectively. The obtained shift of +0.8(3) MHz illustrates that only at low laser power, when the upper fine structure levels are sufficiently resolved, the correct A parameter is found in agreement with the literature value which was used as reference value for magnetic moment calculation (230.8598601(7) MHz) [35]. In the Articles I and II (Sec. 4.3 and 4.4, respectively), the published result was obtained with low laser power. The results for the upper hyperfine splitting $A(P_{1/2})$ are 27.8(2) MHz (low) and 28.3(3) MHz (high).

^{51}K was only measured with high laser power during the experiment in 2012. However, due to fact that the ^{51}K A hyperfine parameter is about 50% larger than for ^{39}K , the lines are better resolved (see Fig. 3 in the Article II in Sec. 4.4), therefore we were able to obtain a reliable result for $A(S_{1/2})$.

The hyperfine splitting is larger for the other isotopes and the peaks are very well separated (see spectra of $^{38g,m}\text{K}$ in Article III (section 5.1); $^{42,44,46,47}\text{K}$ in Appendix C and $^{48–51}\text{K}$ in Article II (section 4.4)), thus it is not expected to see any influence of the laser power on the fitted A parameters. None of the other values is affected by the laser power that was used in the measurements, either because all lines were sufficiently resolved or because the statistical error includes a possible shift due to laser power, which is found to be +0.8(3) MHz between 0.3 mW and 1.3 mW.

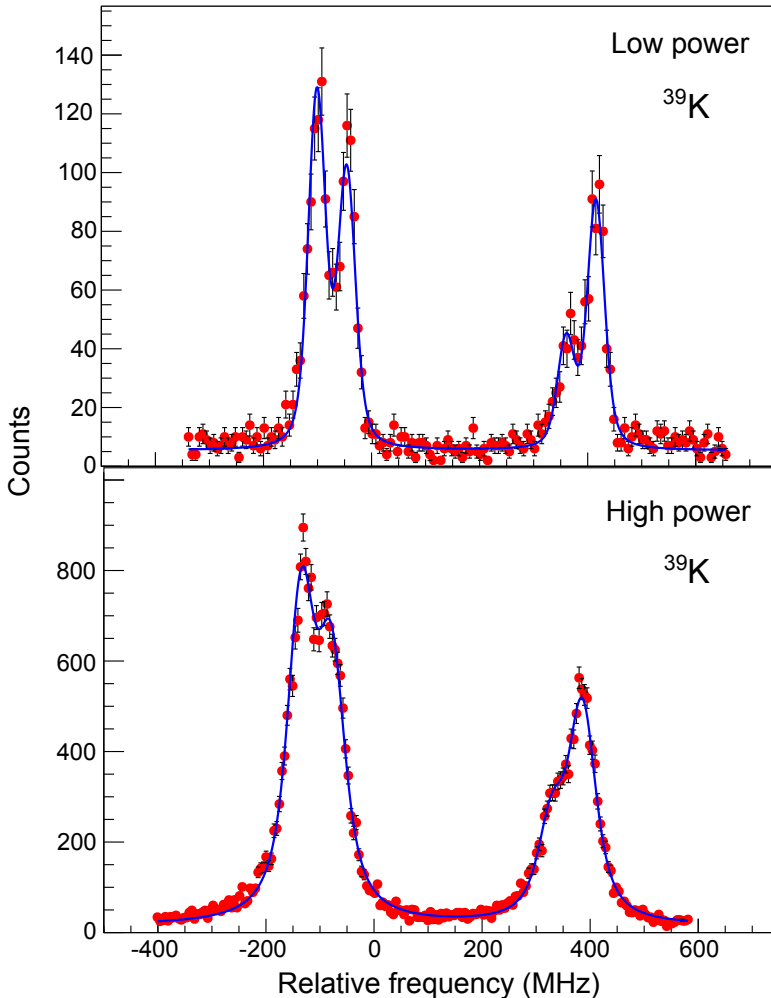


Figure 3.9: Hyperfine structure spectra of ^{39}K recorded with low laser power (upper panel) and high laser power (lower panel). Due to the power broadening caused by the high laser power, the four peaks in the hfs spectrum are not fully revolved. The fit resulted in $\chi^2_{\text{red}} = 1.4$ for NDF = 139 (low power) and $\chi^2_{\text{red}} = 2.2$ for NDF = 191 (high power).

In addition, for ^{47}K there is a clear discrepancy between the obtained values from our experiments and the published one by Touchard and co-authors [31]. In order to demonstrate the consistency of our value, the $A(S_{1/2})$ parameters of ^{47}K from all the files are shown in Fig. 3.10. The weighted mean value for $A(S_{1/2})$

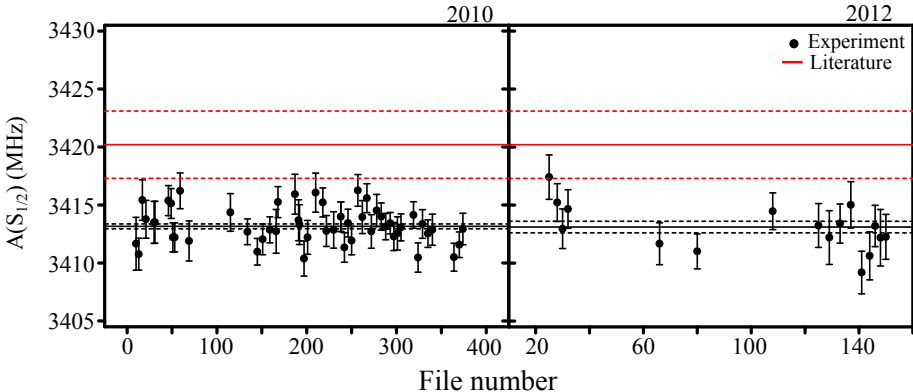


Figure 3.10: $A(S_{1/2})$ hyperfine parameters of ^{47}K from all files obtained during two runs: +3413.16 (21) MHz and +3413.11 (50) MHz from 2010 and 2012 run, respectively. The weighted mean values (black solid line) with $\pm \sigma$ regions are plotted as well (dashed black line).

(black solid line) from our experiments are found to be +3413.16 (21) MHz and +3413.11 (50) MHz from 2010 and 2012 run, respectively. The values are off from the value from an earlier publication which is 3420.2 (29) MHz (red solid line), but agree with it within 2 sigma of its error. In the figure, $\pm \sigma$ intervals are marked with dashed lines.

The hyperfine parameters of the excited state, $A(P_{1/2})$, obtained from two experiments are listed in Table 3.3. The results from the analysis of the single Voigt function are compared to the multiple Voigt analysis where very good agreement is found. The published results were those obtained from the fit with the single Voigt. The calculated isotope shift is shown in Table 3.4 and compared to the literature values. The published results in Article IV (Appendix A.1) are from the analysis with the multiple Voigt line shape.

Table 3 3: Experimental results for the $A(P_{1/2})$ parameter from two sets of data (from 2010 and 2012) which were analyzed with a single Voigt, are compared to the results from multiple Voigt analysis (MV) and the literature values taken from [31]. Statistical uncertainties are given in the brackets.

isotope	I	$A(P_{1/2})$ (MHz)			Literature
		2010	2012	MV	
^{38g}K	3	+48.8 (4)	+48.9 (2)	+48.78 (12)	+48.9 (2)
^{38m}K	0	0	0	0	-
^{39}K	$3/2$	+27.8 (2)	+28.3 (3)	+27.77 (27)	+27.8 (2)
^{42}K	2	-61.11 (23)	-61.3 (4)	-61.05 (16)	+61.2 (2)
^{44}K	2	-45.8 (2)	-	-45.80 (16)	-45.8 (2)
^{46}K	2	-55.9 (2)	-	-55.87 (13)	-55.9 (2)
^{47}K	$1/2$	+411.4 (4)	+411.9 (2)	+412.12 (14)	+411.8 (2)
^{48}K	1	-96.3 (2)	-	-96.21 (22)	-96.3 (3)
^{48}K	2	-57.8 (5)	-	-	-
^{49}K	$1/2$	+285.6 (7)	-	+287.0 (6)	+285.6 (7)
^{50}K	0	0	0	0	-
^{51}K	$3/2$	-	+36.6 (9)	+37.23 (95)	+36.6 (9)
^{51}K	$5/2$	-	+24.4 (6)	+24.82 (63)	+24.4 (6)
^{51}K	$7/2$	-	+18.3 (4)	-	+18.3 (4)

Table 3.4: Experimental results for the isotope shift from the two sets of data (2010 and 2012) which were analyzed with a single Voigt, are compared to the published results from a multiple Voigt analysis and the literature values [31, 32]. The isotope shift of ^{38m}K is calculated relative to ^{38g}K . Statistical uncertainties are given in the brackets.

isotope	I	2010	2012	Average	$\delta\nu^{A,47}$ (MHz)	Published	Literature
^{38g}K	3	-986.2(5)	-985.6(6)	-986.0(4)	-985.9(4)	-984.5(56)	
^{38m}K	0	-9.8(8)	-10.7(7)	-10.3(5)	-11.03(56)	-4(6)	
^{39}K	$3/2$	-859.7(6)	-862.6(16)	-860.0(6)	-862.5(9)	-857.5(17)	
^{42}K	2	-507.2(6)	-506.3(6)	-506.8(4)	-506.7(7)	-505.8(25)	
^{44}K	2	-292.4(6)	-	-292.4(6)	-292.1(5)	-293.2(22)	
^{46}K	2	-92.3(5)	-	-92.3(5)	-91.6(5)	-94.7(23)	
^{47}K	$1/2$	0	0	0	0	0	
^{48}K	1	+69.8(4)	-	+69.8(4)	+67.9(4)	-	
^{48}K	2	-0.19(4)	-	-0.19(4)	-	-	
^{49}K	$1/2$	+136.0(8)	-	+136.0(8)	+135.3(5)	-	
^{50}K	0	+207.7(7)	+209.1(8)	+208.3(7)	+206.5(9)	-	
^{51}K	$3/2$	-	+274.9(13)	+274.9(13)	+273.2(14)	-	
^{51}K	$5/2$	-	+297.0(14)	+297.0(14)	-	-	
^{51}K	$7/2$	-	+308.0(14)	+308.0(14)	-	-	

The reason for the deviation between the two analysis approaches obtained for the isotope shift in isotopes (or isomer) with $I = 0$ will be given in the next section. The discrepancy found in the isotope shift ^{48}K of about 2 MHz is still puzzling.

3.5 I = 0 spectra

As mentioned before, the FWHM of the Lorentzian component was different in the two sets of data recorded with different laser power as a result of power broadening. In the case of measurements with low laser power (2010 data), the FWHM of the Lorentzian component was found to be in the range from 25 up to 30 MHz, while for the data recorded with higher laser power (from 2012), this component was significantly larger, around 45 MHz. It should be noted that in the case of ^{48}K , almost 30% of the files were fitted with a lower limit on the $\sigma_G = 5$ MHz, based on the estimation for the Doppler width to be around 10 MHz. This caused the isotope shift to change by 0.1 MHz (negligible), while the A hyperfine parameters were unaffected. The FWHM of the Gaussian component in both data sets was around 30 MHz.

During the analysis it was noticed that the FWHM of the Lorentzian component for $I = 0$ isotopes, ^{38m}K and ^{50}K , was significantly larger than the values obtained for other isotopes. The reason for this is still not understood. In order to demonstrate this particular effect, we will focus on the following ratios:

$$R_L = \frac{\Gamma_L(^{47}\text{K})}{\Gamma_L(^A\text{K})} \quad \text{and} \quad R_G = \frac{\Gamma_G(^{47}\text{K})}{\Gamma_G(^A\text{K})}. \quad (3.14)$$

Calculated ratios for three independent files for isotopes which were measured in both experiments are listed in Table 3.5 for isotopes with $I \neq 0$ and in Table 3.6 for isotopes with $I = 0$.

In order to investigate the influence of the different line shapes used in the fit on the isotope shift, reanalysis of the data for $^{38g,38m,42,50}\text{K}$ was performed, with the line profile where the three side peaks were included (see Appendix B for details). The side peaks correspond to the multiple collisional excitations. It yielded the isotope shift of ^{38m}K and ^{50}K to be -10.8 (5) MHz and 206.5 (5) MHz, respectively (as published in Kreim *et al.*, [51] Article IV in Appendix A.1). The isotope shift from the single Voigt analysis is found to be -10.3 (5) MHz and 208.3 (7) MHz for ^{38m}K and ^{50}K , respectively. In order to check the influence of the line shape on the values extracted from isotopes with $I \neq 0$, the hfs spectra of ^{38}K and ^{42}K were also refitted. There was no change of the A hyperfine parameters and the obtained isotope shift for ^{38g}K and ^{42}K was changed within error bars, -985.6 (3) MHz and -506.2 (3) MHz for these two isotopes, respectively.

Table 3.5: Ratios of the Lorentzian and Gaussian FWHM between isotopes with $I \neq 0$ and reference isotope for some of the files are listed. The data shows very good consistency with $R = 1$.

Experiment	^{38g}K		^{42}K	
	R_L	R_G	R_L	R_G
2010	0.91 (17)	0.94 (15)	1.10 (13)	0.95 (11)
	0.87 (16)	0.93 (16)	1.3 (3)	0.87 (11)
	1.16 (24)	0.91 (15)	0.88 (16)	0.95 (15)
2012	0.77 (7)	1.75 (10)	1.04 (7)	1.17 (13)
	1.02 (13)	1.14 (21)	1.13 (9)	1.00 (11)
	1.15 (16)	0.86 (19)	1.23 (9)	0.86 (13)

Table 3.6: Ratios of the Lorentzian and Gaussian FWHM between isotopes with $I = 0$ and reference isotope for some of the files are listed. From the data, a clear deviation from $R = 1$ is found for the Lorentzian line width.

Experiment	^{38m}K		^{50}K	
	R_L	R_G	R_L	R_G
2010	3.0 (6)	0.94 (25)	1.7 (2)	2.3 (9)
	1.1 (6)	1.3 (6)	1.7 (3)	1.6 (4)
	5.0 (8)	0.79 (10)	2.5 (14)	1.05 (15)
2012	4.4 (2.3)	1.15 (11)	2.7 (5)	1.12 (12)
	2.2 (5)	1.4 (3)	3.2 (6)	1.41 (12)
	2.8 (6)	1.0 (2)	3.3 (7)	1.09 (16)

The single Voigt analysis yielded -986.0 (4) MHz for ^{38g}K and -506.8 (4) MHz for ^{42}K .

An example of the fit is depicted in Fig. 3.11. Line widths for this particular fit with the single Voigt $\Gamma_L = 18.6$ (29) MHz and $\Gamma_G = 11.8$ (13) MHz, while for the multiple Voigt profile it was $\Gamma_L = 12.0$ (22) MHz and $\Gamma_G = 8.1$ (12) MHz. The obtained reduction of χ^2_{red} by 0.35 was found once the multiple Voigt was used.

However, not all peaks had such nice profile for $I = 0$ cases. During the fitting procedure, it was noticed that in some of the files, when the distance between the side peaks was fixed, Γ_L or σ_G appeared at the limit of 5 MHz. It should be mentioned that in the analysis of the 2010 data performed by K. Kreim, Γ_L was fixed to the mean value of ^{47}K , while in the results presented in this thesis it was free with a lower limit of 5 MHz.

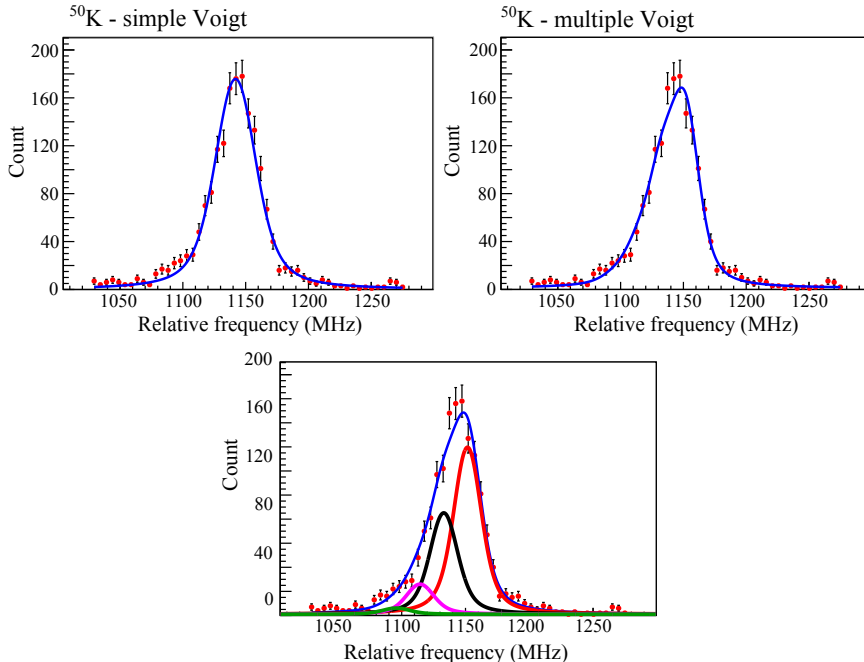


Figure 3.11: (Upper panel) Comparison between single (left) and multiple (right) Voigt line shape fitting the same file of ^{50}K . Decrease of the χ^2_{red} was obtained by introducing three side peaks, from 1.70 to 1.35 for the same NDF = 46. (Lower panel) All peaks are shown: the main in red without collisional excitations and three from the multiple collisional excitations ($n = 1, 2, 3$) in black, purple and green, respectively.

3.6 Systematic uncertainties

The uncertainties on the parameters used for the conversion of the data from voltage to frequency (Eq. (3.5)) induces a systematic uncertainty on the isotope shift. In order to estimate it, the error on V_{ISCOOL} was taken as 1.3 V or 1.8 V as described in Sec. 3.2.4, while for V_{offset} the error was estimated to be 0.05 V. The uncertainties for the kepcos factors are given in Sec. 3.2.3, while the errors related to the isotope masses are listed in Table 1.1. The uncertainty of the wavenumber λ^{-1} , as measured by the laser wavelength meter, is 0.002 provided by the manufacturer (Bristol instruments; 621A Series). This parameter yielded a systematic uncertainty of around $5 \cdot 10^{-4}$ MHz for all isotopes, thus its contribution to the total error can be neglected. For isotopes which were measured in both experimental campaigns, the standard error propagation

methods have been applied. Furthermore, as it was shown in section 3.5, the line shape (simple Voigt or with side peaks) used in the fitting procedure also introduces a shift, yielding an additional systematic error for the $I = 0$ isotope/isomer of 1.5 MHz, while for the other isotopes this was 0.5 MHz. Finally, all these uncertainties combine into a total error on the isotope shift, which is presented in Table 3.7. Based on these numbers, the errors related to V_{ISCOOL} and the fitted line shape dominate the systematic uncertainties.

Table 3.7: Systematic error budget of the isotope shift relative to ^{47}K . For the final value, the results from the line shape and V_{ISCOOL} were used. Results are presented in MHz.

Isotope	V_{ISCOOL}	V_{offset}	f_{kepc}	m	Line shape	Total
$^{38}\text{K}^g$	3.34	0.106	0.026	0.010	0.7	3.4
$^{38}\text{K}^m$	3.34	0.106	0.026	0.010	2.1	4.0
^{39}K	2.88	0.091	0.023	0.011	0.7	3.0
^{42}K	1.67	0.053	0.013	0.011	0.7	1.8
^{44}K	0.53	0.021	0.003	0.005	0.5	0.7
^{46}K	0.14	0.006	0.009	0.004	0.5	0.5
^{48}K	0.21	0.008	0.0013	0.004	0.5	0.5
^{49}K	0.37	0.014	0.0022	0.004	0.5	0.6
^{50}K	0.88	0.028	0.007	0.048	2.1	2.3
^{51}K	0.91	0.025	0.008	0.065	0.5	1.0

3.7 Hyperfine structure anomaly

In cases where the A hyperfine parameter is measured at a relative precision of 10^{-3} - 10^{-4} , the effect called the hyperfine structure anomaly has to be taken into account when deducing the nuclear magnetic moment (or g factor). It arises from the fact that a nucleus has a finite size and should not be considered as point-like, due to which the magnetic hyperfine field - induced by electrons penetrating the nucleus - is not constant over the nuclear volume. Thus the magnetic hyperfine field becomes isotope dependent and the ratio of A-parameters is not exactly equal to the ratio of the g factors. This only happens for $s_{1/2}$ electrons and in heavier elements, for relativistic electrons from the $p_{1/2}$ shell. The hfs anomaly is caused by two effects:

- The extended distribution of the magnetization over the nuclear volume called the Bohr-Weisskopf effect [71, 72].

- The extended nuclear charge distribution which modifies the electron wave function, called the Breit-Rosenthal effect [73].

The Breit-Rosenthal effect can be neglected for heavier alkali elements [74], thus we will consider that the main cause of the hfs anomaly is the distribution of the magnetization.

Due to the hfs anomaly, the A hyperfine parameters are slightly modified for each isotope: $A = A_{\text{point}}(1 + \epsilon)$, where A_{point} is a hyperfine parameter for a point nucleus and ϵ is an isotope dependent perturbation factor. This causes the ratio of the A parameters to be no longer equal to the ratio of the g factors, as it is given in Eq. (2.28), and an additional uncertainty on the g factors has to be addressed. The hfs anomaly can be expressed as

$${}^1\Delta^2 = \frac{A_1}{A_2} \frac{g_2}{g_1} - 1 \quad (3.15)$$

where A_i represents the hyperfine parameter of the same state from two isotopes $i = 1, 2$ and g_i is the g factor ($g = \mu/I$) for these isotopes.

The first hyperfine structure anomaly was published by F. Bitter as the observation of the hfs of Rb isotopes [75], while theoretical work was performed by Bohr and Weisskopf [71]. In the latter it was suggested that the measured spins and magnetic moments (for ${}^{85}\text{Rb}$: $I = 5/2$, $\mu = 1.35 \mu_N$, while for ${}^{87}\text{Rb}$: $I = 3/2$, $\mu = 2.75 \mu_N$) for the two isotopes would point to a very different distribution of their magnetization, causing a large hyperfine structure anomaly.

In this thesis, the hfs anomaly was estimated from the experimental A parameters via a differential hfs anomaly as well as by following the theoretical approach proposed by Bohr.

Differential hfs anomaly

Considering two different electronic states with the total angular momenta J_1 and J_2 , and assuming that $\left(\frac{g_1}{g_2}\right)_{J_1} = \left(\frac{g_1}{g_2}\right)_{J_2}$, a differential hyperfine anomaly between these two electronic states is defined [76] as

$${}^1\delta^2 = {}^1\Delta_{J_1}^2 - {}^1\Delta_{J_2}^2 = \left(\frac{A_1}{A_2}\right)_{J_1} \left(\frac{A_2}{A_1}\right)_{J_2} - 1 \quad (3.16)$$

The differential hfs anomaly in the potassium chain was deduced considering the $S_{1/2}$ and $P_{1/2}$ states, relative to ${}^{39}\text{K}$ with the values taken from Ref. [35, 61]. For other isotopes, the A parameters listed in Table 3.2 and 3.3 were used. In addition, the differential hfs anomaly of ${}^{40,41}\text{K}$ was calculated from

the A parameters obtained in [35, 37, 61]. Due to the lack of information about $A(P_{1/2})$, the anomaly was not calculated for $^{43,45}\text{K}$. The results of the calculations are listed in Table 3.9 and in Table II (column 3) in the Article II (section 4.4). It should be noted that the hfs anomaly in this case can be approximated to a few percent by the differential hfs anomaly, which is good enough taking into account the accuracies of our experimental results.

Estimation of hfs anomaly

In order to estimate the hfs anomaly, the theory presented by Bohr was followed. The model assumes that the nuclei of interest can be described as a single particle moving in the potential of the deformed core, while the magnetic moment depends on the strength of the coupling between the odd nucleon and the core [72]. Here, the anomaly was expressed as the difference between the perturbation factors of two isotopes

$${}^1\Delta_{\text{theo}}^2 = \epsilon(1) - \epsilon(2) \quad (3.17)$$

where the perturbation ϵ factor was calculated from the following relation

$$\epsilon = -[(1 + 0.38\zeta)\alpha_s + 0.62\alpha_L]b(Z, R_0)(R/R_0)^2 \quad (3.18)$$

in which $b(Z, R_0)$ is given as 0.19% in [72] for all potassium isotopes, $(R/R_0)^2$ was 0.66 (R represents the distance from a central charge and R_0 is the nuclear radius). α_s and α_L are the fraction of the nuclear moment of spin and orbital type, respectively and are calculated as

$$\alpha_s = \frac{\sigma g_s}{(I+1)g_I} \quad \text{and} \quad \alpha_L = 1 - \alpha_s. \quad (3.19)$$

The parameter σ is the average value of the odd particle spin component along the nuclear axis and is calculated as

$$\sigma = \frac{(I+1)g_I - g_R - Ig_L}{g_s - g_L} \quad (3.20)$$

where $g_R = 0.5$ was used and it represents the g factor for the nuclear rotation, $g_L = 1$ is the orbital g factor and $g_s = 5.586$ the spin g factor. Finally, the nuclear g factor is presented with g_I and it is calculated for every isotope from the measured magnetic moment.

The last parameter from Eq. (3.18), ζ expresses the angular asymmetry in the spin distribution. The model assumes intermediate spin-orbit coupling, which means that it is between the very strong spin-orbit coupling and the spin-orbit coupling which is smaller than the coupling of l to the nuclear axis, but still

larger energy than the rotational level spacing. For this, Bohr suggested the following equation:

$$\zeta = \frac{1}{4(I+2)} \frac{1}{\beta^2 - 1} (\beta^2(2I+1) - 6\beta(2I+1)^{1/2} - 2I + 5) \quad (3.21)$$

where β is defined as

$$\beta = -\sqrt{\frac{1-2\sigma}{1+2\sigma}} \quad (3.22)$$

Finally, once the ϵ from Eq. (3.18) is calculated for two isotopes, the hyperfine anomaly was obtained from Eq. (3.17).

For even- A potassium isotopes where negative magnetic moments were observed, the described procedure would lead to $\frac{1-2\sigma}{1+2\sigma} < 0$, thus another expression was used instead of Eq. (3.21):

$$\zeta = \frac{2I+1}{4(I+2)} \quad \text{for } j = l - 1/2 \quad (3.23)$$

Only ^{38}K has a positive magnetic moment ($\mu = +1.3711 \mu_N$), thus it was possible to calculate the hfs anomaly using Eq. (3.21) which resulted in almost the same value, $^{39}\Delta^{38} = 0.15\%$.

For the odd- A isotopes with $I = 1/2$, namely $^{47,49}\text{K}$, due to the same issue the ζ parameter was calculated from

$$\zeta = \frac{2I-1}{4(I+1)} \quad \text{for } j = l + 1/2. \quad (3.24)$$

Results from the theoretical calculations of the hfs anomaly for the entire chain of potassium isotopes are listed in Table 3.8.

Table 3.8: Hyperfine structure anomaly estimated from the approach proposed by Bohr. All parameters from the intermediate steps are also listed. See the text for more details.

isotope	I	σ	α_s	β	ζ	ϵ (%)	${}^{39}\Delta_{\text{theo}}^A$ (%)
${}^{38}\text{K}$	3	-0.365	-1.114	-	0.350	-0.006	0.17
${}^{39}\text{K}$	3/2	-0.294	-2.516	-1.962	1.026	0.165	-
${}^{40}\text{K}$	4	-1.335	4.600	-	0.375	-0.379	0.54
${}^{41}\text{K}$	3/2	-0.358	-5.585	-2.458	0.789	0.398	-0.23
${}^{42}\text{K}$	2	-0.918	3.001	-	0.313	-0.265	0.43
${}^{43}\text{K}$	3/2	-0.377	-7.733	-2.667	0.730	0.560	-0.39
${}^{44}\text{K}$	2	-0.825	3.588	-	0.313	-0.302	0.47
${}^{45}\text{K}$	3/2	-0.373	-7.211	-2.623	0.741	0.521	-0.36
${}^{46}\text{K}$	2	-0.887	3.158	-	0.313	-0.275	0.44
${}^{47}\text{K}$	1/2	1.044	1.008	-	0.000	-0.126	0.29
${}^{48}\text{K}$	2	-0.719	2.233	-	0.250	-0.211	0.38
${}^{49}\text{K}$	1/2	0.658	0.915	-	0.000	-0.121	0.29
${}^{51}\text{K}$	3/2	-0.250	-1.632	-1.731	1.244	0.097	0.07

In the earlier publication from 1950 [71], Bohr and Weisskopf suggested the relation for an approximation of the hfs anomaly

$$\Delta_{\text{app}} \approx 0.3b \frac{g_s g_L}{g_s - g_L} \left(\frac{1}{g_1} - \frac{1}{g_2} \right). \quad (3.25)$$

The complete derivation of Eq. (3.25) is given in the same reference. Due to the simplicity of the approximation, these data were not used in the publication. However, just for the simple check, they are listed in the Table 3.9 together with other values for the hfs anomaly obtained with other approaches and the results from the literature.

The results for the hfs anomaly of the potassium isotopes estimated from the different approaches are compared to the experimental differential values in Fig. 3.12. A very good agreement is found between the approximation and the more exactly calculated hyperfine anomaly, as well as with the experimentally determined values (which have rather large error bars).

Table 3.9: Summary of the estimated hfs anomalies from different approaches compared to the ones from literature [70, 36, 35, 37, 77]. Differential hfs anomalies calculated from the experimental results (Eq. (3.16)) are presented in third column. The hfs anomalies base on theory (Eq. (3.17)) are shown in the next column, while the values from the simple approximation (Eq. (3.25)) are listed in the fifth column. In the last column, hfs anomalies from the literature are presented.

isotope	I	$^{39}\delta^A$ (%)	$^{39}\Delta^A_{\text{theo}}$ (%)	$^{39}\Delta^A_{\text{app}}$ (%)	$^{39}\Delta^A_{\text{lit}}$ (%)
^{38}K	3^+	0.53 (44)	0.17	0.11	0.17 (6)
^{40}K	4^-	0.43 (17)	0.54	0.48	0.466 (19)
^{41}K	$3/2^+$	-0.23 (31)	-0.23	-0.22	-0.226 (10)
					-0.22936 (14)
^{42}K	2^-	0.99 (36)	0.43	0.39	0.336 (38)
^{43}K	$3/2^+$	-	-0.39	-0.37	-
^{44}K	2^-	0.47 (47)	0.47	0.43	-
^{45}K	$3/2^+$	-	-0.36	-0.33	-
^{46}K	2^-	0.40 (39)	0.44	0.40	-
^{47}K	$1/2^+$	0.28 (16)	0.29	0.25	-
^{48}K	1^-	0.57 (35)	0.38	0.34	-
^{49}K	$1/2^+$	0.24 (29)	0.29	0.24	-
^{51}K	$3/2^+$	0.57 (250)	0.07	0.06	-

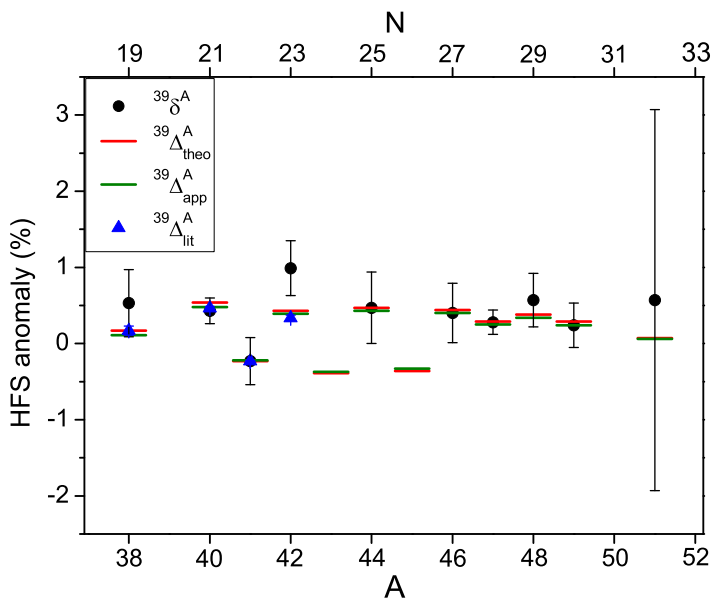


Figure 3.12: Differential (experimental) hyperfine structure anomaly (black dots; Eq. (3.16)) compared to the theoretically estimated hfs anomaly (red lines; Eq. (3.17)), approximated values (green lines; Eq. (3.25)) and the experimentally observed values found in the literature (blue triangles) taken from [70, 36, 35, 37, 77].

Chapter 4

Nuclear structure of potassium isotopes based on spins and magnetic moments

This chapter will focus on the interpretation of the nuclear structure based on comparison between our measurements and theory in the shell-model framework. We will start with the description of the monopole interaction as a continuation of the shell model which is presented in the first chapter. Furthermore, large-scale shell-model calculations will be introduced in more details. The discussion will be presented as two published articles which are included. As an additional information, some unpublished material from the calculations will be given here as well.

4.1 Monopole interaction

In the independent particle model, which is based on the assumption that the noninteracting nucleons are placed in the orbits of the spherically symmetric potential produced by all nucleons, the Hamiltonian is given as $H = H_0$ defined in Eq. (1.2) by neglecting H_{res} . This model is capable of reproducing the correct shell gaps as well as providing information about the nuclear structure of the nuclei with one particle (hole) next to a closed shell. However, for more complex systems, the nucleus is considered to have an inert core (closed shell for protons and neutrons) and the nucleons outside the core are called valence particles. In

this case, H_{res} as defined in Eq. (1.2), has to be taken into account. It describes the interaction between the valence nucleons outside the core, and this residual interaction will depend on the model space that is considered.

For simplicity, we will first consider an example of two valence particles placed in orbits with spin j_1 and j_2 which are coupled to a total spin J , $|j_1 - j_2| \leq J \leq j_1 + j_2$ for $j_1 \neq j_2$. By solving the Schrödinger equation of the Hamiltonian given in Eq. (1.2) for $i = 1, 2$, the energy of the two-particle states as multiplet for different J values can be obtained as

$$E(j_1, j_2; J) = \epsilon_{j_1} + \epsilon_{j_2} + \langle j_1, j_2; J, T | H_{\text{res}} | j_1, j_2; J, T \rangle \quad (4.1)$$

where $\epsilon_{j_1} + \epsilon_{j_2}$ are the single particle energies and T in the equation stands for isospin. The effect of the residual two-body interaction between the particles is expressed via the last term in Eq. (4.1), it is called the two-body matrix elements (TBME) and will be a parameter defining the residual interaction in the shell model calculations.

Applying the multipole expansion to the Hamiltonian of the residual interaction yields

$$H_{\text{res}} = H_{\text{mon}} + H_{\text{mult}} \quad (4.2)$$

where the monopole term, H_{mon} , contributes to the spherical mean field; the multipole term, H_{mult} , contains all other higher terms from the expansion and can include pairing correlations, quadrupole-quadrupole interactions and others, which are responsible for the deformations observed in ground-state properties of nuclei. In this thesis, only the monopole term will be discussed further. More details about the multipole term can be found in Ref. [78, 79].

Combining the H_0 defined in Eq. (1.2) and the H_{mon} from Eq. (4.2), one can rewrite them in the particle number operator ($\hat{n} = \hat{a}^+ \hat{a}$ where \hat{a}^+ is a creation operator, while \hat{a} is a annihilation operator) representation as:

$$\begin{aligned} \hat{H}_0 + \hat{H}_{\text{mon}} &= \sum_{j_1} \epsilon_{j_1}^\pi \hat{n}_{j_1}^\pi + \sum_{j_1} \epsilon_{j_1}^\nu \hat{n}_{j_1}^\nu + \sum_{j_1 j_2} V_{j_1 j_2}^{\pi \nu} \hat{n}_{j_1}^\pi \hat{n}_{j_2}^\nu \\ &+ \sum_{j_1 \leq j_2} V_{j_1 j_2}^{\pi \pi} \frac{\hat{n}_{j_1}^\pi (\hat{n}_{j_2}^\pi - \delta_{j_1 j_2})}{1 + \delta_{j_1 j_2}} + \sum_{j_1 \leq j_2} V_{j_1 j_2}^{\nu \nu} \frac{\hat{n}_{j_1}^\nu (\hat{n}_{j_2}^\nu - \delta_{j_1 j_2})}{1 + \delta_{j_1 j_2}} \end{aligned} \quad (4.3)$$

where $V_{j_1 j_2}^{\tau \tau'}$ is the averaged TBME's via a $(2J + 1)$ factor over all possible J which arises from coupling between j_1 and j_2 . It is also called the centroid of the TBME for a certain J and T . The centroids of the unlike nucleons ($V^{\pi \nu}$) are twice stronger than those from like nucleons ($V^{\pi \pi, \nu \nu}$) [8]. Starting from the general expression for the centroids [78], the term which originates from the

proton-neutron interaction can be written as:

$$V_{j_1 j_2}^{\pi \nu} = \frac{\sum_J (2J+1) \langle j_1 j_2; JM | H_{\text{res}} | j_1 j_2; JM \rangle}{\sum_J (2J+1)} \quad (4.4)$$

where the two interacting nucleons are placed in orbits j_1 and j_2 . This term has a crucial role in the evolution of the shell structure which will be discussed further (see Sec. 4.2).

In the shell-model framework, the one-nucleon separation energy from an orbit which is completely occupied is called the effective single-particle energy (ESPE). Due to its linear dependence with the occupation number, $\Delta\epsilon_{j_1} = n(j_2)V_{j_1 j_2}^{\pi \nu}$ where $0 \leq n(j_2) \leq 2j_2 + 1$, the ESPEs are often used in the theoretical studies to present the evolution of the orbitals in an isotopic or isotonic chain.

In the previously described case, two valence particles could be found only in the two orbitals (j_1 and j_2). Next step is to expand the model space by considering more single-particle states which can be occupied. In this case, it is not only possible to extend the range of the possible J , but also more configurations could lead into the same value of J . In addition, scattered nucleons into different orbitals and coupled into certain J values create a wave function which is not pure anymore, but more fragmented. This effect is called configuration mixing. The Hamiltonian can be constructed for every J value as:

$$H = \begin{bmatrix} H_{11} & H_{12} & \cdots & H_{1n} \\ H_{21} & H_{22} & \cdots & H_{2n} \\ \vdots & \vdots & \ddots & \vdots \\ H_{n1} & H_{n2} & \cdots & H_{nn} \end{bmatrix} \quad (4.5)$$

where every element is described as:

$$H_{lk} = E_k^{(0)} \delta_{lk} + {}_l \langle j_1 j_2; JT | H_{\text{res}} | j_3 j_4; JT \rangle_k \quad (4.6)$$

with $E_k^{(0)}$ being the sum of the single-particle energies ($2\epsilon_j$), Kronecker delta is defined as $\delta_{lk} = 0$ for $l \neq k$ and 1 for $l = k$. The states ${}_l \langle j_1 j_2; JT |$ and $| j_3 j_4; JT \rangle_k$, with j_1 (j_3) and j_2 (j_4) coupled to the total spin J . The diagonal elements in the Hamiltonian from Eq. (4.5) represent the single-particle energies which are shifted due to the monopole part of the residual interaction. TBME between different configurations coupled to J are placed on off-diagonal positions. After the diagonalization of H and solving the Schrödinger equation, energy eigenvalues and eigenfunctions can be obtained for particular J states.

Finally, we can extend our case to the multiparticle configurations where n ($n > 2$) valence particles are considered in the model space. In order

to simplify the shell-model calculations for such complex case, the problem should be reduced to the level where only two-body interactions are taken into account. This can be done by a method which involves the coefficients of fractional parentage (CFP) defined below and gives a probability that the n -particle wave function $|j^n JM\rangle$ can be rewritten as a combination of the $(n-2)$ -particle configuration $|j^{n-2} J_{n-2} M_{n-2}\rangle$ coupled to the two-particle configuration $|j^2 J_2 M_2\rangle$ [6]:

$$|j^n JM\rangle = \sum_{J_2, J_{n-2}} \underbrace{\langle j^n J | j^2 (J_2) j^{n-2} (J_{n-2}) J \rangle}_{CFP} |j^2 (J_2) j^{n-2} (J_{n-2}) JM\rangle. \quad (4.7)$$

The CFPs are normalized as

$$\sum_{J_2, J_{n-2}} (CFP)^2 = 1. \quad (4.8)$$

4.2 Large-scale shell-model calculations

Theoretical calculations are crucial in the interpretation and understanding of the experimental results in the field of nuclear structure research. For the light and mid-mass region, the shell-model calculations have shown great success around shell closures. There are different codes for the shell-model calculations such as ANTOINE [80], NuShellX [81], etc. These codes can handle a large valence space. For example, the dimension of the matrices in the ANTOINE code goes up to 10^9 [78].

During the calculations, following steps have to be performed:

- Defining an inert core, a set of nucleons which will not influence the calculated results. One could consider them as "frozen" nucleons.
- Defining a number of valence nucleons and a valence space. The valence space is also called the "model space" and it represents the orbitals which are taken into account in the calculations. As it is shown in Fig. 4.1, protons and neutrons do not have to have the same model space.
- The valence space will depend also on the parametrization of the "effective residual interaction" that is used. Thus, an effective interaction is always designed for a well-defined model space.
- Defining which J^π should be considered.
- Constructing the Hamiltonian based on the information from the interaction file about the single-particle energies and the two-body matrix elements (TBME).

- Diagonalizing the Hamiltonian; leading to the eigenfunction (wave function) and energy eigenvalues.
- Calculated results such as energy spectra, nuclear moments, transition probabilities, occupation of the orbits, wave function composition, etc. are stored in the output file.

It is essential to note that a general interaction which would be suitable for computing all nuclei does not exist. Thus, one has to make sure that the model space which is used corresponds to the right effective interaction. Furthermore, limits of the model space will lead to quenching of the electrical charges and g factors. These new values are called effective charges and effective g factors. They are introduced to account for the interactions between nucleons from the core and valence nucleons as well as among valence nucleons and in addition, to match the experimental results. In the calculations performed for the potassium isotopes, the following effective g factors were used: $g_{s,\text{eff}}^{\pi,\nu} = 0.85g_{s,\text{free}}^{\pi,\nu}$, $g_l^\pi = 1.15$ and $g_l^\nu = -0.15$.

Experimental results from this thesis are compared to the shell-model calculations carried out by the ANTOINE code. Two phenomenological effective interactions were used: SDPF-NR [82, 83] and SDPF-U [84]. The fact that they are phenomenological means that their two-body matrix elements, as well as the single-particle energies, were tuned to the experimental data. More precisely, in order to obtain the effective interaction, the TBMEs and SPEs are left as free parameters and their values are determined by a fit to a large set of experimental data. This is the reason why these kind of interactions are applicable only locally.

For both interactions, ^{16}O was used as a core and the model space was containing the full sd shell for the protons and the full sd or pf shell for the neutrons. In addition, neutron excitations across the $N = 20$ shell gap were forbidden. A schematic representation of the used model space is shown in Fig. 4.1. In order to build the SDPF-NR interaction [82], the authors used parts from already existing interactions with some modifications. For the sd shell, the USD interaction [85] was employed. Furthermore, the TBME for pf shell were taken from a modified version of the KB' interaction (Kuo-Brown) [86]. Finally, the connection between the two shells was made via cross-shell TBME from G matrix of Lee, Kahanna and Scott (LKS) [87]. The latter were also additionally modified by fitting to the experimental data of nuclei from the region. More precisely, to the natural parity states of nuclei with a few holes in sd and a few particles in fp shells. Moreover, the evolution of the $1/2^+$ and $3/2^+$ states in K isotopes was also used as well as the position of the $5/2^+$ in ^{47}K .

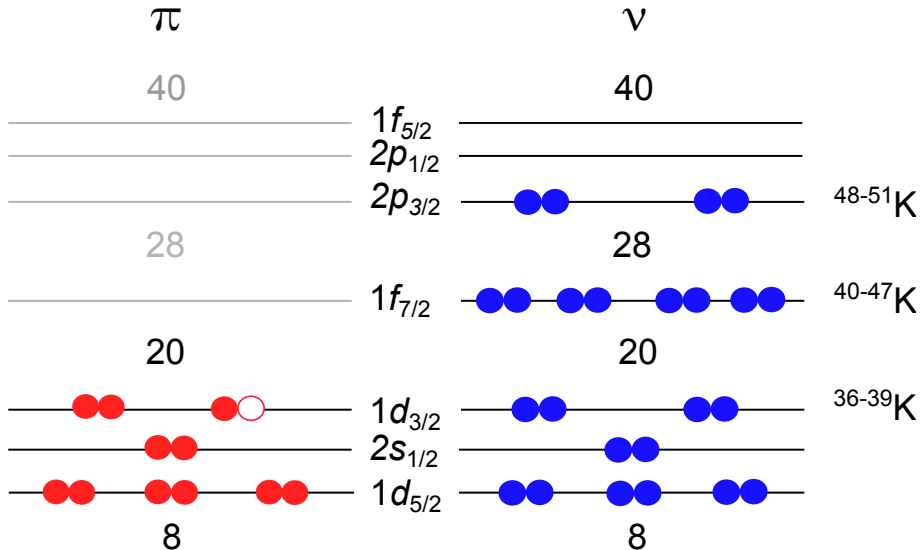


Figure 4.1: Model space used in the shell-model calculations. ^{16}O was used as a core; 11 protons were located in the sd shell, while neutrons occupied the full sd and fp shells, but excitations across $N = 20$ were prohibited.

After more experimental information was obtained, the authors re-fitted the interaction focusing on nuclei with one particle (hole) next to a shell closure: $^{35}_{14}\text{Si}_{21}$, $^{47}_{18}\text{Ar}_{29}$ and $^{41}_{20}\text{Ca}_{21}$. In addition, all $T = 0, 1$ sd - pf centroids were changed by -0.045 MeV and all $T = 1$ pf - pf by -0.250 MeV. This upgraded interaction is called SDPF-U, and its performance will be evaluated by comparing to our data as will be discussed in following paragraphs.

In order to demonstrate the differences between SDPF-NR and SDPF-U interaction, the effective single-particle energies (ESPE) will be considered. They are defined as the one-nucleon separation energy of the particular orbit calculated from the single-particle energy (SPE) and adding a monopole shift due to the nucleon-nucleon interaction (diagonal TBME). The SPE for our model space are presented in Table 4.1. For both interactions, all SPE are the same, except for the $1f_{5/2}$ orbital.

Table 4.1: Bare single-particle energies for orbitals from the model-space used in the shell-model calculations.

interaction	$1d_{5/2}$	$2s_{1/2}$	$1d_{3/2}$	$1f_{7/2}$	$2p_{3/2}$	$2p_{1/2}$	$1f_{5/2}$
SDPF-NR	-3.699	-2.915	1.895	6.22	6.314	6.479	10.95
SDPF-U	-3.699	-2.915	1.895	6.22	6.314	6.479	11.45

The ESPEs are calculated then as the difference in binding energy, BE , relative to the doubly magic nucleus, they are listed in Table 4.2 and 4.3 for SDPF-NR and SDPF-U, respectively. The energy gap between $\pi(1d_{3/2}-2s_{1/2})$ is also given in the last column in both tables. Additionally, results for the ESPEs are presented in Fig. 4.2.

Table 4.2: Calculated ESPEs for the SDPF-NR effective interactions and the proton gap between $1d_{3/2}$ and $2s_{1/2}$ orbitals.

N	isotope	spin	BE (MeV)	ESPE (MeV)	$1d_{3/2}-2s_{1/2}$ (MeV)
20	^{40}Ca	0	-280.35		
	^{39}K	1/2	-261.96	-18.40	
	^{39}K	3/2	-264.71	-15.64	2.75
	^{39}K	5/2	-257.32	-23.04	
28	^{48}Ca	0	-347.61		
	^{47}K	1/2	-324.40	-23.21	
	^{47}K	3/2	-324.00	-23.61	-0.40
	^{47}K	5/2	-318.08	-29.53	
32	^{52}Ca	0	-366.93		
	^{51}K	1/2	-340.93	-26.00	
	^{51}K	3/2	-340.76	-26.17	-0.17
	^{51}K	5/2	-334.61	-32.32	

Table 4.3: Calculated ESPEs for the SDPF-U effective interactions and the proton gap between $1d_{3/2}$ and $2s_{1/2}$ orbitals.

N	isotope	spin	BE (MeV)	ESPE (MeV)	$1d_{3/2}-2s_{1/2}$ (MeV)
20	^{40}Ca	0	-278.73		
	^{39}K	1/2	-260.32	-18.41	
	^{39}K	3/2	-263.11	-15.62	2.79
	^{39}K	5/2	-255.93	-22.80	
28	^{48}Ca	0	-350.12		
	^{47}K	1/2	-326.67	-23.45	
	^{47}K	3/2	-326.30	-23.82	-0.37
	^{47}K	5/2	-321.45	-28.67	
32	^{52}Ca	0	-370.88		
	^{51}K	1/2	-344.42	-26.47	
	^{51}K	3/2	-344.94	-25.94	0.52
	^{51}K	5/2	-340.36	-30.52	

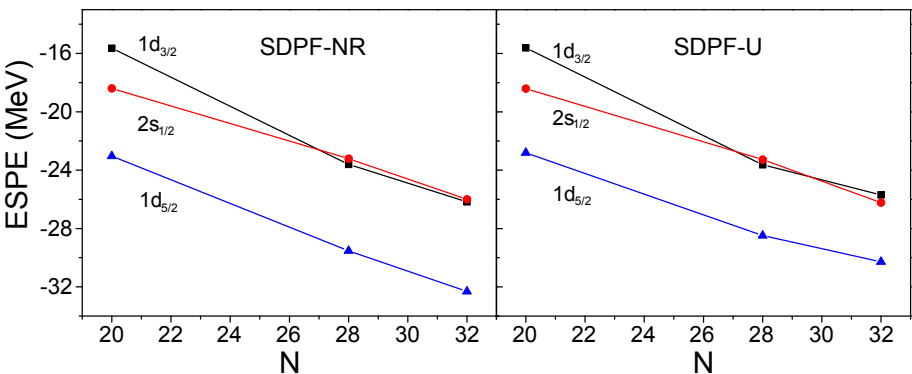


Figure 4.2: Proton effective single-particle energies (ESPEs) calculated for potassium isotopes. The Calculations were performed with two effective interactions: SDPF-NR (left panel) and SDPF-U (right panel). A significant difference is observed beyond $N = 28$ where for the SDPF-NR interaction the $1d_{3/2}$ orbit is located a bit below the $2s_{1/2}$ and they are almost degenerate, while SDPF-U predicts a crossing point around $N = 30$ and well separated orbits by about 500 keV.

The behavior of the ESPEs for both interactions is the same for isotopes with $20 \leq N \leq 28$, while filling the $\nu 1f_{7/2}$. Both interactions predicted the crossing point of the $\pi 1d_{3/2}$ and $\pi 2s_{1/2}$ around $N = 27$ with the total change of the gap of around -3.15 MeV. However, a large discrepancy is found for isotopes

with $29 \leq N \leq 32$, when the next orbit ($\nu 2p_{3/2}$) is involved. In the case of the SDPF-NR interaction, the $\pi 2s_{1/2}$ orbit stays above the $\pi 1d_{3/2}$ with a reduction of the gap by 0.23 MeV. On the other hand, calculations with SDPF-U interaction show that the ESPEs return to normal order at $N = 29$ where the $\pi 2s_{1/2}$ lies below the $\pi 1d_{3/2}$. The total change between these two orbits from $N = 28$ up to $N = 32$ is found to be 0.89 MeV. A more detailed investigation of the evolution of the ESPEs is presented in Article II (section 4.4), where it is discussed which part of the monopole residual interaction is responsible for this effect.

4.2.1 Spin-tensor decomposition

It was shown in the previous subsection that the monopole term of the NN interaction is responsible for the shell evolution. In order to investigate this effect in more details, the different terms of the NN interaction will be discussed.

Based on the information obtained from various experiments, the NN interaction should have the following properties: attractive and short range ($\sim 10^{-15}$ m), it is isospin symmetric and spin dependent, its non-central component should be included and the interaction conserves parity. Thus, the NN interaction can be expressed as a sum of three components:

$$V(1, 2) = V_C(1, 2) + V_{LS}(1, 2) + V_T(1, 2) \quad (4.9)$$

where V_C is a central interaction, V_{LS} is the spin-orbit interaction and V_T represents a tensor interaction. Furthermore, every term now can be presented as function of spin ($\vec{\sigma}$), isospin ($\vec{\tau}$) and position coordinate (\vec{r}) variables, where $\vec{r} = \vec{r}_1 - \vec{r}_2$ is the relative distance between two interacting nucleons. Applying this, one has to obey certain symmetries such as time-reversal, parity and isobaric. Keeping in mind that the interaction is scalar, the different components are rewritten as [4]

- a scalar type central interaction

$$V_C(1, 2) = V_0(r) + V_\sigma(\vec{\sigma}_1 \cdot \vec{\sigma}_2) + V_\tau(r)(\vec{\tau}_1 \cdot \vec{\tau}_2) + V_{\sigma\tau}(r)(\vec{\sigma}_1 \cdot \vec{\sigma}_2)(\vec{\tau}_1 \cdot \vec{\tau}_2) \quad (4.10)$$

This term is called central because it depends on the amplitude of \vec{r} , but not its direction.

- a vector type spin-orbit interaction

$$V_{LS}(1, 2) = V_{LS}(r)\vec{L} \cdot \vec{S} \quad (4.11)$$

where $\vec{S} = (\vec{\sigma}_1 + \vec{\sigma}_2)/(2)$ and $\vec{L} = \vec{r} \times \vec{p}$. Due to its momentum dependence, it has a non-local character.

- tensor type tensor interaction

$$V_T(1, 2) = (V_{T_0}(r) + V_{T_\tau}(r)\vec{\tau}_1 \cdot \vec{\tau}_2) \left(\frac{(\vec{\sigma}_1 \cdot \vec{r})(\vec{\sigma}_2 \cdot \vec{r})}{r^2} - \frac{1}{3}\vec{\sigma}_1 \cdot \vec{\sigma}_2 \right) \quad (4.12)$$

The tensor component was introduced based on the observation that the deuterium nucleus ($\pi + \nu$; $L = 0$ and $S = 1$) has a non-zero quadrupole moment. This pointed to the mixing with $L = 2$ and $S = 1$ configuration and the fact that there should be a term in the NN interaction which depends on the relative orientation between \vec{r} and spin \vec{s} , meaning it is a non-central force with a local character.

In what follows, only the monopole part of the NN interaction will be considered. In order to separate these three components of the monopole term, a method called spin-tensor decomposition [88, 89, 90, 91, 92, 93] can be used. Here only the main ideas of the method will be outlined. The following procedure [90] yields the matrix elements of different $V_{(i)}$ components where i stands for C , LS or T :

- Transformation of the TBMEs from jj -coupling to LS -coupling
- From the LS -coupled matrix elements of $V(1, 2)$, the LS -coupled TBMEs of each component $V_{(i)}$ are calculated
- the LS -coupled matrix elements of each component $V_{(i)}$ are transformed to jj -coupling matrix elements
- These matrix elements are used for further investigation including the creation of the Hamiltonian, diagonalization, obtaining eigenvalues, etc.

It is important to note that the limiting factor of this method is that the model space in the calculations has to include all spin-orbit partners ($j = l \pm \frac{1}{2}$) within a given oscillator shell, thus its application is reduced only to isotopes below Ni ($Z = 28$) with neutrons well below $N = 40$.

In what follows, the main characteristics of the components of the NN interaction will be presented. The central component depends on the relative distance between two interacting nucleons and it is stronger between orbitals with the same nodal quantum number n , $\Delta n = 0$. This is schematically presented in Fig. 4.3.

In case of the tensor component, the character of the considered orbits ($j = l \pm s$) plays a decisive role on the sign of the interaction. Labeling the proton orbits by $j_> = l + \frac{1}{2}$ and $j_< = l - \frac{1}{2}$, while the neutron orbits are marked as $j'_> = l' + \frac{1}{2}$ and $j'_< = l' - \frac{1}{2}$, an attractive interaction is expected between the orbits with

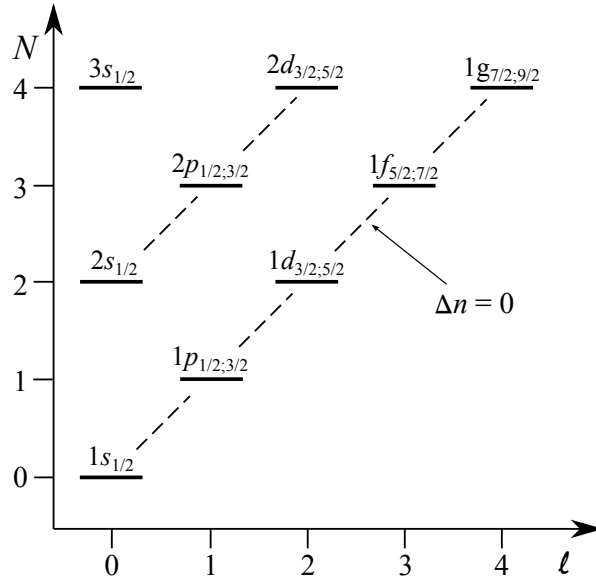


Figure 4.3: Representation of the orbitals (nl_j) where the diagonal dashed line represents $\Delta n = 0$ line. The strength of the central and tensor interaction is decreasing for increasing Δn and Δl .

opposite character ($j_< - j'_>$ or vice versa) and repulsive interaction between the orbit with the same character ($j_> - j'_>$ or $j_< - j'_<$). This is depicted in Fig 4.4.

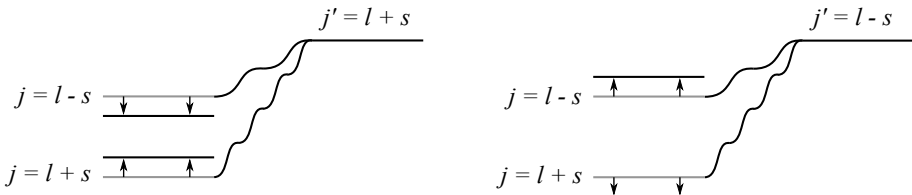


Figure 4.4: Schematic representation of the tensor interaction. It is attractive between the orbits with the opposite orientation of the intrinsic spin relative to the angular momentum and repulsive between the orbits with the same intrinsic spin orientation.

In addition to that, the interaction is the strongest for $\Delta l = 0$ and $\Delta n = 0$ where the maximal overlap of the radial wave-functions of these two orbits is obtained [94]. Furthermore, for the tensor interaction the following identity can

be derived from angular momenta algebra [94]:

$$(2j_> + 1)V_{j>,j';\text{tensor}}^T + (2j_< + 1)V_{j<,j';\text{tensor}}^T = 0 \quad (4.13)$$

where $T = 0, 1$ is the isospin, and $j_<, j_>$ are the spin-orbit partners. For Eq. (4.13) one can conclude that the total effect of the tensor interaction will vanish for the fully occupied $j_<, j_>$ orbits. Lack of information about the vector term in literature shows that this term is the least understood.

In the case of potassium isotopes, the phenomenological interactions SDPF-NR and SDPF-U were decomposed in order to provide more information about the evolution of the $\pi 1d_{3/2}$ and $\pi 2s_{1/2}$ orbits. The results are presented in Table IV in Article II (section 4.4). As an example, an intuitive analysis based on the characteristics of the tensor interaction is given here:

$$\begin{array}{lcl} |V_{d_{3/2}f_{7/2}}^{\pi\nu}|_{\text{tensor}} & > & |V_{d_{3/2}p_{3/2}}^{\pi\nu}|_{\text{tensor}} \\ \Delta n = 0 & & \Delta n = 1 \\ \Delta l = 1 & & \Delta l = 1 \\ |-0.28| & > & |-0.08| \end{array} \quad (4.14)$$

The tensor interaction is attractive (negative values) caused by the character of the orbitals as the $\pi d_{3/2}$ is $j = l - s$ interacting with the $\nu f_{7/2}$ or $\nu p_{3/2}$ which are $j = l + s$ orbits. It should be noted that the tensor interaction vanishes when the $s_{1/2}$ orbit is involved, due to the fact that it depends on the relative orientation of the intrinsic spin and the angular momentum of the interacting nucleons which is not defined for the $l = 0$ case.

In order to investigate the evolution of the gap, one has to look into the difference of the centroids labeled as ΔV . The results of the calculations performed for the $\pi(d_{3/2}-s_{1/2})$ gap in potassium are presented in Table V in Article II (section 4.4). Based on these calculations, we were able to conclude that although the change in the size of the gap is a result of the combined effect of all terms of the interaction, the central component dominates.

In the next sections, the discussion of the experimental results, in particular nuclear spins and magnetic moments, will be presented in the form of two published articles. The first article discusses the evolution of the $\pi 2s_{1/2}$ and $\pi 1d_{3/2}$ orbits based on the established ground-state nuclear spin of $^{49,51}\text{K}$. The second article is a continuation of the first one, where the nuclear structure of the entire isotopic chain of potassium is discussed.

4.3 Article I

The first article, published in the Physics Review Letters, focuses on experimental model independent spin determination of the ^{49}K and ^{51}K ground states, and related to that the evolution of the $\pi(2s_{1/2}-1d_{3/2})$ gap. The ground state spin of ^{49}K is found to be $1/2$, while that of ^{51}K is $3/2$. This points to a reinversion of the proton single-particle levels in the isotopic chain, which was observed for the first time.

My main contribution to this paper was in the performed analysis and shell-model calculations for the two interactions (SDPF-NR and SDPF-U). I was in charge of drafting the article and preparing it for submission.

Physical Review Letters 110, 172505 (2013)

**Spins and Magnetic Moments of ^{49}K and ^{51}K : establishing the
 $1/2^+$ and $3/2^+$ level ordering beyond $N = 28$**

J. Papuga,^{1,*} M. L. Bissell,¹ K. Kreim,² K. Blaum,² B.A. Brown,³ M. De Rydt,¹ R. F. Garcia Ruiz,¹ H. Heylen,¹ M. Kowalska,⁴ R. Neugart,⁵ G. Neyens,¹ W. Nörtershäuser,^{5,6} T. Otsuka,⁷ M. M. Rajabali,¹ R. Sánchez,⁸ Y. Utsuno,⁹ and D. T. Yordanov²

¹*Instituut voor Kern- en Stralingsfysica,
KU Leuven, B-3001 Leuven, Belgium*

²*Max-Plank-Institut für Kernphysik, D-69117 Heidelberg, Germany*

³*Department of Physics and Astronomy and National Superconducting Cyclotron Laboratory,
Michigan State University, East Lansing, Michigan 48824, USA*

⁴*Physics Department, CERN, CH-1211 Geneva 23, Switzerland*

⁵*Institut für Kernchemie, Universität Mainz, D-55128 Mainz, Germany*

⁶*Institut für Kernphysik, TU Darmstadt, D-64289 Darmstadt, Germany*

⁷*Department of Physics and Center for Nuclear Study,
University of Tokyo, Hongo, Tokyo 113-0033, Japan and RIKEN,
Hirosawa, Wako-shi, Saitama 351-0198, Japan*

⁸*GSI Helmholtzzentrum für Schwerionenforschung, D-64291 Darmstadt, Germany*
⁹*Japan Atomic Energy Agency, Tokai-mura, Ibaraki 319-1195, Japan*

(Dated: February 8, 2015)

Abstract

The ground-state spins and magnetic moments of $^{49,51}\text{K}$ have been measured using bunched-beam high-resolution collinear laser spectroscopy at ISOLDE-CERN. For ^{49}K a ground-state spin $I = 1/2$ was firmly established. The observed hyperfine structure of ^{51}K requires a spin $I > 1/2$ and strongly suggests $I = 3/2$. From its magnetic moment $\mu(^{51}\text{K}) = +0.5129(22) \mu_N$ a spin-parity $I^\pi = 3/2^+$ with a dominant $\pi 1d_{3/2}^{-1}$ hole configuration was deduced. This establishes for the first time the re-inversion of the single-particle levels and illustrates the prominent role of the residual monopole interaction for single-particle levels and shell evolution.

The nuclear shell-model forms the basis for our understanding of atomic nuclei and since the very beginning spins and magnetic moments of ground states have played a crucial role [1, 2]. Single-particle as well as collective degrees of freedom in atomic nuclei can be described with modern large-scale shell-models [3]. However, the interplay between theory and experiment is indispensable for further improving the shell-model effective interactions as new regions of the nuclear chart are being explored.

Since more and more rare-isotope beams became available, strong modifications to the well-known shell structure were required in several regions of the nuclear chart. Examples are the unexpected level ordering in the "island of inversion" isotopes $^{31,33}\text{Mg}$ [4], the weakening of the $N = 28$ shell gap below Ca [5], the monopole migration of proton single-particle levels towards $N = 28$ [6] and $N = 50$ [7]. The origin of the changes in shell structure has been discussed in several theoretical papers [8–12]. As experimental evidence is growing, effective shell-model interactions as well as mean-field models are being modified to account for the new observations [13–17].

In the region below Ca ($Z = 20$), where protons occupy the sd shell and neutrons occupy the pf shell, the gradual filling of the $\nu 1f_{7/2}$ orbit from $N = 20$ to $N = 28$ leads to a strong decrease of the first excited $1/2^+$ energy in the ^{19}K and ^{17}Cl isotopes. This level becomes the ground state in ^{47}K [18] and in the Cl chain the inversion begins at ^{41}Cl [19]. Following the explanation given by Otsuka *et al.* [9], occupation of the $\nu 1f_{7/2}$ orbit (having $j = l + 1/2$) leads to an increased binding of the $\pi 1d_{3/2}$ orbital (with $j' = l' - 1/2$), and thus to a near-degeneracy (even inversion) with the $\pi 2s_{1/2}$ orbit as the $\nu 1f_{7/2}$ orbit is fully occupied at $N = 28$.

This raises the question of what happens beyond $N = 28$, when the higher pf orbits are being filled. Using a Woods-Saxon potential e.g. the monotonic lowering of the $\pi 1d_{3/2}$ energy with respect to the $\pi 2s_{1/2}$ energy is predicted to continue well beyond $N = 28$. However, it is by now also well-known that the residual monopole interaction, which changes with isospin and thus with neutron number, plays an important role in the evolution of single-particle levels. This residual monopole interaction has a central, spin-orbit and tensor term, all of which need to be determined from experimental data. Furthermore, these monopole interactions are strongest between orbits with the same number of nodes, and thus in the region beyond $N = 28$ it is the $\pi 2s_{1/2} - \nu 2p_{3/2}$ interaction strength that is the dominant one [12]. Until now, very little experimental data are available which probe this part of the

nucleon-nucleon residual interaction. A rather extended level scheme is available for ^{49}K [20] but all spins are tentative as long as the ground-state spin is not established. These recent in-beam data favor a ground-state spin $I = 1/2$ while earlier β -decay work suggests $I = 3/2$ [21]. For ^{51}K no excited states are known. From β -decay studies the ground-state spin is tentatively assigned to be $I = 3/2$ with a dominant $\pi 1d_{3/2}$ hole structure [22].

This letter presents the measured ground-state spins and magnetic moments of $^{49,51}\text{K}$ with two and four neutrons beyond $N = 28$ respectively, thus gradually filling the $\nu 2p_{3/2}$ orbit. The K^+ beams were produced at the ISOLDE facility at CERN where 1.4 GeV protons impinged on a thick UC_x target. Atoms diffused out of the target and were surface ionized in a heated tube at ~ 2000 °C. The ions were accelerated up to 40 kV, mass separated and bunched by the gas-filled Paul trap (ISCOOL) [7, 23]. Collinear laser spectroscopy [24] was performed using the 769.9 nm $4s\ ^2S_{1/2} \rightarrow 4p\ ^2P_{1/2}$ atomic transition in K, after the beam was neutralized via collisions with neutral K atoms in a charge exchange cell (CEC). To scan the hyperfine structure the Doppler-shifted laser frequency, as experienced by the fast atoms, was modified by applying a tunable scanning voltage of ± 500 V on the CEC. The fluorescence light emitted from the resonantly laser-excited atoms was subsequently detected using photomultiplier tubes (PMTs). By gating the PMT signals such that photons were only collected during the $\sim 6\ \mu\text{s}$ period when the bunch of atoms pass in front of the PMT, the background photon count rate was reduced by a factor of 15000 (= ISCOOL accumulation time/ion bunch temporal width) compared to a continuous beam detection.

The relatively slow decay rate of the atomic transition ($3.8 \times 10^7\ \text{s}^{-1}$), low quantum efficiency (2.5%) and high heat-related dark counts of PMTs operating at these wavelengths hinder optical spectroscopy of exotic K isotopes. In order to perform the measurements on a ^{51}K beam of ~ 4000 ions/s, a new optical detection station was developed. Details on this will be presented in a forthcoming paper [25].

Typical hyperfine structure (hfs) spectra for ^{49}K and ^{51}K are shown in Fig. 1. To convert the recorded scanning voltage into frequency, AME 2012 [26] masses were used with the recently measured masses of ^{49}K [27] and ^{51}K [28] already included. The hfs spectra have been fitted using the χ^2 minimization procedure MINUIT. The peak positions were determined by the hyperfine parameters $A(^2S_{1/2})$ and $A(^2P_{1/2})$, the nuclear spin I and the center of gravity of the structure defining the isotope shift. The A -parameters (Table I) are directly related to the nuclear magnetic moment through the relation $A = \mu B_0/IJ$, where B_0 is the

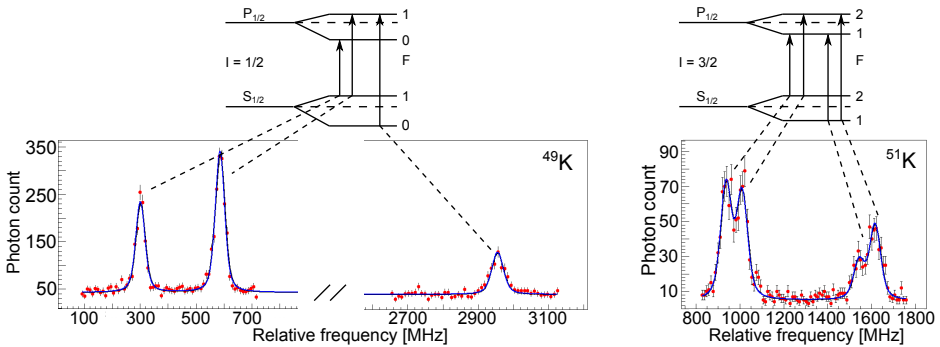


FIG. 1: (Color online) Typical hyperfine spectra for ^{49}K and ^{51}K . Spectra are shown relative to the centroid of ^{39}K .

magnetic field generated by electrons at the site of a nucleus. Voigt profiles with common line widths have been used for all peaks in the spectrum. The nuclear spin determines the number of allowed transitions. For $I = 1/2$ only three transitions are allowed (left-hand side of Fig. 1) and the ground-state spin of ^{49}K can be determined as $I = 1/2$. For all other spins four resonances appear in the spectrum, as illustrated in the right part of Fig. 1. We have therefore fitted the ^{51}K spectra assuming a spin $3/2$, $5/2$ and $7/2$. In the case of a $J = 1/2$ to $J = 1/2$ transition the ratio of the upper-to-lower hyperfine parameter cannot be used to exclude a particular spin (method used e.g. to assign the $^{72,74}\text{Cu}$ spins [29]), as the *relative* hyperfine structure separations are unaffected by the nuclear spin in this case. There is, however, an indirect way to determine the ^{51}K spin, namely by comparing the intensities of the different hyperfine structure components. From the intensity ratios observed for ^{51}K we can exclude a spin $5/2$ (or even higher) at a confidence level of 95%. To further confirm the measured spin $I = 3/2$, the extracted magnetic moment for different spin assumptions can be compared to single-particle moments and predictions by shell-model calculations.

The magnetic moments are deduced from the $A(^2S_{1/2})$ values relative to that of ^{39}K , for which a very precise measurement of $A_{\text{ref}}(^2S_{1/2}) = 230.8598601(7)$ MHz and $\mu_{\text{ref}} = +0.3914662(3) \mu_N$ is available from an atomic beam magnetic resonance measurement [30]. The results are presented in Table II. The statistical errors are smaller than the hyperfine anomalies measured for $^{40,41,42}\text{K}$ relative to ^{39}K [30–32]. Following the approach of Bohr [33] these hyperfine anomalies are well reproduced and those for $^{47,49,51}\text{K}$ are predicted to be

TABLE I: Fitted hyperfine parameters for the studied isotopes (assuming different spins for ^{51}K).

Isotope	I	$A(^2S_{1/2})$ (MHz)	$A(^2P_{1/2})$ (MHz)
^{39}K	3/2	+231.0 (3)	+27.8 (2)
^{47}K	1/2	+3413.2 (2)	+411.8 (2)
^{49}K	1/2	+2368.2 (14)	+285.6 (7)
^{51}K	3/2	+302.5 (13)	+36.6 (9)
^{51}K	(5/2)	+201.6 (9)	+24.4 (6)
^{51}K	(7/2)	+151.3 (7)	+18.3 (4)

less than 0.3%. This is included as an additional error on the magnetic moments (in square brackets).

The ground-state wave function of the odd- A potassium isotopes is dominated by one proton hole in the $Z = 20$ shell. The Schmidt moments and thus also the free-nucleon g factors of the relevant single-particle orbits $\pi 1d_{3/2}$, $\pi 2s_{1/2}$ and $\pi 1f_{7/2}$ are very different from each other (respectively +0.08, +5.58 and +1.65). Therefore their g factors are an excellent probe to monitor in which orbital the unpaired proton occurs. Because the single nucleon does not appear as a free particle, the experimental values are compared to effective single-nucleon g factors, with typical values for the sd shell [34]. The upper part of Fig. 2 illustrates that the experimental g factors of $^{39-45}\text{K}$ are all close to the effective value for a hole in the $\pi 1d_{3/2}$ orbit ($g_{\text{eff}} = +0.25$). Also the ^{51}K g factors (assuming different spins, given in column 3 of Table II) agree very well with this value. This confirms the dominant $\pi 1d_{3/2}^{-1}$ component in the ground-state wave function of each of these isotopes, including ^{51}K . The ground-state spins are known to be 3/2 $^+$ up to ^{45}K and this supports again our results of the 3/2 for the ^{51}K ground state. The ^{47}K g factor is close to the effective single-particle value for a $\pi 2s_{1/2}^{-1}$ hole configuration and its spin-parity is known to be 1/2 $^+$ [18]. The ground-state spin of ^{49}K is established to be also $I = 1/2$, but its g factor suggests a rather mixed wave function.

In what follows we focus on further establishing the ground-state spin of ^{51}K . For this we compare the experimental magnetic moments to values calculated with different effective shell-model interactions. Calculations have been performed with the SDPF-NR [35, 36] and its recently upgraded SDPF-U interaction [14] as well as with the recently developed SDPF-

TABLE II: Experimental magnetic moments (in units of μ_N) and g factors, compared to shell-model values using different effective interactions (see text for details). The error in square brackets represents the uncertainty related to the hyperfine anomaly. The ^{47}K value is in good agreement with the literature value $1.933(9) \mu_N$ [18]. Energies for the predicted states of ^{51}K are shown in keV.

Isotope	I^π	g_{exp}	μ_{exp}	$\mu_{\text{SDPF-NR}}$	$\mu_{\text{SDPF-U}}$	$\mu_{\text{SDPF-MU}}$
^{39}K	$3/2^+$	+0.2611 (3) [8]	+0.3917 (5) [12]	+0.63	+0.63	+0.65
^{47}K	$1/2^+$	+3.8584 (2) [116]	+1.9292 (1) [58]	+1.87	+1.91	+1.91
^{49}K	$1/2^+$	+2.6772 (16) [80]	+1.3386 (8) [40]	+1.61	+1.81	+1.72
^{51}K	$3/2^+$	+0.3420 (15) [10]	+0.5129 (22) [15]	+0.60 ($E = 0$)	+0.63 ($E = 0$)	+0.51 ($E = 0$)
^{51}K	$(5/2^+)$	+0.2279 (10) [7]	+0.5698 (25) [17]	+0.84 ($E = 1725$)	+1.40 ($E = 2018$)	+0.75 ($E = 2264$)
^{51}K	$(7/2^+)$	+0.1710 (8) [5]	+0.5986 (28) [18]	-0.13 ($E = 1793$)	-0.04 ($E = 2040$)	-0.10 ($E = 2048$)

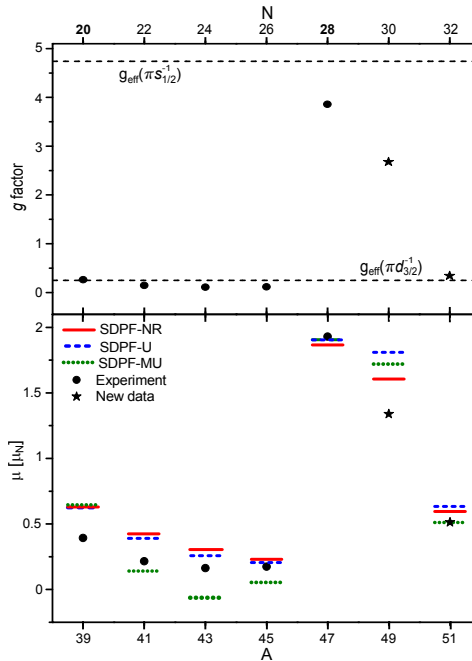


FIG. 2: (Color online) Experimental g factors (upper) and magnetic moments (lower) from [18, 30] (dots) and the new data (stars) for ^{49}K ($1/2$) and ^{51}K ($3/2$). Effective single-particle g factors are calculated with $g_s^{\text{eff}}=0.85g_s^{\text{free}}$ and $g_l^{\pi}=1.15$, $g_l^{\nu}=-0.15$. See text for details on calculations.

MU interaction [37] (Table II). The SDPF-NR and SDPF-U interactions have monopole matrix elements that were tuned by fitting experimental spectra of isotopes in this region, from O to Ca. The SPDF-MU interaction is based on the recently developed monopole-based universal interaction V_{MU} [12] and involves therefore fewer fitted parameters. Calculations are performed with protons restricted to the sd shell (thus only positive parity levels are calculated) and neutrons in the full pf shell. The experimental magnetic moments for the $3/2^+$ ground states of $^{39-45}\text{K}$ are well reproduced by all effective interactions (lower part of Fig. 2), and the agreement for the $3/2^+$ state in ^{51}K is even better than $0.1 \mu_N$ for all of them. The lowest positive parity states ($5/2^+$, $7/2^+$) appear around 2 MeV and have magnetic moments that deviate significantly more from the experimental values (Table II). Negative parity $3/2^-$, $5/2^-$, $7/2^-$ states, due to a proton excited in the pf shell, all have a magnetic moment that is larger than $+3.3 \mu_N$, incompatible with the observed small

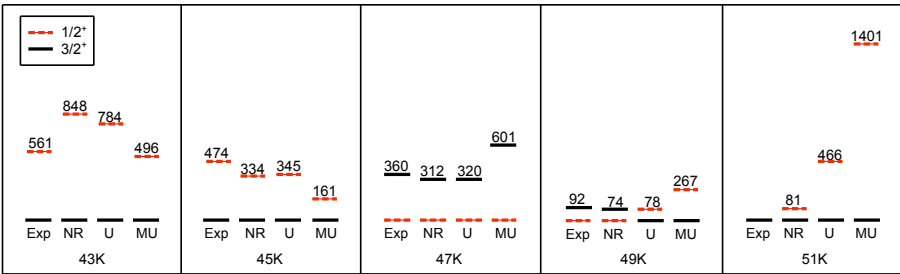


FIG. 3: (Color online) Experimental energies in odd-K isotopes [20, 22, 39–41] compared with calculated levels (SDPF-NR, SDPF-U and SDPF-MU interactions; details in text). $3/2^+$ levels are solid black lines and $1/2^+$ dashed red. Ground-state spins for ^{49}K and ^{51}K are from this work.

value around $+0.5\mu_N$. All arguments together consistently confirm that the ground-state spin-parity of ^{51}K is $3/2^+$. The magnetic moment of the $1/2^+$ ground state in ^{47}K is also reproduced very well, while the experimental moment of the $I = 1/2^+$ ground state of ^{49}K is somewhat overestimated by all calculations, suggesting that some particular mixing in the wave function is not well taken into account. A simple two-level mixing calculation shows that 25% mixing of a $[\pi d_{3/2}^{-1}(\nu fp)_{2+}]_{1/2^+}$ allows to reproduce the observed $1/2^+$ moment [38].

By establishing the ground-state spins of ^{49}K and ^{51}K , we have demonstrated that the gradual reduction of the energy gap between the proton $\pi 2s_{1/2} - \pi 1d_{3/2}$ orbits reaches a minimum around $N = 29$ and again increases towards the more neutron rich isotopes. It is the first time that such a 're-inversion' of single-particle levels is observed and it illustrates how the residual monopole interaction dominates their evolution.

In Fig. 3 we compare the experimental $3/2^+$ and $1/2^+$ levels to those calculated with the different shell-model effective interactions. The SDPF-NR and SDPF-U interactions show the best overall agreement, which is not surprising because their monopole matrix elements were tuned by fitting to experimental spectra, including that of ^{47}K [14]. With the recently developed SDPF-MU interaction [37] a reasonable agreement with the data is found, considering that its cross-shell interaction is described in a functional form using the simple tensor-subtracted monopole evolution as described in [12], with only six parameters.

In conclusion, the hyperfine structures of atomic $^{49,51}\text{K}$ isotopes were measured for the first time. The data establish a ground-state spin $I = 1/2$ for ^{49}K and $I = 3/2$ for ^{51}K . The magnetic moments $\mu(^{49}\text{K}) = +1.3386(8)[40]\mu_N$ and $\mu(^{51}\text{K}) = +0.5129(22)[15]\mu_N$ reveal a

mixed configuration for ^{49}K and a rather pure $\pi 1d_{3/2}^{-1}$ configuration for ^{51}K . Comparison with shell-model calculations shows good agreement for ^{51}K , but none of the interactions reproduces the low experimental value of ^{49}K . Best overall agreement with the ground-state moment and energy levels in ^{49}K is observed for the SDPF-NR interaction, which predicts the highest mixing with $\pi 1d_{3/2}$ components in its wave function. The experimentally observed evolution of the $1/2^+$ and $3/2^+$ levels is now established up to ^{51}K . Different effective interactions predict very different energy gaps between the $3/2^+$ and the first excited $1/2^+$ level in ^{51}K . Along with the current results, spectroscopy of the excited states in ^{51}K is required to further improve the effective interactions in this region.

This work was supported by the IAP-project P6/23, the FWO-Vlaanderen, NSF grant PHY-1068217, BMBF (05 P12 RDCIC), Max-Planck Society and EU FP7 via ENSAR (no. 262010). We would like to thank to the ISOLDE technical group for their support and assistance.

* jasna.papuga@fys.kuleuven.be

- [1] M. G. Mayer, Phys. Rev. **74**, 235 (1948).
- [2] M. G. Mayer, Phys. Rev. **75**, 1969 (1949).
- [3] E. Caurier, G. Martínez-Pinedo, F. Nowacki, A. Poves, and A. P. Zuker, Rev. Mod. Phys. **77**, 427 (2005).
- [4] G. Neyens, Phys. Rev. C **84**, 064310 (2011).
- [5] B. Bastin et al., Phys. Rev. Lett. **99**, 022503 (2007).
- [6] A. Gade et al., Phys. Rev. C **74**, 034322 (2006).
- [7] K. T. Flanagan et al., Phys. Rev. Lett. **103**, 142501 (2009).
- [8] T. Otsuka et al., Phys. Rev. Lett. **87**, 082502 (2001).
- [9] T. Otsuka, T. Suzuki, R. Fujimoto, H. Grawe, and Y. Akaishi, Phys. Rev. Lett. **95**, 232502 (2005).
- [10] T. Otsuka, T. Matsuo, and D. Abe, Phys. Rev. Lett. **97**, 162501 (2006).
- [11] N. A. Smirnova, B. Bally, K. Heyde, F. Nowacki, and K. Sieja, Phys. Lett. B **686**, 109 (2010).
- [12] T. Otsuka et al., Phys. Rev. Lett. **104**, 012501 (2010).
- [13] M. Grasso et al., Phys. Rev. C **76**, 044319 (2007).

- [14] F. Nowacki and A. Poves, Phys. Rev. C **79**, 014310 (2009), URL <http://link.aps.org/doi/10.1103/PhysRevC.79.014310>.
- [15] M. Zalewski et al., Phys. Rev. C **80**, 064307 (2009).
- [16] K. Kaneko, Y. Sun, T. Mizusaki, and M. Hasegawa, Phys. Rev. C **83**, 014320 (2011).
- [17] Y.Z.Wang, J.Z.Gu, X.Z.Zhang, and J.M.Dong, Phys. Rev. C **84**, 044333 (2011).
- [18] F. Touchard et al., Phys. Lett. B **108**, 169 (1982).
- [19] J. Ollier et al., Phys. Rev. C **67**, 024302 (2003).
- [20] R. Broda et al., Phys. Rev. C **82**, 034319 (2010), URL <http://link.aps.org/doi/10.1103/PhysRevC.82.034319>.
- [21] L. C. Carraz et al., Physics Letters B **109**, 419 (1982), ISSN 0370-2693, URL <http://www.sciencedirect.com/science/article/pii/0370269382911042>.
- [22] F. Perrot et al., Phys. Rev. C **74**, 014313 (2006).
- [23] H. Franberg et al., Nucl. Inst. and Meth. in Phys. Res. B **266**, 4502 (2008).
- [24] A. C. Mueller et al., Nucl. Phys. A **403**, 234 (1983).
- [25] K. Kreim et al., in preparation.
- [26] M. Wang et al., Chinese Physics C **36**, 16032014 (2012).
- [27] A. Lapierre et al., Phys. Rev. C **85**, 024317 (2012), URL <http://link.aps.org/doi/10.1103/PhysRevC.85.024317>.
- [28] A. T. Gallant et al., Phys. Rev. Lett. **109**, 032506 (2012), URL <http://link.aps.org/doi/10.1103/PhysRevLett.109.032506>.
- [29] K. T. Flanagan et al., Phys. Rev. C **82**, 041302(R) (2010).
- [30] A. Beckmann, K. D. Böklen, and D. Elke, Zeitschrift für Physik A Hadrons and Nuclei **270**, 173 (1974), ISSN 0939-7922, URL <http://dx.doi.org/10.1007/BF01680407>.
- [31] J. T. Eisinger, B. Bederson, and B. T. Feld, Phys. Rev. **86**, 73 (1952).
- [32] Y. W. Chan, V. W. Cohen, and H. B. Silsbee, Phys. Rev. **184**, 1102 (1969).
- [33] A. Bohr, Phys. Rev. **81**, 331 (1951).
- [34] W. A. Richter, S. Mkhize, and B. A. Brown, Phys. Rev. C **78**, 064302 (2008).
- [35] J. Retamosa, E. Caurier, F. Nowacki, and A. Poves, Phys. Rev. C **55**, 1266 (1997).
- [36] S. Nummela et al., Phys. Rev. C **64**, 054313 (2001).
- [37] Y. Utsuno et al., Phys. Rev. C **86**, 051301(R) (2012).
- [38] G. Neyens, proc. Int. Sym. "Exotic Nuclear Structure From Nucleons" (ENSFN 2012), Tokyo,

- Japan, Oct.2012 to be published in Journal of Physics: Conference Series (2013).
- [39] D. F. Measday and T. J. Stocki, Phys. Rev. C **73**, 045501 (2006).
 - [40] A. Huck et al., Phys. Rev. C **21**, 712 (1980).
 - [41] L. Weissman et al., Phys. Rev. C **70**, 024304 (2004).

4.4 Article II

This article represents an overview of the nuclear structure of all K isotopes for which magnetic moments are known. The discussion is based on the measured nuclear spins and the comparison of the magnetic moments with the shell-model calculations. The odd- A and even- A isotopes are discussed in separate sections, with common summary and conclusions.

This article has been entirely written by me, including the analysis and the shell-model calculations of the nuclear moments. I was in charge of preparing the paper for the submission process, and made all the contacts with the different collaborators.

Physical Review C 90, 034321 (2014)

Shell structure of potassium isotopes deduced from their magnetic moments

J. Papuga,^{1,*} M. L. Bissell,¹ K. Kreim,² C. Barbieri,³ K. Blaum,² M. De Rydt,¹ T. Duguet,^{4,5} R. F. Garcia Ruiz,¹ H. Heylen,¹ M. Kowalska,⁶ R. Neugart,⁷ G. Neyens,¹ W. Nörtershäuser,^{7,8} M. M. Rajabali,¹ R. Sánchez,^{9,10} N. Smirnova,¹¹ V. Somà,⁴ and D. T. Yordanov^{2,12}

¹*KU Leuven, Instituut voor Kern- en Stralingsphysica, 3001 Leuven, Belgium*

²*Max-Plank-Institut für Kernphysik, D-69117 Heidelberg, Germany*

³*Department of Physics, University of Surrey,
Guildford GU2 7XH, United Kingdom*

⁴*CEA-Saclay, IRFU/Service de Physique Nucléaire, 91191 Gif-sur-Yvette, France*

⁵*National Superconducting Cyclotron Laboratory and Department of Physics and Astronomy,
Michigan State University, East Lansing, Michigan 48824, USA*

⁶*Physics Department, CERN, CH-1211 Geneva 23, Switzerland*

⁷*Institut für Kernchemie, Universität Mainz, D-55128 Mainz, Germany*

⁸*Institut für Kernphysik, TU Darmstadt, D-64289 Darmstadt, Germany*

⁹*GSI Helmholtzzentrum für Schwerionenforschung, D-64291 Darmstadt, Germany*

¹⁰*Helmholtz Institut Mainz, Johannes Gutenberg Universität Mainz 55099 Mainz, Germany*

¹¹*CENBG (CNRS/IN2P3-Université Bordeaux 1)*

Chemin du Solarium, BP 120, 33175 Gradignan, France

¹²*Institut de Physique Nucléaire Orsay,*

IN2P3/CNRS, 91405 Orsay Cedex, France

(Dated: March 13, 2015)

Abstract

Background Ground-state spins and magnetic moments are sensitive to the nuclear wave function, thus they are powerful probes to study the nuclear structure of isotopes far from stability.

Purpose Extend our knowledge about the evolution of the $1/2^+$ and $3/2^+$ states for K isotopes beyond the $N = 28$ shell gap.

Method High-resolution collinear laser spectroscopy on bunched atomic beams.

Results From measured hyperfine structure spectra of K isotopes, nuclear spins and magnetic moments of the ground states were obtained for isotopes from $N = 19$ up to $N = 32$. In order to draw conclusions about the composition of the wave functions and the occupation of the levels, the experimental data were compared to shell-model calculations using SDPF-NR and SDPF-U effective interactions. In addition, a detailed discussion about the evolution of the gap between proton $1d_{3/2}$ and $2s_{1/2}$ in the shell model and *ab initio* framework is also presented.

Conclusions The dominant component of the wave function for the odd- A isotopes up to ^{45}K is a $\pi 1d_{3/2}^{-1}$ hole. For $^{47,49}\text{K}$, the main component originates from a $\pi 2s_{1/2}^{-1}$ hole configuration and it inverts back to the $\pi 1d_{3/2}^{-1}$ in ^{51}K . For all even- A isotopes, the dominant configuration arises from a $\pi 1d_{3/2}^{-1}$ hole coupled to a neutron in the $\nu 1f_{7/2}$ or $\nu 2p_{3/2}$ orbitals. Only for ^{48}K , a significant amount of mixing with $\pi 2s_{1/2}^{-1} \otimes \nu(pf)$ is observed leading to a $I^\pi = 1^-$ ground state. For ^{50}K , the ground-state spin-parity is 0^- with leading configuration $\pi 1d_{3/2}^{-1} \otimes \nu 2p_{3/2}^{-1}$.

*jasna.papuga@fys.kuleuven.be

I. INTRODUCTION

The shell structure of nuclei established by Goeppert-Mayer [1] and Haxel *et al.* [2] more than 60 years ago is the corner stone of nuclear structure described by the shell model. However, a few decades later, with systematic studies of nuclei with large N/Z ratio, known as "exotic nuclei", it was observed that the original shell gaps are not preserved and "new" shell closures appear [3–5]. This fact continues to attract the attention of many experimentalists and theorists who try to understand the origin of these changes. Nowadays, despite the experimental challenges, a large variety of exotic nuclei can be produced and studied with the highest precision in facilities around the world [6, 7]. These experimental data are used by theorists for fine tuning of the effective interactions in order to improve their descriptive as well as predictive power [8].

In the past decade, the region below Ca ($Z < 20$) with $20 \leq N \leq 28$ was investigated intensively, in particular the evolution of the πsd orbitals as a function of neutron number (for review see, e.g., Refs. [9, 10]). The energy spacing between the $1/2^+$ and $3/2^+$ levels as a function of the $\nu f_{7/2}$ occupancy and the evolution of the $N = 20$ and $N = 28$ shell gaps with decreasing Z for odd- A K ($Z = 19$), Cl ($Z = 17$) and P ($Z = 15$) was presented by Gade *et al.* [10], with experimental results compared to shell-model calculations up to $N = 28$. The inversion of the $1/2^+$ and $3/2^+$ states in the Cl chain is observed for the half-filled $\nu 1f_{7/2}$ orbital. The same effect appears for potassium isotopes, but only when the same orbital is completely filled, at $N = 28$. In addition, the evolution of the effective single-particle energies (ESPE) for potassium isotopes (single-hole states in Ca isotopes) based on shell-model calculations is discussed by Smirnova *et al.* in Ref. [11], where a degeneracy of the $\pi 2s_{1/2}$ and $\pi 1d_{3/2}$ levels is predicted to occur at $N = 28$ and returns to a "normal" ordering ($\pi 2s_{1/2}$ below $\pi 1d_{3/2}$) approaching $N = 40$ (Fig 1(c) in Ref. [11]). The reordering of the orbitals is driven by the monopole part of the proton-neutron interaction, which can be decomposed into three components: the central, vector and tensor. Initially Otsuka *et al.* [12] suggested that the evolution of the ESPEs is mainly due to the tensor component. However, in more recent publications [11, 13, 14] several authors have shown that both the tensor term as well as the central term have to be considered.

Regarding the shell model, potassium isotopes are excellent probes for this study, with only one proton less than the magic number $Z = 20$. Nevertheless, little and especially

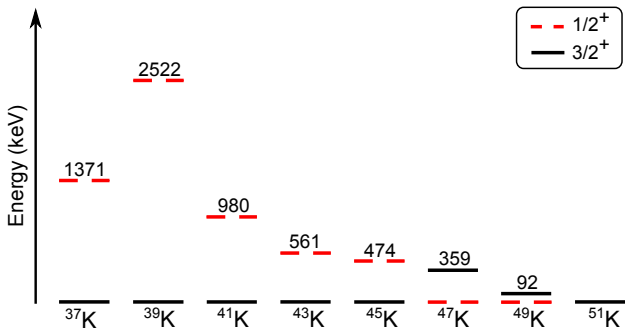


FIG. 1: (Color online) Experimental energies for $1/2^+$ and $3/2^+$ states in odd- A K isotopes. Inversion of the nuclear spin is obtained in $^{47,49}\text{K}$ and reinversion back in ^{51}K . Results are taken from [16, 23–25]. Ground-state spin for ^{49}K and ^{51}K were established [22].

conflicting information is available so far for the neutron-rich potassium isotopes. Level schemes based on the tentatively assigned spins of the ground state were provided for ^{48}K [15] and ^{49}K [16]. In addition, an extensive discussion was presented by Gaudefroy [17] on the energy levels and configurations of $N = 27, 28$ and 29 isotones in the shell-model framework and compared to the experimental observation, where available. However, the predicted spin of 2^- for ^{48}K , is in contradiction with $I^\pi = (1^-)$ proposed by Królas *et al.* [15]. In addition, the nuclear spin of the ground state of ^{50}K was proposed to be 0^- [18] in contrast to the recent β -decay studies where it was suggested to be 1^- [19]. The ground state spin-parity of ^{49}K was tentatively assigned to be $(1/2^+)$ by Broda *et al.* [16], contrary to the earlier tentative $(3/2^+)$ assignment from β -decay spectroscopy [20]. For ^{51}K , the nuclear spin was tentatively assigned to be $(3/2^+)$ by Perrot *et al.* [21].

Our recent hyperfine structure measurements of potassium isotopes using the collinear laser spectroscopy technique provided unambiguous spin values for $^{48-51}\text{K}$ and gave the answer to the question as to what happens with the proton sd orbitals for isotopes beyond $N = 28$. By measuring the nuclear spins of ^{49}K and ^{51}K to be $1/2$ and $3/2$, [22] respectively, the evolution of these two states in the potassium isotopes is firmly established. This is presented in Fig. 1 for isotopes from $N = 18$ up to $N = 32$ where the inversion of the states is observed at $N = 28$ followed by the reinversion back at $N = 32$. In addition, we have confirmed a spin-parity 1^- for ^{48}K and 0^- for ^{50}K [26]. The measured magnetic moments

of $^{48-51}\text{K}$ were not discussed in detail so far and will be presented in this article. Additionally, based on the comparison between experimental data and shell-model calculations, the configuration of the ground-state wave functions will be addressed as well. Finally, *ab initio* Gorkov-Green's function calculations of the odd- A isotopes will be discussed.

II. EXPERIMENTAL PROCEDURE

The experiment was performed at the collinear laser spectroscopy beam line COLLAPS [27] at ISOLDE/CERN. The radioactive ion beam was produced by 1.4-GeV protons (beam current about $1.7\ \mu\text{A}$) impinging on a thick UC_x target ($45\ \text{g}/\text{cm}^2$). Ionization of the resulting fragments was achieved by the surface ion source. The target and the ionizing tube were heated to around 2000°C . The accelerated ions (up to 40 kV) were mass separated by the high resolution separator (HRS). The gas-filled Paul trap (ISCOOL) [28, 29] was used for cooling and bunching of the ions. Multiple bunches spaced by 90 ms were generated after each proton pulse. The bunched ions were guided to the setup for collinear laser spectroscopy where they were superimposed with the laser. A schematic representation of the beam line for collinear laser spectroscopy is shown in Fig. 2.

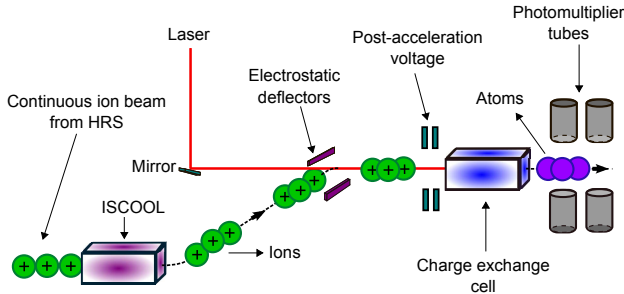


FIG. 2: (Color online) Schematic representation of the setup for collinear laser spectroscopy at ISOLDE.

A cw titanium:sapphire (Ti:Sa) laser was operated close to the Doppler-shifted $4s\ ^2S_{1/2} \rightarrow 4p\ ^2P_{1/2}$ transition at 769.9 nm, providing around 1 mW power into the beam line. Stabilization of the laser system during the experiment was ensured by locking the laser to a reference Fabry-Perot interferometer maintained under vacuum, which in turn was locked to a frequency stabilized helium-neon (HeNe) laser. An applied voltage of $\pm 10\ \text{kV}$ on the

charge exchange cell (CEC) provided the Doppler tuning for the ions, which were neutralized through the collisions with potassium vapor. Scanning of the hyperfine structure (hfs) was performed by applying an additional voltage in a range of ± 500 V. The resonance photons were recorded by four photomultiplier tubes (PMT) placed immediately after the CEC. By gating the signal on the PMTs to the fluorescence photons from the bunches, the signal was only recorded for about $6\ \mu\text{s}$ when the bunches were in front of the PMTs. Consequently, the background related to the scattered laser light was suppressed by a factor $\sim 10^4$ ($6\ \mu\text{s}/90\ \text{ms}$). More details about the setup can be found in Ref. [26].

III. RESULTS

In Fig. 3 typical hyperfine spectra for $^{48-51}\text{K}$ are shown. The raw data are saved as counts versus scanning voltage. The conversion from voltage to frequency was carried out by using the masses from [30] and applying the relativistic Doppler formula. The spectra were fitted with a Voigt line shape using common width for all components. The χ^2 -minimization procedure MINUIT [31] was used with A parameters [$A(S_{1/2})$ and $A(P_{1/2})$], the center of gravity and the intensities left as free fit parameters. Nuclear spins, magnetic moments, and changes in mean square charge radii were extracted model independently. From the intensity ratios of the hyperfine components, the nuclear spin of ^{48}K and ^{51}K were determined to be $I = 1$ [26] and $I = 3/2$ [22], respectively. Since only three peaks are observed in the hyperfine spectrum of ^{49}K , a spin of $I = 1/2$ can be unambiguously assigned [22]. A single peak in the hyperfine spectrum of ^{50}K corresponds to $I = 0$ [26]. The deduced magnetic moments and the implication for the nuclear structure of the potassium isotopes will be reported in this article.

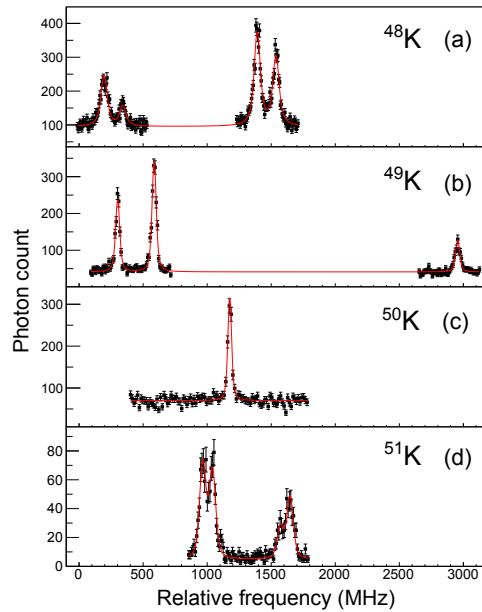


FIG. 3: (Color online) The hyperfine spectra of $^{48-51}\text{K}$ (a)-(d) obtained by collinear laser spectroscopy. The spectra are shown relative to the centroid of ^{39}K .

The observed hyperfine A parameters of the ground and the excited states for all studied isotopes are presented in Table I. The results are compared to the literature values from [32–34]. Compared to the results from earlier atomic beam laser spectroscopy studies [32], the precision has been increased by an order of magnitude for most of the values. The hyperfine A parameters for $^{48-51}\text{K}$ were measured for the first time. For the isotopes/isomer with $I = 0$, there is no hyperfine splitting of the atomic states, thus the A parameters are equal to 0.

The relation between A parameters and magnetic moments is given by $A = \mu B_0 / IJ$, where B_0 is the magnetic field induced by the electron cloud at the position of the nucleus. As B_0 is to first order isotope independent, magnetic moments were deduced relative to ^{39}K using Eq. (1):

$$\mu = \frac{A(^2S_{1/2})I}{A_{\text{ref}}(^2S_{1/2})I_{\text{ref}}} \mu_{\text{ref}}. \quad (1)$$

TABLE I: Magnetic hyperfine parameters for neutral potassium from this work and comparison with literature values [32–34].

Isotope	I^π	$A(^2S_{1/2})$ (MHz)	$A(^2P_{1/2})$ (MHz)	$A_{\text{lit}}(^2S_{1/2})$ (MHz)	$A_{\text{lit}}(^2P_{1/2})$ (MHz)
^{38}K	3^+	+404.3 (3)	+48.9 (2)	+404.369 (3)	–
^{38m}K	0^+	0	0	–	–
^{39}K	$3/2^+$	+231.0 (3)	+27.8 (2)	+231.0 (3)	+27.5(4)
^{42}K	2^-	-503.7 (3)	-61.2 (2)	-503.550779 (5)	-60.6(16)
^{44}K	2^-	-378.9 (4)	-45.8 (2)	-378.1 (11)	-44.9(11)
^{46}K	2^-	-462.8 (3)	-55.9 (2)	-465.1 (12)	-55.7(13)
^{47}K	$1/2^+$	+3413.2 (3) ^a	+411.8 (2)	+3420.2 (29)	+411.9(50)
^{48}K	1^-	-795.9 (3)	-96.3 (3)	–	–
^{49}K	$1/2^+$	+2368.2 (14)	+285.6 (7)	–	–
^{50}K	0^-	0	0	–	–
^{51}K	$3/2^+$	+302.5 (13)	+36.6 (9)	–	–

^aAfter reanalysis, the uncertainty on this value was increased from 0.2 to 0.3 MHz.

The reference values were taken from atomic-beam magnetic resonance measurements, where precise values are reported to be $A_{\text{ref}}(^2S_{1/2}) = +230.8598601 (7)$ MHz and $\mu_{\text{ref}} = +0.3914662(3) \mu_N$ [35].

As the magnetic moments of potassium isotopes were determined with $10^{-3} - 10^{-4}$ relative precision, one cannot neglect the hfs anomaly between two isotopes, arising from the finite size of the nuclei. This slightly modifies the A parameters [36] and gives a small correction of Eq. (1) which is expressed by

$${}^{39}\Delta^A = \frac{A^{39}(S_{1/2})/g({}^{39}\text{K})}{A^A(S_{1/2})/g({}^A\text{K})} - 1, \quad (2)$$

being different from zero. In Eq. (2), the g factor is $g = \mu/I$. The dominant contributions to the hfs anomaly are originating from the difference in the nuclear magnetization distribution (Bohr-Weisskopff effect [37]) and difference of the charge distribution (Breit-Rosenthal effect [38]). In the case of potassium isotopes, the hfs anomaly was measured for $^{38-42}\text{K}$ relative to ${}^{39}\text{K}$ [33–35, 39, 40]. In order to assess the additional uncertainty on the magnetic moments for all measured isotopes, the hfs anomaly was estimated from the experimental data as well

as from theoretical calculations.

According to the approach proposed by Ehlers *et al.* [41], the differential hyperfine structure anomaly ($^{39}\delta^A$) between two different electronic states is defined as

$$^{39}\delta^A = \frac{A^{39}(S_{1/2})/A^{39}(P_{1/2})}{A^A(S_{1/2})/A^A(P_{1/2})} - 1, \quad (3)$$

where the A parameters for the reference isotope ^{39}K were taken from literature [35, 42]. The value of the hyperfine structure anomaly can be approximated by the differential hyperfine structure anomaly, which is good to a few percent. This is good enough considering the accuracies of our experimental results. Differential hyperfine anomalies are presented in Table II (column 3). For $^{40,41}\text{K}$, the experimental results from literature were used: the $A(S_{1/2})$ parameter from [35, 39], while the $A(P_{1/2})$ parameters were taken from [42]. It should be noted that for $^{43,45}\text{K}$ no data for $A(P_{1/2})$ were obtained. In addition, theoretical calculations were performed following Bohr [36]. The hfs anomaly was estimated to be $^{39}\Delta_{\text{theo}}^A = \epsilon(^{39}\text{K}) - \epsilon(^A\text{K})$, where $\epsilon(^A\text{K})$ is a perturbation factor due to the finite size of the nucleus. It can be calculated using [36]

$$\epsilon = -[(1 + 0.38\zeta)\alpha_s + 0.62\alpha_l]b(Z, R_0)(R/R_0)^2. \quad (4)$$

In Ref. [36], all parameters from Eq. (4) are defined and for some of them values are tabulated. Theoretical estimations of the ϵ parameter and hfs anomaly ($^{39}\Delta_{\text{theo}}^A$) are listed in Table II (columns 4 and 5). Hyperfine structure anomalies of the potassium isotopes known from the literature [33–35, 39, 40] are shown in the last column of Table II ($^{39}\Delta_{\text{lit}}^A$). For all isotopes except ^{42}K , the hyperfine structure anomaly estimated from the experimental results is in agreement with the calculated ones. The values for odd-odd nuclei are systematically higher than for odd-even, thus we will quote different additional uncertainties on the magnetic moments (in square brackets in Tables III and VII), namely 0.3% and 0.5% for odd- A and even- A isotopes, respectively.

TABLE II: Estimated hyperfine structure anomalies of potassium isotopes. Experimental results for the hyperfine parameters were used to calculate $(^{39}\delta^A)$ from Eq. (3). For $^{40,41}\text{K}$ experimental data were taken from [35, 39, 42]. The $\epsilon(^A\text{K})$ parameters for all isotopes are calculated from Eq. (4) and are listed in the next column. For the reference isotope, it was found to be $\epsilon(^{39}\text{K}) = 0.165$. The estimated hyperfine structure anomalies from the model ($^{39}\Delta_{\text{theo}}^A$) described by Bohr (see text for details) are shown as well. In the last column, the hyperfine structure anomalies from literature ($^{39}\Delta_{\text{lit}}^A$) are given [33–35, 39, 40].

Isotope	I^π	$^{39}\delta^A$ (%)	$\epsilon(^A\text{K})$	$^{39}\Delta_{\text{theo}}^A$ (%)	$^{39}\Delta_{\text{lit}}^A$ (%)
^{38}K	3^+	0.53 (44)	-0.006	0.17	0.17(6)
^{40}K	4^-	0.43 (17)	-0.379	0.54	0.466 (19)
^{41}K	$3/2^+$	-0.23 (31)	0.398	-0.23	-0.226 (10)
					-0.22936 (14)
^{42}K	2^-	0.99 (36)	-0.265	0.43	0.336 (38)
^{43}K	$3/2^+$	-	0.560	-0.39	-
^{44}K	2^-	0.47 (47)	-0.302	0.47	-
^{45}K	$3/2^+$	-	0.521	-0.36	-
^{46}K	2^-	0.40 (39)	-0.275	0.44	-
^{47}K	$1/2^+$	0.28 (16)	-0.126	0.29	-
^{48}K	1^-	0.57 (35)	-0.211	0.38	-
^{49}K	$1/2^+$	0.24 (29)	-0.121	0.29	-
^{51}K	$3/2^+$	0.57 (250)	0.097	0.07	-

IV. DISCUSSION

Nuclei with one particle or one hole next to a shell closure are excellent probes for testing shell-model interactions. In this context, the investigation of the potassium chain is of great interest, since it has a hole in the πsd orbital and it covers two major neutron shells, $N = 20$ and $N = 28$, and one subshell at $N = 32$.

In what follows, the experimental results from our work are compared to shell-model predictions. The calculations were carried out using the ANTOINE code [43] for two effective interactions: SDPF-NR [44, 45] and SDPF-U [46]. The latter is a more recent version of the

SDPF-NR interaction where the monopole part was refitted by including more experimental results from nuclei with one particle or one hole next to the closed shell for protons or neutrons such as ^{35}Si , ^{47}Ar and ^{41}Ca . The calculations have been performed in the $0\hbar\omega$ shell model space beyond a ^{16}O core and with valence protons restricted to sd orbitals and neutrons to sd or pf orbitals. Neutron excitations across $N = 20$ were prohibited. In order to account for missing interactions among the valence nucleons as well as with the nucleons from the core, the calculations were performed using effective g factors: the spin g factors were fixed at $g_s^{\text{eff}} = 0.85g_s^{\text{free}}$, while the orbital g factors were fixed to $g_l^\pi = 1.15$ and $g_l^\nu = -0.15$ [47].

A. Odd- A

Nuclear properties such as the ground-state spin and magnetic moment of odd- A K isotopes (odd-even isotopes) are determined by an unpaired proton placed in the πsd orbital whilst the even number of neutrons are coupled to spin zero. In the simple shell-model framework the measured nuclear spin indicates the dominant component of the ground-state wave function. Based on this simple model, one would expect that the magnetic moments of these isotopes are equal to the single-particle magnetic moments of the orbital where a valence proton is located. However, the observed deviation from the single-particle values reveals influence of the proton-neutron interaction leading to a more collective behavior. Although the magnetic moments of the neutron-rich odd- A K isotopes were already published in [22], a detailed discussion over the entire odd- A chain from $N = 20$ up to $N = 32$ will be presented here with additional focus on the monopole interaction responsible for the shell evolution.

The experimentally observed magnetic moments are listed in Table III together with the values predicted by shell-model calculations using the SDPF-NR and SDPF-U effective interactions. In the same table, the calculated percentage of the component of the ground-state wave function originating from a hole in the $\pi 1d_{3/2}^{-1}$ is shown as well.

In Fig. 4 the experimental magnetic moments for odd- A K isotopes are compared to the results from the shell-model calculations. In general a very good agreement between experimental and theoretical results is observed. The discrepancy for ^{39}K and ^{41}K might be due to excitation across the $Z, N = 20$ shell gaps, which were not considered in these calculations. This problem is especially pronounced for ^{39}K where, the shell-model calculations yield a

TABLE III: Experimental magnetic moments (in units of μ_N) compared with the calculated ones using two effective interactions: SDPF-NR and SDPF-U. The predicted amount of the $\pi 1d_{3/2}^{-1} \otimes \nu(f_0)$ in the ground-state wave function is given in %. If available, the literature values are shown as well. The uncertainty in the square brackets is due to the hyperfine structure anomaly and is 0.3%.

Isotope	I^π	μ_{exp}	$\mu_{\text{SDPF-NR}}$	$\pi 1d_{3/2}^{-1}$ (%)	$\mu_{\text{SDPF-U}}$	$\pi 1d_{3/2}^{-1}$ (%)	μ_{lit}	Ref.
^{39}K	$3/2^+$	+0.3917(5) [12]	+0.65	100%	+0.65	100%	+0.3914662(3)	[35]
^{41}K	$3/2^+$	-	+0.37	95%	+0.33	95%	+0.2148701(2)	[35]
^{43}K	$3/2^+$	-	+0.22	92%	+0.17	92%	+0.1633(8) ^a	[32]
^{45}K	$3/2^+$	-	+0.23	88%	+0.21	90%	+0.1734(8) ^a	[32]
^{47}K	$1/2^+$	+1.9292(2) [58]	+1.87	13%	+1.91	13%	+1.933(9) ^a	[32]
^{49}K	$1/2^+$	+1.3386(8) [40]	+1.61	21%	+1.81	15%	-	-
^{51}K	$3/2^+$	+0.5129(22) [15]	+0.60	90%	+0.65	93%	-	-

^aIncluded 0.5% uncertainty on the error to account for the hyperfine structure anomaly.

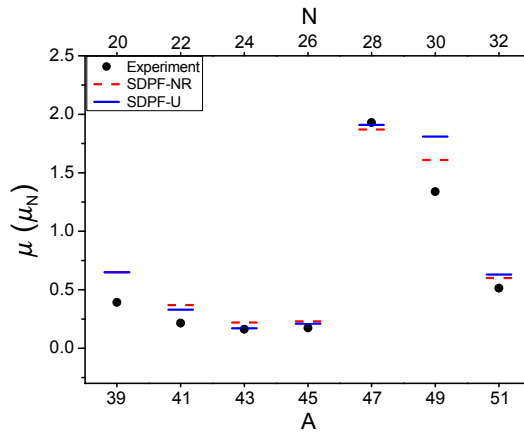


FIG. 4: (Color online) Experimental magnetic moments (black dots) compared to the shell-model calculation using SDPF-NR (red dashed line) and SDPF-U (blue solid line) interactions and effective g factors (see text for more details). In general a very good agreement between experimental and theoretical results is observed, except for ^{39}K and ^{49}K .

pure $\pi 1d_{3/2}^{-1}$ state with a magnetic moment about 60% larger than the experimental value. Both effective interactions yield almost identical amounts of the $\pi 1d_{3/2}^{-1} \otimes \nu(pf)$ component in the ground state of odd- A isotopes. It is more than 90% for all isotopes up to ^{45}K , but for $^{47,49}\text{K}$ the wave function is dominated by the $\pi 2s_{1/2}^{-1} \otimes \nu(pf)$ configuration. This was already concluded in [22], the conclusion based on the measured ground-state spin and g factor. The only noticeable difference between both calculations is found for ^{49}K , where the contribution from $\pi 1d_{3/2}^{-1} \otimes \nu(pf)$ is predicted to be 21% from SDPF-NR and 15% from SDPF-U. In both cases the calculated value deviates from the experimental one, but SDPF-U shows a larger deviation. From a two-state mixing calculation, at least 25 % [48] of mixing with the $[\pi 1d_{3/2}^{-1} \otimes \nu(pf)_{2+}]_{1/2+}$ is needed to reproduce the observed magnetic moment.

The inversion of the nuclear spin from $I = 3/2$ to $I = 1/2$ at $N = 28$ and the reinversion back to $I = 3/2$ at $N = 32$ is related to the evolution of the proton orbitals (πsd) while different neutron orbitals are being filled. This evolution is driven by the monopole term of the nucleon-nucleon (NN) interaction. According to Otsuka *et al.* [14], the interaction has a linear dependence on the occupation number and consists of three parts: central, vector and tensor. Applying the spin-tensor decomposition method [11, 13], it is possible to separate the contribution of different components of the effective NN interaction. This leads to a qualitative analysis of the role of each part separately in the evolution of the effective single-particle energies (ESPEs). The calculated centroids for every component of the monopole interaction are listed in Table IV. The centroid of the proton-neutron interaction is defined as [49]

$$V_{j_\pi j_\nu} = \frac{\sum_J (2J+1) \langle j_\pi j_\nu | V | j_\pi j_\nu \rangle}{\sum_J (2J+1)}, \quad (5)$$

where j_π and j_ν stand for the angular momentum of proton and neutron orbitals, $\langle j_\pi j_\nu | V | j_\pi j_\nu \rangle$ is the two-body matrix element and J is the total angular momentum of a proton-neutron state. The summation runs over all possible values of J .

Based on the results presented in Table IV, the central component of the interaction is by far the largest (columns 3,4 and 6,7) and, thus has the strongest influence on the energy shift. Note that there is no tensor component for the $s_{1/2}$ orbital due to the absence of a preferred orientation of the spin for an $l = 0$ state [12].

TABLE IV: Spin-tensor content of the centroids of the SDPF-NR and SDPF-U interaction, defining the proton $1d_{3/2}$ - $2s_{1/2}$ gap. Results are presented in MeV.

Interaction	Component	$V_{d_{3/2}f_{7/2}}^{\pi\nu}$	$V_{s_{1/2}f_{7/2}}^{\pi\nu}$	ΔV	$V_{d_{3/2}p_{3/2}}^{\pi\nu}$	$V_{s_{1/2}p_{3/2}}^{\pi\nu}$	ΔV
SDPF-NR	Central	-1.66	-1.26	-0.40	-1.34	-1.46	+0.12
	Vector	+0.28	+0.17	+0.11	+0.21	+0.22	-0.01
	Tensor	-0.28	0.00	-0.28	-0.08	0.00	-0.08
	Total	-1.66	-1.09	-0.57	-1.21	-1.24	+0.03
	Central	-1.51	-1.21	-0.30	-1.05	-1.21	+0.16
	Vector	+0.09	+0.07	+0.02	+0.05	-0.11	+0.16
	Tensor	-0.28	0.00	-0.28	-0.06	0.00	-0.06
	Total	-1.70	-1.14	-0.56	-1.06	-1.32	+0.26

The change of the energy gap between $\pi 1d_{3/2}$ and $\pi 2s_{1/2}$ depends on the difference ΔV between the two centroids (Table IV; columns 5 and 8). The evolution of the energy gap from $N = 20$ to $N = 28$ and from $N = 28$ to $N = 32$, along with the spin-tensor decomposition of this energy gap, is presented in Table V.

Both interactions predict the same decrease of the gap by -3.15 MeV for isotopes from $N = 20$ up to $N = 28$ (Table V; columns 2 and 3), although the central and vector contribution are significantly different in both interactions. Once the $\nu p_{3/2}$ orbital is involved, for isotopes from $N = 29$ up to $N = 32$, the situation changes. The increase in the gap between

TABLE V: Calculated contributions of the different spin-tensor terms of SDPF-NR ("NR") and SDPF-U ("U") to the evolution of the energy gap between effective $\pi 1d_{3/2}$ and $\pi 2s_{1/2}$ when filling $\nu 1f_{7/2}$ and $\nu 2p_{3/2}$ orbitals. The results are given in MeV.

filling	$\nu 1f_{7/2}$		$\nu 2p_{3/2}$	
	NR	U	NR	U
Central	-2.09	-1.58	+0.46	+0.58
Vector	+0.58	+0.06	-0.06	+0.43
Tensor	-1.64	-1.64	-0.17	-0.12
Total	-3.15	-3.16	+0.23	+0.89

$\pi 1d_{3/2}$ and $\pi 2s_{1/2}$ (Table V; columns 4 and 5) is mostly driven by the central component in the SDPF-NR interaction, while also the vector component contributes significantly in the SDPF-U. Therefore, the calculated change in the energy gap is very different: +0.23 MeV and +0.89 MeV, respectively. This results in different calculated spectra for ^{49}K and ^{51}K as illustrated in Fig. 5. This figure shows the energy difference between the lowest $1/2^+$ and $3/2^+$ states for isotopes in the range from $N = 24$ up to $N = 34$ compared to the calculated values.

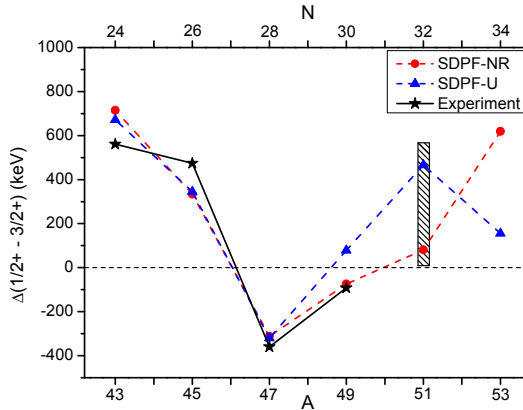


FIG. 5: (Color online) Energy difference between the two lowest states with $I^\pi = 1/2^+$ and $3/2^+$ for odd- A K isotopes from $N = 24$ up to $N = 34$. Experimental results (black stars) taken from [16, 23–25] are in good agreement with the shell-model calculations using different effective interactions: SDPF-NR (red dots) and SDPF-U (blue triangles). For ^{49}K , only the SDPF-NR interaction correctly predicts the spin of the ground state to be $1/2^+$. The shaded area represents the expected region based on the measured ground-state spin and the shell-model calculation for the first excited state in ^{51}K .

Up to $N = 28$, both interactions are in agreement with the experimental results. The deviation between both effective interactions increases beyond $N = 28$ when the $\nu 2p_{3/2}$ and higher orbitals are involved. For ^{49}K , both interactions calculate the energy difference between the ground and first excited state to be about 75 keV, but only the SDPF-NR predicts the correct ground-state spin. Although both effective interactions predicted the correct ground-state spin for ^{51}K , experimental data on the energy of the first-excited state

is needed to further test the validity of both models. Beyond $N = 32$ the predicted ground-state spin $3/2$ for ^{53}K needs experimental verification, as well as the energy of the first excited $1/2^+$ state, which is very different in both calculations.

Very recently, *ab initio* calculations of open-shell nuclei have become possible in the Ca region [50] on the basis of the self-consistent Gorkov-Green's function formalism [51]. State-of-the-art chiral two- (NN) [52, 53] and three-nucleon ($3N$) [54] interactions adjusted to two-, three- and four-body observables (up to ^4He) are employed, without any further modification, in the computation of systems containing several tens of nucleons. We refer to Ref. [50] for further details. In the present study, Gorkov-Green's function calculations of the lowest $1/2^+$ and $3/2^+$ states in $^{37-53}\text{K}$ have been performed by removing a proton from $^{38-54}\text{Ca}$. Similarly to Fig. 5, the upper panel of Fig. 6 compares the results to experimental data. The calculated energy differences have been shifted down by 2.58 MeV to match the experimental value for ^{47}K . The overestimation of energy differences is a general feature of calculated odd- A spectra and actually correlates with the systematic overbinding of neighboring even- A ground states [50]. Still, one observes the correct *relative* evolution of the $1/2^+$ state with respect to the $3/2^+$ when going from ^{37}K to ^{47}K and then from ^{47}K to ^{49}K . This result is very encouraging for these first-ever systematic *ab initio* calculations in mid-mass nuclei. Indeed, it allows one to speculate that correcting in the near future for the systematic overbinding produced in the Ca region by currently available chiral interactions, and thus for the too spread out spectra of odd- A systems, might bring the theoretical calculation in good agreement with experiment. Although this remains to be confirmed, it demonstrates that systematic spectroscopic data in mid-mass neutron-rich nuclei provide a good test case to validate/invalidate specific features of basic inter-nucleon interactions and innovative many-body theories.

To complement the above analysis, the lower panel of Fig. 6 provides the evolution of proton $1d_{3/2}$ and $2s_{1/2}$ shells. These two effective single-particle energies (ESPEs) recollect [51] the fragmented $3/2^+$ and $1/2^+$ strengths obtained from one-proton addition and removal processes on neighboring Ca isotones. Within the present theoretical description, the evolution of the observable (i.e. theoretical-scheme independent) lowest-lying $1/2^+$ and $3/2^+$ states does qualitatively reflect the evolution of the underlying non-observable (i.e. theoretical-scheme dependent) single-particle shells. As such, the energy gap between the two shells decreases from 5.76 MeV in ^{39}K to 1.81 MeV in ^{47}K which is a reduction of about 70%. Adding four neutrons in the $\nu 2p_{3/2}$ shell causes the energy difference to increase again

to 4.03 MeV.

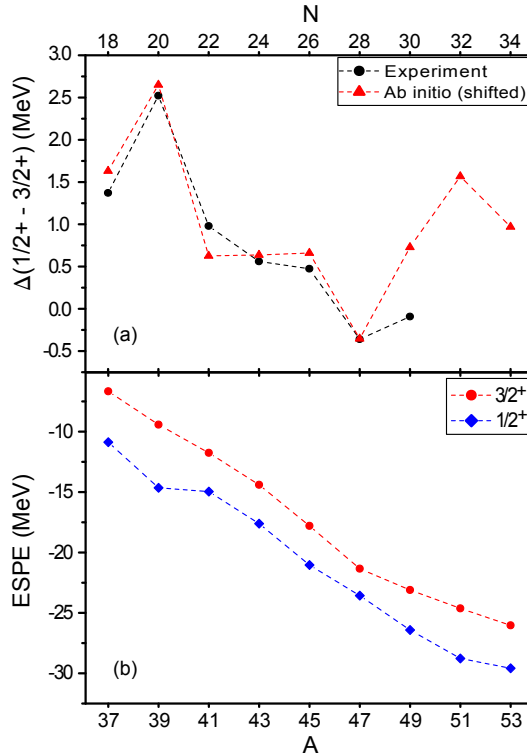


FIG. 6: (Color online) (a) Energy difference between the lowest $1/2^+$ and $3/2^+$ states obtained in $^{37-53}\text{K}$ from *ab initio* Gorkov-Green's function calculations and experiment. *Ab initio* results have been shifted by 2.58 MeV to match the experimental $(1/2^+ - 3/2^+)$ splitting in ^{47}K . (b) $\pi d_{3/2}$ and $\pi s_{1/2}$ effective single-particle energies (ESPE) in $^{37-53}\text{K}$ calculated in Gorkov-Green's functions theory.

B. Even- A

The configuration of the even- A potassium isotopes arises from the coupling between an unpaired proton in the sd shell with an unpaired neutron. Different neutron orbitals are involved, starting from ^{38}K where a hole in the $\nu 1d_{3/2}$ is expected, then gradually filling the $\nu 1f_{7/2}$ and finally, the $\nu 2p_{3/2}$ for $^{48,50}\text{K}$.

In order to investigate the composition of the ground-state wave functions of the even- A K isotopes, we first compare the experimental magnetic moments to the semi-empirical values. Based on the additivity rule for the magnetic moments (g factors) and assuming a weak coupling between the odd proton and the odd neutron, the semi-empirical magnetic moments can be calculated using the following formula [55]: $\mu_{\text{se}} = g_{\text{se}} \cdot I$, with

$$g_{\text{se}} = \frac{g(j_\pi) + g(j_\nu)}{2} + \frac{g(j_\pi) - g(j_\nu)}{2} \frac{j_\pi(j_\pi + 1) - j_\nu(j_\nu + 1)}{I(I + 1)}, \quad (6)$$

where $g(j_\pi)$ and $g(j_\nu)$ are the experimental g factors of nuclei with an odd proton or neutron in the corresponding orbital. The calculations were performed using the measured g factors of the neighboring isotopes with the odd-even and even-odd number of particles in j_π and j_ν , respectively. For the empirical values of unpaired protons, results from Table III were used. The g factors for the odd neutrons were taken from the corresponding Ca isotones [56–59]. The obtained results with the list of isotopes used for different configurations are presented in Table VI.

TABLE VI: Semi-empirical g factors obtained for certain configurations using the additivity rule in Eq. (6) (see text for more details). In the calculations, results from Table III were used for $g(j_\pi)$, while for $g(j_\nu)$ Ca data were taken from [56–59]. For ^{48}K , different configurations are considered for $I = 1$.

Isotope	I^π	configuration	g_{se}	$(g(j_\pi); g(j_\nu))$
^{38}K	3^+	$\pi 1d_{3/2}^{-1} \otimes \nu 1d_{3/2}^{-1}$	+0.47	$(^{39}\text{K}; ^{39}\text{Ca})$
^{40}K	4^-	$\pi 1d_{3/2}^{-1} \otimes \nu 1f_{7/2}$	-0.31	$(^{39}\text{K}; ^{41}\text{Ca})$
^{42}K	2^-	$\pi 1d_{3/2}^{-1} \otimes \nu 1f_{7/2}^3$	-0.64	$(^{41}\text{K}; ^{43}\text{Ca})$
^{44}K	2^-	$\pi 1d_{3/2}^{-1} \otimes \nu 1f_{7/2}^5$	-0.62	$(^{43}\text{K}; ^{45}\text{Ca})$
^{46}K	2^-	$\pi 1d_{3/2}^{-1} \otimes \nu 1f_{7/2}^{-1}$	-0.65	$(^{45}\text{K}; ^{47}\text{Ca})$
^{48}K	1^-	$\pi 1d_{3/2}^{-1} \otimes \nu 2p_{3/2}$	-0.40	$(^{45}\text{K}; ^{49}\text{Ca})$
^{48}K	1^-	$\pi 2s_{1/2}^{-1} \otimes \nu 2p_{3/2}$	-2.11	$(^{47}\text{K}; ^{49}\text{Ca})$

A comparison between the experimental and semi-empirical g factors is shown in Fig. 7. For ^{38}K , the semi-empirical value calculated from ^{39}K and ^{39}Ca provides excellent agreement with the experimental result. This confirms that the dominant component in the wave function for the ground state originates from the coupling between a hole in the $\pi 1d_{3/2}$

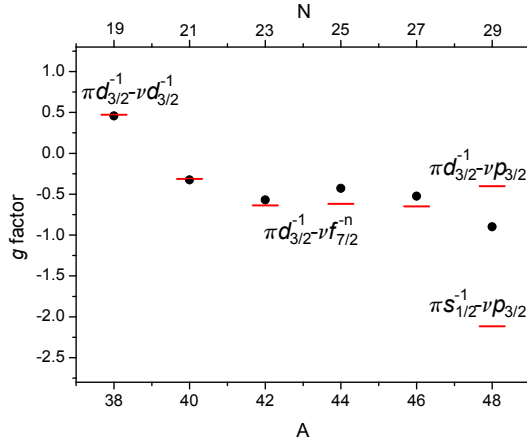


FIG. 7: (Color online) Experimental g factors (black dots) compared to the semi-empirical values (red solid line) calculated from the neighboring isotopes. Based on the good agreement between the experimental and semi-empirical g factors, the dominant component of the wave functions can be easily established for $^{38-46}\text{K}$. Only for ^{48}K a strong mixing between the $\pi 2s_{1/2}^{-1} \otimes \nu 2p_{3/2}$ and the $\pi 1d_{3/2}^{-1} \otimes \nu 2p_{3/2}$ in the wave function is found.

and the $\nu 1d_{3/2}$. By adding more neutrons, the $\nu 1f_{7/2}$ orbital is filled for ^{40}K up to ^{46}K . In order to calculate the semi-empirical g factors for these isotopes, $g(j_\pi)$ is provided from neighboring odd- A K isotopes (Table III) combined with $g(j_\nu)$ of the subsequent odd- A Ca isotones starting from $N = 21$ up to $N = 27$. The trend of the experimental g factors is very well reproduced by the semi-empirical calculations suggesting that the dominant component in the wave function of these isotopes is $\pi 1d_{3/2}^{-1} \otimes \nu 1f_{7/2}^n$ where $n = 1, 3, 5, 7$. For ^{48}K , two semi-empirical values are calculated by considering a coupling between a proton hole in the $\pi 2s_{1/2}$ or the $\pi 1d_{3/2}$ with neutrons in the $\nu 2p_{3/2}$ orbital. Comparing the experimental g factor to the semi-empirical results, it is possible to conclude that the main component in the wave function of this isotope arises from the configuration with a hole in the $\pi 1d_{3/2}$. Nevertheless, the deviation of the experimental result from the semi-empirical g factors is due to a large amount of mixing between both configurations in the wave function. ^{50}K is not presented because the observed $I = 0$ leads to $\mu = 0$. There are two possible configurations which would yield this particular spin: $\pi 1d_{3/2}^{-1} \otimes \nu 2p_{3/2}$ and $\pi 2s_{1/2}^{-1} \otimes \nu 2p_{1/2}$.

TABLE VII: Experimental magnetic moments (in units of μ_N) for even- A K isotopes compared to shell-model predictions using two effective interactions: SDPF-NR and SDPF-U. The error in the square brackets is due to the hyperfine structure anomaly, which amounts to 0.5%.

Isotope	I^π	μ_{exp}	$\mu_{\text{SDPF-NR}}$	$\mu_{\text{SDPF-U}}$	μ_{lit}	Reference
^{38}K	3^+	+1.3711 (10) [69]	+1.33	+1.33	+1.371 (6) ^a	[32]
^{40}K	4^-	—	-1.63	-1.63	-1.2964 (4) ^b	[39]
^{42}K	2^-	-1.1388 (7) [57]	-1.58	-1.56	-1.14087 (20) ^b	[34]
^{44}K	2^-	-0.8567 (9) [43]	-1.05	-0.90	-0.856 (4) ^a	[32]
^{46}K	2^-	-1.0464 (7) [52]	-1.21	-1.18	-1.051 (6) ^a	[32]
^{48}K	1^-	-0.8997 (3) [45]	-0.77	-0.55	—	-

^aIncluded 0.5% uncertainty on the error to account for the hyperfine structure anomaly.

^bThe value without diamagnetic correction of +0.13%.

The experimental magnetic moments together with shell-model calculations are summarized in Table VII and graphically presented in Fig. 8. The predictions for ^{38}K from both interactions reproduce the experimental magnetic moments very well. Furthermore, almost the same value is calculated with both interactions for $A = 40$ and $A = 42$, but the experimental results are underestimated by about 26% and 37% for ^{40}K and ^{42}K , respectively. While the SDPF-U interaction almost reproduces the observed magnetic moment for ^{44}K , its earlier version (SDPF-NR) shows a deviation of approximately $0.26 \mu_N$ when comparing to the experimental result. Additionally, very good agreement is observed between experimental and theoretical results for ^{46}K . Finally, the situation is inverted for the case with the strongly mixed ^{48}K , which is better reproduced by the SDPF-NR interaction and shows a deviation of about $0.35 \mu_N$ for SDPF-U. The general trend of the magnetic moments is well reproduced by both interactions and the calculated magnetic moments are in reasonable agreement with the experimental results. The slightly larger deviation observed for ^{40}K and ^{42}K is probably due to lack of excitations across $Z, N = 20$.

At this point one should be aware that the odd-odd isotopes are more challenging for the shell-model calculation than odd-even nuclei due to the high level density at low energy. These levels arise from all different possibilities of couplings between an odd proton and an odd neutron. Although the energy of a calculated level might be wrong by hundreds of keV,

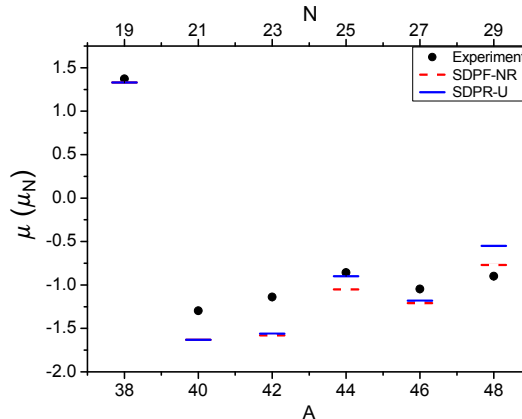


FIG. 8: (color online) Measured magnetic moments (black dots) for even- A K isotopes compared to the shell-model calculations using the SDPF-NR (red dashed line) as well as the SDPF-U (blue solid line) effective interaction. Although there is a larger deviation present for ^{40}K and ^{42}K , which might originate from lack of the excitations across $Z, N = 20$, overall reasonable agreement between the experimental and theoretical results is observed.

if the magnetic moment is well reproduced we can still draw reliable conclusions on the wave function composition of the state.

In the case of ^{38}K , the $\pi 1d_{3/2}^{-1} \otimes \nu 1d_{3/2}^{-1}$ configuration constitutes more than 90% of the total wave function. The dominant component of the ground-state wave function for all $N > 20$ even- A K isotopes is arising from a hole in the $\pi 1d_{3/2}$ coupled to an odd neutron in the pf orbital. For $^{40,42,44,46}\text{K}$, the main component is $\pi 1d_{3/2}^{-1} \otimes \nu 1f_{7/2}^n$ and its contribution to the wave function decreases from more than 90% down to about 85%. The lowest 1^- state in ^{48}K is predicted to be an excited state by both interactions respectively at $E = 407\text{ keV}$ and $E = 395\text{ keV}$ (see Fig. 9).

Both interactions favor a 2^- state as the ground state. In addition, an excited 2^- state is near-degenerate with the 1^- level, at $E = 408\text{ keV}$ and $E = 340\text{ keV}$, respectively. Considering the firmly assigned ground-state spin-parity of ^{48}K , and using the multipolarities deduced from the measured lifetimes of the lowest four levels by Królas *et al.* [15], the experimental spin-parities of the four lowest excited states can now be more firmly assigned. A reasonable agreement with the calculated level scheme is shown up to 1 MeV. However,

the positive parity level around 2 MeV, which must be due to a proton excitation across the $Z = 20$ gap, is not reproduced in the current calculations, as such excitations have not been included.

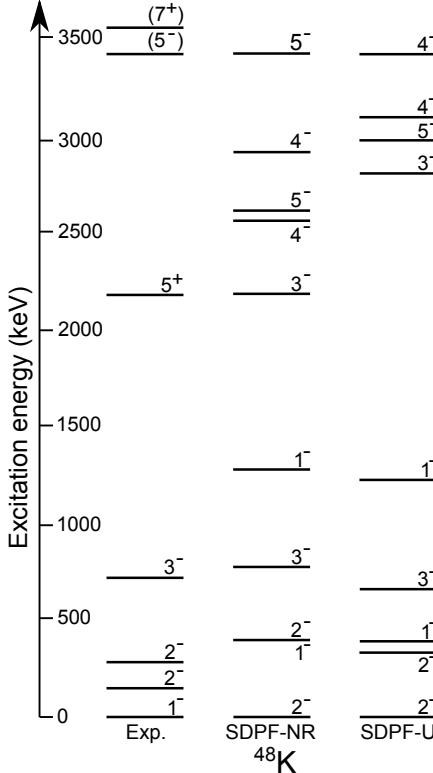


FIG. 9: Experimental energy spectrum of ^{48}K adapted from Ref. [15] using the fact that the nuclear spin is firmly established to be 1^- [26]. Results are compared to the calculated spectra from different effective interactions: SDPF-NR and SDPF-U.

The wave function of the calculated lowest 1^- state, which reproduces the observed magnetic moment reasonably well, is very fragmented compared to the other even- A K isotopes: $\pi 1d_{3/2}^{-1} \otimes \nu 2p_{3/2}$ only constitutes approximately 40% and 50% of the total wave function for SDPF-NR and SDPF-U, respectively. The next leading component, $\pi 2s_{1/2}^{-1} \otimes \nu 2p_{3/2}$, contributes only 15-20%, although this isotope is located between two isotopes with a dominant $\pi 2s_{1/2}^{-1}$ configuration (^{47}K and ^{49}K). In addition, configurations which arise from

$1p1h$ excitation from $\nu 1f_{7/2}$ to the rest of the $\nu(pf)$ shell have a significant contribution of about 15% to the total wave function of the lowest 1^- state in ^{48}K . In the case of ^{50}K , the wave function of the 0^- level is much less fragmented: the main component is $\pi 1d_{3/2}^{-1} \otimes \nu(pf)$, constituting more than 85% of the wave function. The contribution of the $\pi 2s_{1/2}^{-1} \otimes \nu(pf)$ component as well as the one from $1p1h$ neutron excitations is about 5%. While this 0^- is correctly reproduced as the ground state by the SDPF-U interaction, it is predicted at 315 keV (with a 2^- ground state) with SDPF-NR.

In addition to the magnetic moment and wave functions obtained from the shell-model calculations, it is also possible to extract information about the occupancy of the orbitals. The calculated occupancy of the $\pi 2s_{1/2}$ and $\pi 1d_{3/2}$ orbitals are shown in Fig. 10.

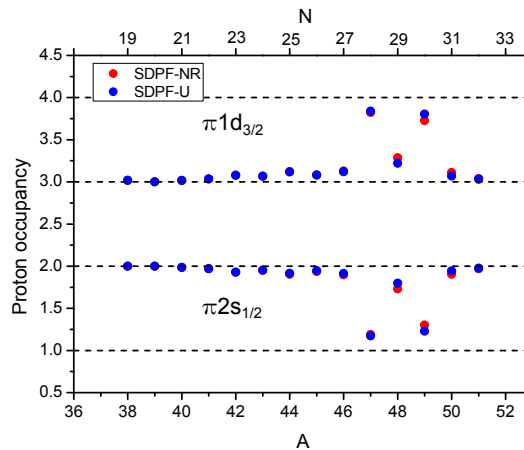


FIG. 10: (Color online) Proton occupation of the $\pi 2s_{1/2}$ and the $\pi 1d_{3/2}$ orbitals from the shell-model calculations using the SDPF-NR and SDPF-U effective interactions. It is clear that for isotopes from $A = 38 - 46$ and $A = 48, 50 - 51$ the dominant component in the configuration is a hole in the $\pi 1d_{3/2}$. In the case of $I^\pi = 1/2^+$ isotopes, a proton hole is located in the $2s_{1/2}$. Deviation from integer numbers for $^{47-49}\text{K}$ indicates mixing in the wave function.

The maximum number of particles found in an orbital with total angular momentum j is $2j + 1$. Thus, for the $s_{1/2}$ this number is 2, while in case of the $d_{3/2}$ it is 4. The occupation of the $\pi 2s_{1/2}$ remains almost constant around two protons from $N = 19$ up to $N = 27$, with a slight decrease toward ^{46}K . For these isotopes, the occupation of the $\pi 1d_{3/2}$ stays around three protons with a corresponding slight increase toward $A = 46$. This increase

(decrease) of occupancy for the $\pi 1d_{3/2}$ ($\pi 2s_{1/2}$) orbital is probably due to the reduction of the energy difference between these two proton orbitals with increasing number of neutrons in the $\nu 1f_{7/2}$. Additionally, a small odd-even staggering in the proton occupation is also observed for these isotopes. This effect could be due to the proton-neutron coupling for the odd-odd isotopes, which results in a higher occupancy of $\pi 1d_{3/2}$ and a lower occupancy for the $\pi 2s_{1/2}$. In this region, there is no discrepancy observed between results from the different interactions. Furthermore, almost degenerate proton orbitals for $N = 28$ yield a hole in the $\pi 2s_{1/2}$ causing the $\pi 1d_{3/2}$ to be nearly completely filled. Surprisingly, for ^{48}K with an additional unpaired neutron in the $\nu 2p_{3/2}$ orbital, the proton occupation of $\pi 1d_{3/2}$ drops down to about 3.3 protons while the $\pi 2s_{1/2}$ occupation increases accordingly. For the next isotope with two neutrons placed in the $\nu 2p_{3/2}$ (^{49}K), the occupation of the proton orbitals is more similar to ^{47}K , where a hole in the $\pi 2s_{1/2}$ is found. This is also in agreement with the nuclear spins and magnetic moments of these two isotopes. At this point a larger deviation from integer numbers for the proton occupation indicates a larger amount of mixing in the configurations of $^{47-49}\text{K}$. Based on the information obtained from the g factor and magnetic moment for ^{48}K , a hole in the $\pi d_{3/2}$ was expected to be the dominant component, which is confirmed by these occupancies. Nevertheless, the reason for the big decrease of the $\pi 1d_{3/2}$ occupancy compared to the neighboring two isotopes is still puzzling. Adding one and two more neutrons leads to the "normal" occupation for the neutron-rich K isotopes with the filled $\pi 2s_{1/2}$ and a hole in the $\pi 1d_{3/2}$.

V. SUMMARY

Hyperfine spectra of potassium isotopes between $N = 19$ and $N = 32$ were measured using collinear laser spectroscopy, yielding the nuclear spins and magnetic moments. The experimental results were compared to shell-model calculations using two different effective interactions: SDPF-NR and SDPF-U. Overall good agreement is observed between the measured magnetic moments and theoretical predictions. This allows one to draw conclusions on the composition of the wave function as well as on the proton occupation of the $2s_{1/2}$ and $1d_{3/2}$ orbitals. It was shown that the dominant component of the ground-state wave function for odd- A isotopes up to ^{45}K arises from a hole in the $\pi 1d_{3/2}$. Additionally, for isotopes with spin $1/2^+$ the main component of the wave function is $\pi 2s_{1/2}^{-1}$ with more mix-

ing present in ^{49}K coming from the almost degenerate $\pi 2s_{1/2}$ and $\pi 1d_{3/2}$ proton orbitals. The nuclear spin of ^{51}K , which was found to be 3/2, points to the "normal" ordering of the EPSE, and this is confirmed by the measured magnetic moment that is close to the $\pi 1d_{3/2}$ single particle value. In the case of odd-odd isotopes, the main configuration originates from the coupling of the $\pi 1d_{3/2}^{-1} \otimes \nu(pf)$, and this for all odd-odd isotopes from $N = 19$ up to $N = 31$. Only for ^{48}K , a very fragmented wave function has been observed for the 1^- ground state. This level becomes the ground state due to a significant (>20%) contribution from the $\pi 2s_{1/2}^{-1} \otimes \nu(pf)$ configuration. Moreover, a detailed discussion about the evolution of the proton effective single particle energies (ESPEs) was presented. The central term of the monopole interaction was found to have the strongest effect in the changing ESPE beyond $N = 28$. *Ab initio* calculations of the ESPEs show a considerable decrease (70%) of the gap between $\pi(1d_{3/2}-2s_{1/2})$ at $N = 28$ presenting a promising starting point for the approach which is currently still under development.

The experimental results of the neutron-rich potassium isotopes have a relevant role in the future improvements of the effective shell-model interactions and *ab initio* calculations. Additional experimental data for ^{51}K and ^{53}K , in particular the spin of the ^{53}K ground state and the energy of the $I = 1/2^+$ states, could provide the final clues about the evolution of the proton *sd* levels in this region.

Acknowledgments

The authors are grateful to F. Nowacki for providing the effective interactions which were used in the shell-model calculations. C.B., T.D. and V.S. would like to thank A. Cipollone and P. Navrátil for their collaboration on $3N$ forces. This work was supported by the IAP-project P7/12, the FWO-Vlaanderen, GOA 10/010 from KU Leuven, NSF grant no. PHY-1068217, BMBF (05 P12 RDCIC), Max-Planck Society, EU FP7 via ENSAR (no. 262010) and STFC grant No. ST/L005743/1. Gorkov-Green's function calculations were performed using HPC resources from GENCI-CCRT (Grant No. 2014-050707) and the DiRAC Data Analytic system at the University of Cambridge (BIS National E-infrastructure Capital Grant No. ST/K001590/1 and STFC Grants No. ST/H008861/1, ST/H00887X/1, and ST/K00333X/1). We would like to thank to the ISOLDE technical group for their

support and assistance.

- [1] M. Goeppert Mayer, Phys. Rev. **75**, 1969 (1949).
- [2] O. Haxel, J. Jensen, and H. Suess, Phys. Rev. **75**, 1766 (1949).
- [3] R. Krücken, Contemp. Phys. **52**, 101 (2011).
- [4] O. Sorlin and M.-G. Porquet, Prog. Part. Nucl. Phys. **61**, 602 (2008).
- [5] F. Wienholtz, D. Beck, K. Blaum, Ch. Borgmann, M. Breitenfeldt, R. B. Cakirli, S. George, F. Herfurth, J. D. Holt, M. Kowalska, et al., Nature **498**, 346 (2013).
- [6] K. Blaum, J. Dilling, and W. Nörtershäuser, Phys. Scr. **T152**, 014017 (2013).
- [7] P. Van Duppen and K. Riisager, Journal of Physics G: Nuclear and Particle Physics **38**, 024005 (2011).
- [8] K. Heyde, Phys. Scr. **T152**, 014006 (2013).
- [9] O. Sorlin and M.-G. Porquet, Phys. Scr. **T152**, 014003 (2013).
- [10] A. Gade, B. A. Brown, D. Bazin, C. M. Campbell, J. A. Church, D. C. Dinca, J. Enders, T. Glasmacher, M. Horoi, Z. Hu, et al., Phys. Rev. C **74**, 034322 (2006).
- [11] N. A. Smirnova, K. Heyde, B. Bally, F. Nowacki, and K. Sieja, Phys. Rev. C **86**, 034314 (2012).
- [12] T. Otsuka, T. Suzuki, R. Fujimoto, H. Grawe, and Y. Akaishi, Phys. Rev. Lett. **95**, 232502 (2005).
- [13] N. A. Smirnova, B. Bally, K. Heyde, F. Nowacki, and K. Sieja, Phys. Lett. B **686**, 109 (2010).
- [14] T. Otsuka, T. Suzuki, M. Honma, Y. Utsuno, N. Tsunoda, K. Tsukiyama, and M. Hjorth-Jensen, Phys. Rev. Lett. **104**, 012501 (2010).
- [15] W. Królas, R. Broda, B. Fornal, R. V. F. Janssens, A. Gadea, S. Lunardi, J. J. Valiente-Dobon, D. Mengoni, N. Mărginean, L. Corradi, et al., Phys. Rev. C **84**, 064301 (2011).
- [16] R. Broda, J. Wrzesiński, A. Gadea, N. Mărginean, B. Fornal, L. Corradi, A. M. Stefanini, W. Królas, T. Pawłat, B. Szpak, et al., Phys. Rev. C **82**, 034319 (2010), URL <http://link.aps.org/doi/10.1103/PhysRevC.82.034319>.
- [17] L. Gaudefroy, Phys. Rev. C **81**, 064329 (2010).
- [18] P. Baumann, M. Bounajma, F. Didierjean, A. Huck, A. Knipper, M. Ramdhane, G. Walter, G. Marguier, C. Richard-Serre, and B. A. Brown, Phys. Rev. C **58**, 1970 (1998).
- [19] H. L. Crawford, R. V. F. Janssens, P. F. Mantica, J. S. Berryman, R. Broda, M. P. Carpenter,

- B. Fornal, G. F. Grinyer, N. Hoteling, B. Kay, et al., *Acta Physica Polonica B* **40**, 481 (2009).
- [20] L. C. Carraz, P. G. Hansen, A. Huck, B. Jonson, G. Klotz, A. Knipper, K. L. Kratz, C. Miéhé, S. Mattsson, G. Nyman, et al., *Physics Letters B* **109**, 419 (1982), ISSN 0370-2693, URL <http://www.sciencedirect.com/science/article/pii/0370269382911042>.
- [21] F. Perrot, F. Maréchal, C. Jollet, P. Dessagne, J.-C. Angélique, G. Ban, P. Baumann, F. Benrachi, U. Bergmann, C. Borcea, et al., *Phys. Rev. C* **74**, 014313 (2006).
- [22] J. Papuga, M. L. Bissell, K. Kreim, K. Blaum, B. A. Brown, M. De Rydt, R. F. Garcia Ruiz, H. Heylen, M. Kowalska, R. Neugart, et al., *Phys. Rev. Lett.* **110**, 172503 (2013).
- [23] D. F. Measday and T. J. Stocki, *Phys. Rev. C* **73**, 045501 (2006).
- [24] A. Huck, G. Klotz, A. Knipper, C. Miéhé, G. Walter, and C. Richard-Serre, *Phys. Rev. C* **21**, 712 (1980).
- [25] L. Weissman, O. Arnd, U. Bergmann, A. Brown, R. Catherall, J. Cederkall, I. Dillmann, O. Hallmann, L. Fraile, S. Franchoo, et al., *Phys. Rev. C* **70**, 024304 (2004).
- [26] K. Kreim, M. L. Bissell, J. Papuga, K. Blaum, M. De Rydt, R. F. Garcia Ruiz, S. Goriely, H. Heylen, M. Kowalska, R. Neugart, et al., *Physics Letters B* **731**, 97 (2014).
- [27] A. C. Mueller, F. Buchinger, W. Klempert, E. Otten, R. Neugart, C. Ekström, and J. Heine-meyer, *Nucl. Phys. A* **403**, 234 (1983).
- [28] H. Frånberg, P. Delahaye, J. Billowes, K. Blaum, R. Catherall, F. Duval, O. Gianfrancesco, T. Giles, A. Jokinen, M. Lindroos, et al., *Nucl. Instrum. Methods Phys. Res. B* **266**, 4502 (2008).
- [29] P. Vingerhoets, K. T. Flanagan, M. Avgoulea, J. Billowes, M. L. Bissell, K. Blaum, B. A. Brown, B. Cheal, M. De Rydt, D. H. Forest, et al., *Phys. Rev. C* **82**, 064311 (2010).
- [30] M. Wang, G. Audi, A. H. Wapstra, F. G. Kondev, M. MacCormick, X. Xu, and B. Pfeiffer, *Chinese Physics C* **36**, 1603 (2012).
- [31] F. James, *MINUIT - Function Minimization and Error Analysis; CERN* (1994).
- [32] F. Touchard, P. Guimbal, S. Büttgenbach, R. Klapisch, M. De Saint Simon, J. M. Serre, C. Thibault, H. T. Duong, P. Juncar, S. Liberman, et al., *Phys. Lett. B* **108**, 169 (1982).
- [33] E. A. Phillips, O. Ames, and S. S. Glickstein, *Phys. Rev.* **138**, 773 (1965).
- [34] Y. W. Chan, V. W. Cohen, and H. B. Silsbee, *Phys. Rev.* **184**, 1102 (1969).
- [35] A. Beckmann, K. D. Böklen, and D. Elke, *Z. Phys. A* **270**, 173 (1974), ISSN 0939-7922, URL <http://dx.doi.org/10.1007/BF01680407>.

- [36] A. Bohr, Phys. Rev. **81**, 331 (1951).
- [37] A. Bohr and V. F. Weisskopf, Phys. Rev. **77**, 94 (1950).
- [38] J. E. Rosenthal and G. Breit, Phys. Rev. **41**, 459 (1932).
- [39] J. T. Eisinger, B. Bederson, and B. T. Feld, Phys. Rev. **86**, 73 (1952).
- [40] S. A. Ochs, R. A. Logan, and P. Kusch, Phys. Rev. **78**, 184 (1950).
- [41] V. J. Ehlers, Y. Kabasakal, H. A. Shugart, and O. Tezer, Phys. Rev. **176**, 25 (1968).
- [42] S. Falke, E. Tiemann, C. Lisdat, H. Schnatz, and G. Grosche, Phys. Rev. A **74**, 032503 (2006).
- [43] F. Nowacki and E. Caurier, Acta Physica Polonica B **30**, 705 (1999).
- [44] J. Retamosa, E. Caurier, F. Nowacki, and A. Poves, Phys. Rev. C **55**, 1266 (1997).
- [45] S. Nummela, P. Baumann, E. Caurier, P. Dessagne, A. Jokinen, A. Knipper, G. Le Scornet, C. Miché, F. Nowacki, M. Oinonen, et al., Phys. Rev. C **63**, 044316 (2001).
- [46] F. Nowacki and A. Poves, Phys. Rev. C **79**, 014310 (2009), URL <http://link.aps.org/doi/10.1103/PhysRevC.79.014310>.
- [47] W. A. Richter, S. Mkhize, and B. A. Brown, Phys. Rev. C **78**, 064302 (2008).
- [48] G. Neyens, J. Phys.: Conf. Series **445**, 012007 (2013).
- [49] A. Poves and A. P. Zuker, Phys. Rep. **70**, 235 (1981).
- [50] V. Somà, A. Cipollone, C. Barbieri, P. Navrátil, and T. Duguet, Phys. Rev. C **89**, 061301(R) (2014).
- [51] V. Somà, T. Duguet, and C. Barbieri, Phys. Rev. C **84**, 064317 (2011).
- [52] D. R. Entem and R. Machleidt, Phys. Rev. C **68**, 041001(R) (2003).
- [53] R. Machleidt and D. R. Entem, Phys. Rep. **503**, 1 (2011).
- [54] P. Navrátil, Few-Body Systems **41**, 117 (2007).
- [55] H. M. Schwartz, Phys. Rev. **89**, 1293 (1953).
- [56] T. Minamisono, J. W. Hugg, D. G. Mavis, T. K. Saylor, H. F. Glavish, and S. S. Hanna, Phys. Lett. B **61**, 155 (1976).
- [57] A. Andl, K. Bekk, S. Göring, A. Hanser, G. Nowicki, H. Rebel, G. Schatz, and R. C. Thompson, Phys. Rev. C **26**, 2194 (1982).
- [58] L. Olschewski, Z. Physik **249**, 205 (1972).
- [59] R. F. Garcia Ruiz, in preparation.

Chapter 5

Isomer shift in ^{38}K

This chapter is dedicated to our measurement of the isomer shift in ^{38}K . This is the first direct observation of this isomer shift, and it contradicts the conclusions from an earlier indirect measurement published in [32]. The results are published in Physics Review Letters and will be presented in the form of an article.

5.1 Article III

The observed isomer shift in ^{38}K yielded a significant difference in the mean square charge radius between the isomeric state ($I^\pi = 0^+$) and the ground state ($I^\pi = 3^+$). This effect can be explained by scattering of $\pi\nu$ pairs into the pf orbits. Shell-model calculations using interactions where proton and neutron excitations were included across the $Z = N = 20$ energy gap confirmed this explanation.

My contribution to the article is in the analysis which was carried out in parallel with the main author of this article. In addition, I performed preliminary shell-model calculations which were finally not included due to unsuitable interactions. I was also involved in drafting the manuscript.

Physical Review Letter 113, 052502 (2014)

**Proton-Neutron Pairing Correlations in the Self-Conjugate
Nucleus ^{38}K Probed via a Direct Measurement of the Isomer
Shift**

M. L. Bissell,^{1,*} J. Papuga,¹ H. Naïdja,^{2,3,4} K. Kreim,⁵ K. Blaum,⁵

M. De Rydt,¹ R. F. Garcia Ruiz,¹ H. Heylen,¹ M. Kowalska,⁶

R. Neugart,^{5,7} G. Neyens,¹ W. Nörtershäuser,^{7,8} F. Nowacki,²

M. M. Rajabali,¹ R. Sanchez,^{3,9} K. Sieja,² and D. T. Yordanov⁵

¹*KU Leuven, Instituut voor Kern- en Stralingsfysica, B-3001 Leuven, Belgium*

²*Université de Strasbourg, IPHC, 23 rue du Loess 67037 Strasbourg,*

France CNRS, UMR7178, 67037 Strasbourg, France

³*GSI Helmholtzzentrum für Schwerionenforschung, D-64291 Darmstadt, Germany*

⁴*Laboratoire de Physique Mathématique et Subatomique,*

Constantine 1 University, Constantine 25000, Algeria

⁵*Max-Plank-Institut für Kernphysik, D-69117 Heidelberg, Germany*

⁶*Physics Department, CERN, CH-1211 Geneva 23, Switzerland*

⁷*Institut für Kernchemie, Johannes*

Gutenberg-Universität Mainz, D-55128 Mainz, Germany

⁸*Institut für Kernphysik, TU Darmstadt, D-64289 Darmstadt, Germany*

⁹*Helmholtz-Institut Mainz, Johannes*

Gutenberg-Universität Mainz, 55099 Mainz, Germany

(Dated: March 16, 2015)

Abstract

A marked difference in the nuclear charge radius was observed between the $I^\pi = 3^+$ ground state and the $I^\pi = 0^+$ isomer of ^{38}K and is qualitatively explained using an intuitive picture of proton-neutron pairing. In a high-precision measurement of the isomer shift using bunched-beam collinear laser spectroscopy at CERN-ISOLDE, a change in the mean-square charge radius of $\langle r_c^2 \rangle(^{38}\text{K}^m) - \langle r_c^2 \rangle(^{38}\text{K}^g) = 0.100(6) \text{ fm}^2$ was obtained. This is an order of magnitude more accurate than the result of a previous indirect measurement from which it was concluded that both long-lived states in ^{38}K have similar charge radii. Our observation leads to a substantially different understanding since the difference in charge radius is, moreover, opposite in sign to previously reported theoretical predictions. It is demonstrated that the observed isomer shift can be reproduced by large-scale shell-model calculations including proton and neutron excitations across the $N, Z = 20$ shell gaps, confirming the significance of cross-shell correlations in the region of ^{40}Ca .

Since the early days of nuclear physics, it has been known that protons and neutrons favor the formation of $I = 0$ pairs with antialigned spins. In 1935, the first parametrisation of the Bethe-Weizsäcker mass formula [1] included a term that took $\pi\pi$ and $\nu\nu$ pairs into account by enhancing the binding in even-even nuclei. Only one year later an analysis of nucleon-nucleon scattering data demonstrated that within experimental errors the strong interaction between nucleons can be considered charge independent [2]. This discovery led directly to the application [3] of Heisenberg's concept of "isotopic spin" (isospin) to finite nuclei. As a direct consequence $\pi\nu$ pairs with $T = 1$, $T_z = 0$ should be treated on an equal footing to the $T = 1$ $\pi\pi$ and $\nu\nu$ pairs with $T_z = +1, -1$, respectively. While this charge independent treatment of isovector pairing remains a standard feature of modern shell model calculations and is under development in mean-field approaches [4, 5], the experimental investigation of the $\pi\nu$ pairing interaction remains an active area of interest [6, 7]. Specifically, theoretical debate [8–11] on the role of $\pi\nu$ pairing in the microscopic origins of the nuclear symmetry energy has wide ranging consequences not only for nuclear structure, but also nuclear astrophysics [12–14]. Consequently, an experimental constraint on the strength of isovector pairing correlations is vital. Here, we demonstrate that, when $\pi\nu$ pairing correlations are considered on an equal footing to $\pi\pi$ and $\nu\nu$ correlations, then the increase in mean square charge radius of $^{38}\text{K}^m$ can be successfully described. Furthermore, the isomer shift is shown to provide a highly sensitive test of the strength of isovector pairing employed in modern nuclear structure calculations.

The setup for collinear laser spectroscopy [15], located at CERN-ISOLDE, was used to obtain the hyperfine spectra (hfs) of $^{38,39,42,44,46-51}\text{K}$ isotopes. During the experiment, protons bombarded a UC_x target producing a wide range of radioactive nuclei. The ions of interest were cooled and bunched in a helium filled radio-frequency quadrupole ISCOOL [16] after mass separation by the high-resolution mass separator. These ions were then neutralized in a potassium-filled charge exchange cell (CEC) located in front of the detection region and resonant excitation of the $4s\ ^2S_{1/2} \rightarrow 4p\ ^2P_{1/2}$ atomic transition was obtained using a cw Ti:sapphire laser. With the laser frequency kept constant, Doppler tuning of the ions was performed by applying an additional voltage to the CEC. The background from scattered light was reduced by only accepting signals from the detectors (four photomultiplier tubes) when bunches of K atoms arrived in the detection region. More detailed descriptions of the experimental setup may be found in Papuga et al. [17] and Kreim et al. [18] reporting, respectively, on spins and magnetic moments

of $^{49,51}\text{K}$ and charge radii of the K isotopes between $N = 27$ and $N = 32$.

Here, we focus only on the discussion of the isomer shift between the two observed states in ^{38}K . As the mass difference between the two states is small, systematic uncertainties on the kinematic shift arising from an imperfect knowledge of the ion beam energy [19] are negligible. An example frequency spectrum containing both the ground state and isomer of ^{38}K is presented in Fig. 1. Simultaneous fitting of the four $^{38}\text{K}^g$ hfs components and the single $^{38}\text{K}^m$ component was performed using a χ^2 minimization procedure. The fitting employed asymmetric line shapes associated with collisional ion energy loss [20] and the relative positions of the $^{38}\text{K}^g$ components to the hfs centroid were constrained by the usual relations [21].

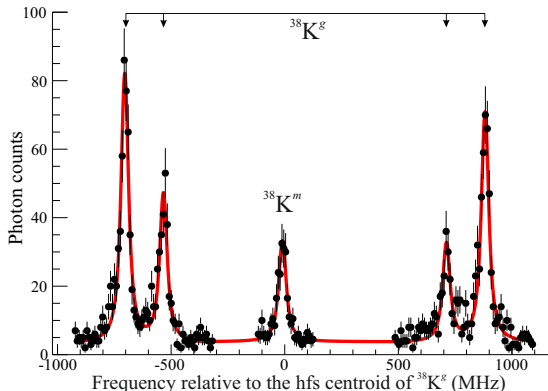


FIG. 1: (color online) Observed hyperfine spectra of $^{38}\text{K}^{g,m}$. Four peaks are obtained for $I = 3$ (ground state) and only one for $I = 0$ (isomer).

The difference in hyperfine structure centroid of two isotopes or nuclear states $\delta\nu^{A,A'} = \nu^{A'} - \nu^A$ may be related to the difference in mean square charge radii $\delta\langle r_c^2 \rangle^{A,A'} = \langle r_c^2 \rangle^{A'} - \langle r_c^2 \rangle^A$ via

$$\delta\langle r_c^2 \rangle^{A,A'} = \frac{1}{F}(\delta\nu^{A,A'} - K_{\text{MS}} \frac{m_{A'} - m_A}{m_{A'} m_A}) \quad (1)$$

where m_A and $m_{A'}$ are the masses of relevant isotopes or nuclear states taken from Wang et al. [22]. K_{MS} is the total mass shift factor given by the sum $K_{\text{MS}} = K_{\text{SMS}} + K_{\text{NMS}}$, in which the specific mass shift $K_{\text{SMS}} = -15.4(38)$ GHz u from Martensson-Pendrill et al. [23] and the normal mass shift $K_{\text{NMS}} = \nu^A m_e = 213.55$ GHz u. The electronic factor $F = -110(3)$ MHz fm $^{-2}$ was also taken from reference [23].

Behr *te al.* [24] measured the isotope shift $\delta\nu^{38m,39}$ and combined this with $\delta\nu^{38g,39}$ measured by Touchard *te al.* [25]. From this approach, they found that, within errors,

the ground and isomeric state had the same charge radii. In Table I excellent agreement can be seen between the $^{38m,39}\text{K}$ isotope shift measured in this work and that of Behr et al. and agreement within errors between our $^{38g,39}\text{K}$ isotope shift and that of Touchard et al.. It is only possible to conclude that the cumulative effect of the relatively large uncertainties in [24] and [25] led to the conclusion that the ground state and isomer are of the same size. Here the advantages of performing a direct isomer shift measurement are most clearly visible.

TABLE I: Isomer and isotope shifts determined in this work compared with literature values. The second uncertainty contained within the square brackets corresponds to the systematic contribution associated with the atomic parameters K_{SMS} and F .

A'	A	$\delta\nu^{A,A'} \text{ (MHz)}$	$\delta\langle r_c^2 \rangle^{A,A'} \text{ (fm}^2)$	Reference
38g	39	-123.4 (10)	-0.089 (9)[23]	This work
		-127.0 (53)	-0.057 (48)[23]	[25]
38m	39	-134.5 (11)	0.011 (10)[23]	This work
		-132 (3)	-0.02 (3)[2] ^a	[24]
38m	38g	-11.03 (56)	0.100 (5)[3]	This work
		-4 (6)	0.04 (6)	[24, 25]

^aMeasured in the $4s^2S_{1/2} \rightarrow 4p^2P_{3/2}$ transition assuming the same F and K_{SMS} as in the $4s^2S_{1/2} \rightarrow 4p^2P_{1/2}$ transition.

The authors of [24] also performed a detailed calculation of the difference in charge radius of the two states. Their Hartree-Fock calculation constrained by shell model orbital occupancies concluded that the ground state should be larger than the isomer by 0.014 fm^2 . This evaluation clearly contradicts the measurement reported in this work in both magnitude and sign.

To develop an understanding of the origins of the difference in size of these two nuclear states, we begin by comparing with the $\delta\langle r_c^2 \rangle^{38g,A'}$ of neighboring nuclei in Fig. 2. Clearly, the increase in size of the isomeric state is larger than the normal ground-state odd-even staggering by about a factor of 2. An alternative view of this effect can be obtained by plotting the differences in charge radii as a function of A along the line of $N = Z$. The results of this process are shown in Fig. 3. Here, it is seen that the larger charge radius of the isomer is consistent with a smooth increase in size along the $N = Z$ line, while the ground state is somewhat smaller than the average of its two neighbors.

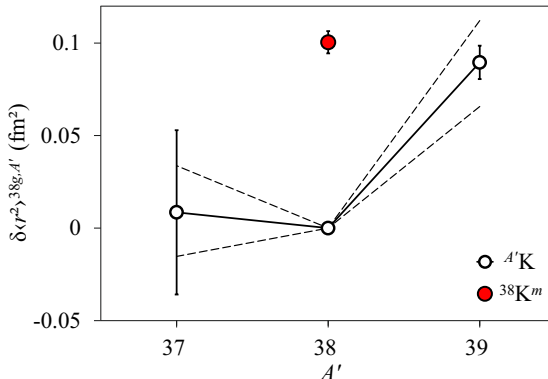


FIG. 2: (color online) Changes in mean square charge radius referenced to ${}^{38}\text{K}$. The systematic uncertainty related to the atomic specific mass shift is represented by the two dotted lines. Datum for ${}^{37}\text{K}$ taken from [24].

To interpret these observations one may begin by considering the origins of the ubiquitous normal odd-even staggering (OES) in nuclear charge radii [26–28]. This phenomenon may be readily explained by considering $\pi\pi$ or $\nu\nu$ $I = 0$ pairs scattering to a large number of states near the Fermi surface in the even N or Z nuclei. The addition of an odd proton or neutron “blocks” a specific orbit, thus, reducing the scattering of pairs. As less bound orbitals naturally have a larger spacial extent, $\langle r_c^2 \rangle$ of odd N or Z nuclei are consistently found to be smaller than the average of their even neighbors. In the case of isotopic OES, an increase in neutron orbital correlations translates into a change in charge radius either by a global broadening of the proton distribution in mean-field calculations or via a direct enhancement of the scattering of valence $\pi\pi$ pairs. Although such pairing arguments are typically employed when considering pairs of protons or neutrons, charge independence of the nucleon-nucleon interaction effectively results in the possibility of $\pi\nu$ pairing correlations. Indeed, in ${}^{38}\text{K}$, it would appear that, for the $T = 1$ isomer, the $\pi\nu$ pair coupled to $I = 0$ is free to scatter into a range of orbitals. Conversely, the $\pi\nu$ pair making up the $T = 0$, $I^\pi = 3^+$ ground state is heavily restricted in the number of states with which it can mix, significantly reducing the proton occupancy in the fp shell.

In this blocking picture, it is readily apparent that the isomer shift should be larger than the normal isotopic OES. As the even N ${}^{37,39}\text{K}$ isotopes have proton distributions which remain blocked by the single $\pi d_{3/2}^{-1}$, the scale of the OES remains somewhat smaller than in the neighboring even Z isotopic chains. The formation of an $I = 0$ $\pi\nu$ pair in ${}^{38}\text{K}^m$ effectively removes this blocking, thus, enhancing the πfp occupancy. Under the

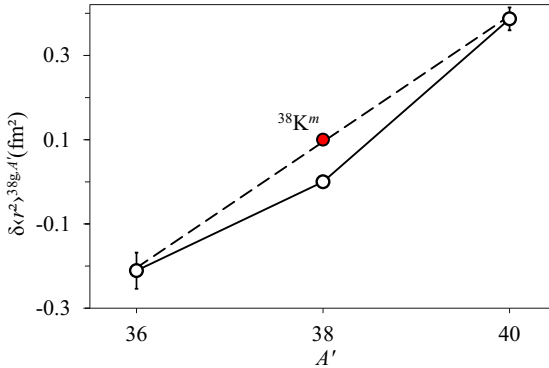


FIG. 3: (color online) Changes in mean square charge radii between the self-conjugate nuclei ^{36}Ar , ^{38}K , and ^{40}Ca from this work and [29].

assumption of charge independence, this $\pi\nu$ pair should be free to scatter on an equal basis to $\pi\pi$, $\nu\nu$ pairs removing the OES along the line of $N = Z$. Precisely this behavior is observed in the experimental $\delta\langle r_c^2 \rangle^{A,A'}$ presented in Fig. 3.

As the observed radii differences can be understood with a simple intuitive model, it remains to investigate how the previous detailed theoretical calculation failed to predict both the sign and magnitude of the isomer shift. It was shown by Caurier *et al.* [27] that the isotope shifts in Ca could be reproduced with a reasonable accuracy if one calculates the occupancy of the πfp shell as a function of A . In this work, the expression

$$\delta\langle r_c^2 \rangle^{A,A'} = \frac{1}{Z} \Delta n_{fp}^\pi(A, A') b^2 \quad (2)$$

was used, where b is the oscillator parameter and n_{fp}^π refers to the number of protons lifted across the $Z = 20$ shell closure. The choice of oscillator parameter b remains a subject of much interest. While a number of approaches exist within the literature [30–33], it should be noted that all produce values of b within a few percent of each other. In the following, we assume $b^2(^{38}\text{K}) = 3.944 \text{ fm}^2$ as determined by the equation of Duflo and Zuker [32]. With this value and Eq. (2) it is immediately obvious that, for a successful reproduction of the isomer shift, one would require the isomer to have an average πfp orbital occupancy, n_{fp}^π , of the order of 0.48 protons larger than the corresponding ground state occupancy.

To test the validity of this conclusion shell model calculations were performed in the model space comprising $1s_{1/2}$, $1d_{3/2}$, $0f_{7/2}$, $1p_{3/2}$ orbitals for neutrons and protons, with the ZBM2 interaction from Ref. [27]. Full space diagonalization in this model space has been achieved using the shell model code ANTOINE [34]. The results of the calculations are

reported in Table II, where the summed pf -shell proton occupancies are listed for ground and isomeric states along with the corresponding $\delta \langle r^2 \rangle^{38g,38m}$ obtained from Eq. (2). As can be seen, the ZBM2 interaction gives a fair agreement with the experimental value, supporting the realistic character of the wave functions obtained. However, as demonstrated in Fig. 4, it fails to produce a correct order of the $T = 1$ versus $T = 0$ states. This problem can be traced back to the uncertainty on the adjustments of $d_{3/2}-d_{3/2}$ monopole matrix elements: since ^{38}O is unbound, the strength of the $T = 1$ monopole cannot be precisely determined in a purely neutron system. As appears here, the $T = 1$ matrix elements of the ZBM2 interaction are too strong with respect to the $T = 0$ elements producing an inversion of the 0^+ and 3^+ levels.

TABLE II: Proton occupancies of the $f_{7/2}p_{3/2}$ orbitals, and the difference in charge radii between 0^+ isomer and 3^+ ground state, calculated within the shell model. See text for details.

	$n_{fp}^\pi(38m)$	$n_{fp}^\pi(38g)$	$\delta \langle r_c^2 \rangle^{38g,38m} (\text{fm}^2)$
ZBM2	0.86	0.50	0.075
ZBM2 modified	0.82	0.41	0.085
Experiment			0.100(6)

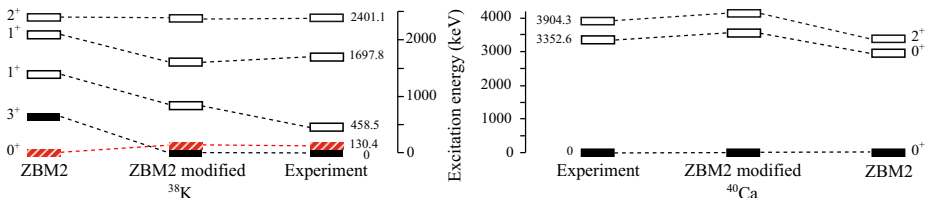


FIG. 4: (color online) Low energy excitation spectra of ^{38}K (left) and ^{40}Ca (right) calculated with the ZBM2 interaction before and after modification of the $V_{d_{3/2},d_{3/2}}^{0,1}$ centroids (see text for details).

In the isospin formalism, the centroids V_{ij} enter the monopole Hamiltonian through the coefficients a_{ij} and b_{ij} , where $a_{ij} = \frac{1}{4}(3V_{ij}^{T=1} + V_{ij}^{T=0})$ and $b_{ij} = V_{ij}^{T=1} - V_{ij}^{T=0}$. While the b_{ij} coefficient fixes the position of the configurations with a given isospin T value, the a_{ij} component fixes the position of configurations dependent on the particle number involved. It is thus always possible to modify the position of the $T = 0$ versus $T = 1$ states via the b_{ij} parameter, leaving the position of particle-hole excited states versus zero-particle-zero-hole configuration unchanged. In our case, we have modified the $V_{d_{3/2},d_{3/2}}^{0,1}$ centroids

to reproduce the spectrum of ^{38}K in the ZBM2 calculation as shown in Fig. 4. This modification leads to a proper behavior of the two-neutron separation energies along the oxygen chain. At the same time, the a_{ij} value is left invariant, preserving the description of the isotope shifts in calcium and other results from the original ZBM2 interaction as illustrated for ^{40}Ca in Fig. 4. From Table II, it can be seen that ZBM2 and the modified version of the interaction provide a similar composition of the ground and isomeric state wave functions, the latter giving $\delta \langle r_c^2 \rangle^{38g,38m} = 0.085 \text{ fm}^2$, even closer to the experimental value of $0.100(6) \text{ fm}^2$.

Finally, we have quantified the role of pairing correlations in the description of the ground and isomeric states by taking the expectation value of the $T = 1$ pairing Hamiltonian in the wave functions of the 3^+ and 0^+ states obtained from the shell-model diagonalization. The absolute value of the pairing contribution to the 0^+ state is 5 MeV larger than to the 3^+ . On the contrary, taking the pairing Hamiltonian restricted to proton-proton and neutron-neutron pairs only, one obtains a small and nearly equal expectation value for both states. Therefore, these are, indeed, the $T = 1, I = 0$ proton-neutron pairs that constitute the essential difference in the building of the 0^+ and 3^+ states.

Returning to Behr *et al.*'s shell-model occupancy constrained spherical Hartree-Fock calculations it is likely that the exclusion of cross-shell correlations and the resulting small difference between the orbital occupancies of the two states is the origin for the incorrect sign of the isomer shift.

It is intriguing to note that the only other odd-odd self-conjugate isomer shift measured to date [21] in ^{50}Mn [35] results in a $\delta \langle r^2 \rangle$ which is identical in magnitude and opposite in sign to that measured here. The sign can be easily understood when one recalls that the $T = 0$ and $T = 1$ levels are inverted after $A = 40$ for all known cases with the exception of ^{58}Cu . While it is too early to draw direct conclusions from this similarity, the measurement of other isomer shifts in odd-odd self-conjugate nuclei such as ^{26}Al and ^{42}Sc could map the evolution of proton-neutron pairing correlations along the line of $N = Z$.

To conclude, both the direction and magnitude of the isomer shift in $^{38}\text{K}^m$ can be described phenomenologically when isovector proton-neutron pairing correlations are considered. Furthermore, a detailed study within the shell model framework has demonstrated good agreement with the observed isomer shift, confirming the significance of these cross-shell correlations in the region of ^{40}Ca .

This work was supported by the IAP-Projects No. P6/23, No. P7/12, the FWO-

Vlaanderen, NSF Grant No. PHY-1068217, BMBF (No. 05 P12 RDCIC), Max-Planck Society and EU FP7 via ENSAR (No. 262010). We would like to thank to the ISOLDE technical group for their support and assistance. H.N. and K.B. acknowledge support from the Helmholtz Association through the Nuclear Astrophysics Virtual Institute NAVI (No. VH-VI-417).

* mark.bissell@cern.ch

- [1] C. Weizsäcker, Z. Phys. **96**, 431 (1935), ISSN 0044-3328, URL <http://dx.doi.org/10.1007/BF01337700>.
- [2] G. Breit, E. U. Condon, and R. D. Present, Phys. Rev. **50**, 825 (1936), URL <http://link.aps.org/doi/10.1103/PhysRev.50.825>.
- [3] E. Wigner, Phys. Rev. **51**, 106 (1937), URL <http://link.aps.org/doi/10.1103/PhysRev.51.106>.
- [4] W. A. Friedman and G. F. Bertsch, Phys. Rev. C **76**, 057301 (2007), URL <http://link.aps.org/doi/10.1103/PhysRevC.76.057301>.
- [5] N. Sandulescu, D. Negrea, J. Dukelsky, and C. W. Johnson, Phys. Rev. C **85**, 061303 (2012), URL <http://link.aps.org/doi/10.1103/PhysRevC.85.061303>.
- [6] R. Subedi et al., Science **320**, 1476 (2008), URL <http://www.sciencemag.org/content/320/5882/1476.abstract>.
- [7] A. O. Macchiavelli et al., Phys. Rev. C **61**, 041303 (2000), URL <http://link.aps.org/doi/10.1103/PhysRevC.61.041303>.
- [8] A. Poves and G. Martinez-Pinedo, Phys. Lett. B **430**, 203 (1998).
- [9] O. Civitarese, M. Reboiro, and P. Vogel, Phys. Rev. C **56**, 1840 (1997), URL <http://link.aps.org/doi/10.1103/PhysRevC.56.1840>.
- [10] K. Neergård, Phys. Rev. C **80**, 044313 (2009), URL <http://link.aps.org/doi/10.1103/PhysRevC.80.044313>.
- [11] I. Bentley and S. Frauendorf, Phys. Rev. C **88**, 014322 (2013), URL <http://link.aps.org/doi/10.1103/PhysRevC.88.014322>.
- [12] J. M. Lattimer and M. Prakash, Astrophys. J. **550**, 426 (2001), URL <http://stacks.iop.org/0004-637X/550/i=1/a=426>.
- [13] J. M. Lattimer and M. Prakash, Science **304**, 536 (2004), URL <http://www.sciencemag.org/content/304/5670/536.abstract>.

- [14] T. Frick, H. Müther, A. Rios, A. Polls, and A. Ramos, Phys. Rev. C **71**, 014313 (2005), URL <http://link.aps.org/doi/10.1103/PhysRevC.71.014313>.
- [15] A. C. Mueller, F. Buchinger, W. Klempert, E. W. Otten, R. Neugart, C. Ekström, and J. Heinemeier, Nucl. Phys. A **403**, 234 (1983), ISSN 0375-9474, URL <http://www.sciencedirect.com/science/article/pii/0375947483902269>.
- [16] H. Franberg et al., Nucl. Instrum. Methods Phys. Res., Sect. B **266**, 4502 (2008).
- [17] J. Papuga et al., Phys. Rev. Lett. **110**, 172503 (2013), URL <http://link.aps.org/doi/10.1103/PhysRevLett.110.172503>.
- [18] K. Kreim et al., Phys. Lett. B **731**, 97 (2014), ISSN 0370-2693, URL <http://www.sciencedirect.com/science/article/pii/S0370269314001038>.
- [19] A. Krieger et al., Nucl. Instrum. Methods Phys. Res., Sect. A **632**, 23 (2011), ISSN 0168-9002, URL <http://www.sciencedirect.com/science/article/pii/S0168900210029256>.
- [20] N. Bendali, H. T. Duong, P. Juncar, J. M. S. Jalm, and J. L. Vialle, J. Phys. B **19**, 233 (1986), URL <http://stacks.iop.org/0022-3700/19/i=2/a=012>.
- [21] B. Cheal and K. T. Flanagan, J. Phys. G **37**, 113101 (2010).
- [22] M. Wang, G. Audi, A. Wapstra, F. Kondev, M. MacCormick, X. Xu, and B. Pfeiffer, Chin. Phys. C **36**, 1603 (2012), URL <http://stacks.iop.org/1674-1137/36/i=12/a=003>.
- [23] A.-M. Martensson-Pendrill, L. Pendrill, A. Salomonson, A. Ynnerman, and H. Warston, J. Phys. B **23**, 1749 (1990).
- [24] J. A. Behr et al., Phys. Rev. Lett. **79**, 375 (1997), URL <http://link.aps.org/doi/10.1103/PhysRevLett.79.375>.
- [25] F. Touchard et al., Phys. Lett. B **108**, 169 (1982).
- [26] M. Horoi, Phys. Rev. C **50**, 2834 (1994), URL <http://link.aps.org/doi/10.1103/PhysRevC.50.2834>.
- [27] E. Caurier et al., Phys. Lett. B **522**, 240 (2001).
- [28] S. Sakakihara and Y. Tanaka, Nucl. Phys. A **691**, 649 (2001), ISSN 0375-9474, URL <http://www.sciencedirect.com/science/article/pii/S0375947401005668>.
- [29] G. Fricke and K. Heilig, *Nuclear Charge Radii, Landolt-Börnstein - Group I Elementary Particles, Nuclei and Atoms*, vol. 20 (Springer, Berlin, 2004), ISBN 978-3-540-42829-9, URL http://dx.doi.org/10.1007/10856314_1.
- [30] G. A. Lalazissis and S. E. Massen, Phys. Rev. C **53**, 1599 (1996), URL <http://link.aps.org/doi/10.1103/PhysRevC.53.1599>.

- [31] G. A. Lalazissis and S. E. Massen, Phys. Rev. C **55**, 2427 (1997), URL <http://link.aps.org/doi/10.1103/PhysRevC.55.2427>.
- [32] J. Duflo and A. P. Zuker, Phys. Rev. C **59**, R2347 (1999).
- [33] J. Blomqvist and A. Molinari, Nucl. Phys. A **106**, 545 (1968), ISSN 0375-9474, URL <http://www.sciencedirect.com/science/article/pii/0375947468905150>.
- [34] E. Caurier, G. Martinez-Pinedo, F. Nowacki, A. Poves, and A. P. Zuker, Rev. Mod. Phys. **77**, 427 (2005).
- [35] F. C. Charlwood et al., Phys. Lett. B **690**, 346 (2010), ISSN 0370-2693, URL <http://www.sciencedirect.com/science/article/pii/S0370269310006520>.

Chapter 6

Conclusion

In this thesis, the results from the studies of the structure of the potassium isotopes were presented. Having one proton less than the Ca isotopes, the K isotopes represent a good benchmark for theoretical models and provide opportunities for their improvements. During the two experiments, hyperfine structure spectra of eleven isotopes were measured, including one isomer. In our studies, we covered two main neutron shell closures, $N = 20$ and $N = 28$, reaching the $N = 32$ sub-shell. Our results provided new information about the evolution of the nuclear structure in the potassium chain for neutron-rich isotopes.

The two experiments were performed at ISOLDE-CERN using collinear laser spectroscopy on bunched ion beams. The main idea of the technique, the experimental set-up together with the details from the experiments are given in the thesis. Improvements in the light collection region with a reduction in the non-resonant photon background counting, allowed us to measure the hyperfine structure of ^{51}K which is produced by about 4000 ions/s. Nuclear properties such as the ground-state spins, magnetic moments and the change in the mean square charge radii were investigated.

The number of peaks in the hyperfine structure spectra revealed immediately the nuclear spin of the ground-state of two isotopes. More precisely, the three peaks in ^{49}K spectra yielded the spin of $I = 1/2$, while a single peak in ^{50}K pointed to $I = 0$. The analysis of the intensity ratios between the hyperfine peaks in the spectra of ^{48}K and ^{51}K allowed us to conclude that the spins are $I = 1$ and $I = 3/2$, respectively. The firm determination of the ground-state spin of these neutron-rich isotopes cleared up the conflicting data in the literature and gave input for studying the evolution of the $\pi(2s_{1/2} - 1d_{3/2})$ energy gap.

It was observed before that the flip of the ground state with $I = 3/2$ and the first-excited state with $I = 1/2$ takes place when the $\nu 1f_{7/2}$ is completely filled. The origin of this effect is found in the monopole part of the NN interaction which brings the $\pi 2s_{1/2}$ and $\pi 1d_{3/2}$ orbits close in energy, and even inverts them at $N = 28$. However, it was unknown what will happen when the next neutron orbit $\nu 2p_{3/2}$ is included. Our studies indicated, the reinversion back to the expected ground-state spin of $I = 3/2$ for a fully filled $\nu 2p_{3/2}$ orbit. The gap between $\pi(2s_{1/2} - 1d_{3/2})$ was investigated in the shell-model framework via effective single-particle energies. From the spin-tensors decomposition of the NN interaction, it was found that this evolution is driven mostly by the central term. In addition, *ab initio* calculations which included three-body ($3N$) forces were carried out. Although, reasonable agreement with the experimental data for the energy difference between $1/2^+$ and $3/2^+$ was found, there is still room for improvements.

The magnetic moments for the isotopes beyond $N = 28$ were measured for the first time. By the comparison with the shell-model calculations with two different interactions, SDPF-NR and SDPF-U, we were able to look into the wave function of the ground state of the entire potassium chain. For odd- A isotopes up to ^{45}K , the main component in the wave function originates from a hole in $\pi 1d_{3/2}$. The isotopes with the spin of $I = 1/2$ ($^{47,49}\text{K}$) are dominated by the $\pi 2s_{1/2}^{-1} \otimes \nu(pf)$ component, however, more mixing with the $[\pi 1d_{3/2}^{-1} \otimes \nu(pf)]_{1/2}$ is found in ^{49}K . In the case of even- A isotopes, the wave function is dominated by a configuration arising from a hole in the $\pi 1d_{3/2}$ orbit. ^{48}K is the only isotope where a very fragmented wave function is found.

Direct measurements of the isomer shift in ^{38}K resulted in a significant difference between the nuclear radius in the ground state ($I^\pi = 3^+$) and isomeric state ($I^\pi = 0^+$). Intuitively, it was explained by that fact that the $\pi\nu$ pair coupled to $I = 0$ can easily be scattered in the pf orbits as they are the same orbits for this $N = Z$ isotope. For the ground state with spin 3, which is due to the coupling of the neutron and proton holes in the $d_{3/2}$ orbital, it is more difficult to make configurations with spin 3 by exciting a proton and a neutron, as the next orbital has spin 7/2. Consequently, the occupation of the πpf orbits is limited for the $I = 3$ state, causing it to have a smaller nuclear radius. The theoretical explanation for such results is found in the shell-model calculations where $Z = N = 20$ excitations were included and $\pi\nu$ paring correlations were taken into account.

Although the results from this thesis shed some light on the conflicting data for the ground-state spin of the neutron-rich potassium isotopes, revealed the reinversion of the single-particle levels and extended our knowledge of the nuclear radii up to $N = 32$, the story is definitely not complete yet. There are

still some open questions that call for further investigation.

To draw firm conclusions related to the evolution of the $1/2^+$ and $3/2^+$, and in particular on how this gap evolves with N , it is crucial to measure the energy of the first-excited state in ^{51}K and establish the spins/energies in ^{53}K . A test on the single-particle nature of the ground and first-excited state could also be studied through transfer reaction studies. However, these studies require the use of radioactive beams at intensities of at least $10^4\text{-}10^5$ pps. These additional studies will help to further test the effective interactions used in the shell-model calculations. This is of special interest since they predicted significantly different evolution of the $\pi(2s_{1/2} - 1d_{3/2})$ gap after $N = 28$. In addition, the *ab initio* calculations could indicate that the three-body forces need to be included in the interaction in order to obtain correct spectroscopic data. This was already discussed for Ca isotopes by Holt *et al.* [95].

The $N = 32$ sub-shell closure was observed in Ca isotopes in the two-neutron separation energy (S_n) from the mass measurements performed by the ISOLTRAP collaboration [96]. However, based on the nuclear radii presented in this thesis, there is no clear evidence for such shell effect at $N = 32$. Additionally, the ISOLTRAP collaboration recently measured the masses of potassium isotopes up to ^{53}K and the results are still under analysis [97]. It would be very interesting to measure hyperfine structure spectra of isotopes beyond $N = 32$ in order to investigate this effect in complementary data.

In addition to the studies of the potassium isotopes at the COLLAPS beam line, an experiment on neutron-rich calcium isotopes was recently performed resulting in the spin determination of ^{51}Ca ($I = 3/2$), measurements of nuclear moments [98] and extending the radii up to $N = 32$. The next experiment with $^{53,54}\text{Ca}$ is already approved, and will employ radioactive detection (β -particles) instead of photons to be more sensitive for these beams which are produced at only 10-100 ions/s.

Appendix A

Radii of potassium isotopes beyond $N = 28$

Beside the results for the nuclear spins, magnetic moments and isomeric shift in ^{38}K which were discussed in previous chapters, the mean square charge radii were also deduced from the same experimental data. The introduction to the mean square charge radius as the property of a nucleus was given in section 2.1.3, while the explanation on how to deduce it from the optical spectra is presented in section 2.2.3.

These results were published in Physics Letters B. In order to complete the story related to the nuclear structure of K isotopes extracted from the collinear laser spectroscopy data, this article is included in the following section.

A.1 Article IV

The results presented in this article extend our knowledge of the change of the mean square charge radii beyond $N = 28$, up to $N = 32$. From the comparison with the results from other isotopic chains in the Ca region, besides the N dependence of the nuclear size, the Z dependence was also investigated.

My contribution to the article is in the analysis which was carried out in parallel with the main author of this article. However, I was not involved in the preparation of the draft and in the process of submitting it to the journal.

Physics Letters B 731, (2014) 97-102

Nuclear charge radii of potassium isotopes beyond $N = 28$

K. Kreim^{a,*}, M. L. Bissell^b, J. Papuga^b, K. Blaum^a, M. De Rydt^b, R. F. Garcia Ruiz^b, S. Goriely^c, H. Heylen^b, M. Kowalska^d, R. Neugart^{a,e}, G. Neyens^b, W. Nörtershäuser^{e,f}, M. M. Rajabali^b, R. Sánchez Alarcón^{g,h}, H. H. Strokeⁱ, D. T. Yordanov^{a,d}

^aMax-Planck-Institut für Kernphysik, Saupfercheckweg 1, D-69117 Heidelberg, Germany

^bInstituut voor Kern- en Stralingsfysica, KU Leuven, B-3001 Leuven, Belgium

^cInstitut d'Astronomie et d'Astrophysique, CP-226, Université Libre de Bruxelles, B-1050 Brussels, Belgium

^dPhysics Department, CERN, CH-1211 Geneva 23, Switzerland

^eInstitut für Kernchemie, Universität Mainz, D-55128 Mainz, Germany

^fInstitut für Kernphysik, Technische Universität Darmstadt, D-64289 Darmstadt, Germany

^gGSI Helmholtzzentrum für Schwerionenforschung GmbH, D-64291 Darmstadt, Germany

^hHelmholtz-Institut Mainz, 55099 Mainz, Germany

ⁱDepartment of Physics, New York University, New York, NY 10003, USA

Abstract

We report on the measurement of optical isotope shifts for $^{38,39,42,44,46-51}\text{K}$ relative to ^{47}K from which changes in the nuclear mean square charge radii across the $N = 28$ shell closure are deduced. The investigation was carried out by bunched-beam collinear laser spectroscopy at the CERN-ISOLDE radioactive ion-beam facility. Mean square charge radii are now known from ^{37}K to ^{51}K , covering all $\nu f_{7/2}$ -shell as well as all $\nu p_{3/2}$ -shell nuclei. These measurements, in conjunction with those of Ca, Cr, Mn and Fe, provide a first insight into the Z dependence of the evolution of nuclear size above the shell closure at $N = 28$.

Keywords: Isotope shift, Nuclear charge radius, Potassium, Collinear laser spectroscopy

1. Introduction

Mean square charge radii of nuclei in the calcium region ($Z = 20$) have been the subject of extensive investigation, both experimentally [1–6] and theoretically [5–10]. Although existing data cover the full $\nu f_{7/2}$ orbital, very little is known on the nuclei above $N = 28$ with valence neutrons in the $p_{3/2}$ orbital. Furthermore, substantial structural changes are predicted in this region, including the inversion and subsequent re-inversion of the $\pi s_{1/2}$ and $\pi d_{3/2}$ shell-model orbitals [1, 11] and the development of subshell closures at $N = 32$ and $N = 34$ [12–16]. Whilst theoretical models of charge radii across the $\nu f_{7/2}$ shell have been successful in describing the trend observed for calcium [8, 9], little is known about how this observable would be influenced by the anticipated structural evolution in the region beyond $N = 28$.

*Corresponding author

Email address: kim.kreim@cern.ch (K. Kreim)

The inversion of the odd- A potassium ground-state configuration from $I = 3/2$ ($\pi d_{3/2}$) in $^{39-45}\text{K}$ to $I = 1/2$ ($\pi s_{1/2}$) for ^{47}K ($N = 28$) was reported by Touchard et al. [1] in 1982 and has subsequently been reproduced by nuclear shell-model and mean-field calculations [17–19]. The question of how the $\pi d_{3/2}$ orbital evolves whilst filling the $\nu p_{3/2}$ orbital has been addressed in a recent paper by Papuga et al. [11] for the even- N isotopes ^{49}K and ^{51}K , having respectively spin 1/2 and 3/2. In the present work, the ground-state structure of the odd- N isotopes ^{48}K and ^{50}K and a detailed analysis of the spin determination for ^{51}K are presented. With the spin measurements on $^{48-51}\text{K}$ the contradictory assignments found in decay spectroscopy data [20–24] are resolved. These spins in combination with the magnetic moment of ^{48}K fully define the region of inversion [25].

In this letter we report on the measurement of optical hyperfine structure and isotope shifts for $^{38,39,42,44,46-51}\text{K}$ relative to ^{47}K , from which changes in the nuclear mean square charge radii are deduced.

2. Experimental method and data analysis

The measurements were carried out at the collinear laser spectroscopy setup COLLAPS [26] at ISOLDE-CERN [27]. Neutron-rich potassium isotopes were produced by 1.4-GeV protons impinging onto a thick UC_x target. The isotopes were surface ionized, accelerated to 40 keV, mass separated and directed to the ISOLDE cooler-buncher ISCOOL [28]. After ISCOOL the ion bunches were directed to the collinear laser spectroscopy beam line, where they were neutralized in collisions with potassium vapor. The atomic $4s\ ^2S_{1/2} \rightarrow 4p\ ^2P_{1/2}$ transition ($\lambda = 769.9\text{ nm}$) was excited by light generated from a cw titanium-sapphire ring laser. Frequency scanning was performed by applying an additional acceleration potential to the neutralization cell, thus varying the Doppler-shifted laser frequency in the reference frame of the atoms. A light collection system consisting of four separate photomultiplier tubes (PMTs) with imaging optics placed perpendicular to the beam path was used to detect the resonance fluorescence photons. Counts from the PMTs were only accepted during the time in which the atom bunches passed through the light collection system. The background from scattered photons was thus reduced by a factor of $\sim 10^4$ [29, 30].

Optical spectroscopy of K isotopes is hindered by the relatively slow decay rate of the atomic transition ($3.8 \times 10^7\text{ s}^{-1}$) as well as a low (2.5 %) quantum efficiency of the PMTs with a high heat-related dark count rate. In order to perform the measurements on a ^{51}K beam of approximately 4000 ions/s, a new optical detection region was developed. Eight 100-mm diameter aspheric lenses were used to precisely image the fluorescence of the laser-excited K atoms onto four extended-red multialkali PMTs in the arrangement shown in Fig. 1. The light-collection efficiency of this system is approximately twice that of the previous standard system described in Mueller et al. [31], whilst the background from scattered laser light is an order of magnitude lower. The PMTs were maintained at -40°C using a refrigerant circulator to reduce dark counts and held under vacuum to prevent ice formation. RG715 colored glass filters were placed in front of the PMTs in order to cut the strong visible beam light originating from stable contaminant beams of Ti and Cr excited in collisions in the charge exchange cell.

Isotope shift measurements were performed relative to ^{47}K . The spectra were fitted with a hyperfine structure (hfs) using a line shape composed of multiple Voigt profiles [32, 33], which were found to describe most adequately the asymmetric line shape, using χ^2 minimization (see Fig. 2 and 4). The asymmetry originates from inelastic collisions in the charge exchange process. The reduced χ^2 of the fit could be improved from 2.2 (single Voigt) to 1.5 (multiple

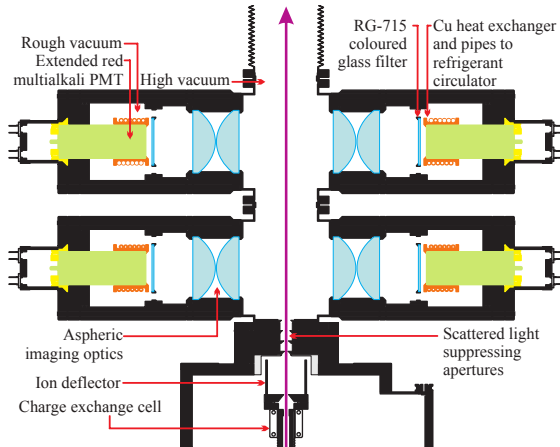


Figure 1: (Color online) Cut through the optical detection region (top view). The atom and laser beams enter the detection region through the charge exchange cell (bottom). For details see text.

Voigt). For the fit a two-parameter first-order hyperfine splitting [34] was used. The magnetic hyperfine parameters A and the centroid of each hfs were extracted. A sample spectrum for ^{48}K is shown in Fig. 2 together with the fitted hfs spectrum. Also shown are the energy levels of the ground state ($S_{1/2}$) and excited state ($P_{1/2}$) with allowed transitions.

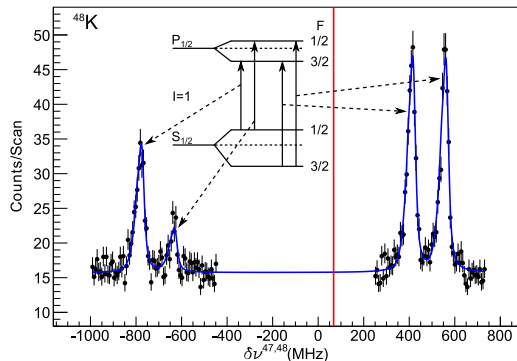


Figure 2: (Color online) Optical spectrum of ^{48}K recorded with 0.2 mW laser power. Also shown is the fitted hfs (blue solid line) and the hfs centroid (red vertical line). The ($S_{1/2}$) and ($P_{1/2}$) level scheme is shown as an inset.

In Table 1 we give the ground-state spins deduced from the measured hfs patterns. The spins measured for $^{37-47}\text{K}$, previously reported in [1, 35], are confirmed by the present analysis. Our new spins measured for ^{49}K and ^{51}K have been published in [11]. The procedure to determine the spins of ^{48}K , ^{50}K and ^{51}K will be described in the following.

Table 1: Spins, isotope shifts referenced to ^{47}K ($\delta\nu^{47,A}$), and changes in mean square charge radii ($\delta\langle r^2 \rangle^{47,A}$) of potassium isotopes in the atomic transition $4s\ ^2S_{1/2} \rightarrow 4p\ ^2P_{1/2}$. Statistical errors are shown in round brackets, systematic errors in square brackets. Complementary data $\delta\nu^{39,A}$ from [3] and [1] (published without systematic errors), referenced to ^{39}K , are quoted in the fourth column.

A	I^π	$\delta\nu^{47,A}$ (MHz)	$\delta\nu^{39,A}$ (MHz)	$\delta\langle r^2 \rangle^{47,A}$ (fm 2)
37	$3/2^+$		-265.4(4)	-0.163(40)[199]
38	3^+	-985.9(4)[34]		-0.126(3)[177]
39	$3/2^+$	-862.5(9)[30]	-127.0(53)	-0.140(51)[174]
			0	-0.037(8)[153]
40	4^-		125.6(3)	-0.066(16)[129]
41	$3/2^+$		235.3(8)	0.036(17)[108]
42	2^-	-506.7(7)[17]		0.034(6)[89]
			351.7(19)	0.026(23)[88]
43	$3/2^+$		459.0(12)	0.049(19)[69]
44	2^-	-292.1(5)[10]		0.036(5)[51]
			564.3(14)	0.047(20)[50]
45	$3/2^+$		661.7(16)	0.072(21)[33]
46	2^-	-91.6(5)[3]		-0.002(4)[16]
			762.8(15)	0.026(21)[16]
47	$1/2^+$	0	857.5(17)	0
48	1^-	67.9(4)[3]		0.186(3)[16]
49	$1/2^+$	135.3(5)[6]		0.342(4)[32]
50	0^-	206.5(9)[9]		0.434(8)[47]
51	$3/2^+$	273.2(14)[11]		0.538(13)[61]

3. Spin determination for $^{48,49,50,51}\text{K}$

For ^{48}K our spin assignment is based on the different relative intensities of the hfs components for ^{46}K ($I = 2$) and ^{48}K . The hfs fits only cannot distinguish between the assumed spins of $I = 1$ and $I = 2$, because the relative splittings are independent of the spin. In Fig. 3 we show the intensities for the individual hfs components of ^{46}K and ^{48}K relative to the $I + 1/2 \rightarrow I + 1/2$ (see Fig. 2) component as a function of laser power. Data points are taken at 0.2 mW and 1.2 mW, the relative intensities at 0 mW represent the theoretical Racah intensities [36]. The hfs of both isotopes have been recorded under identical experimental conditions and the only property that can cause a difference in the relative intensities is the nuclear spin.

The relative intensities of ^{46}K and ^{48}K are significantly different and therefore the spins cannot be the same. The two measured values of ^{46}K at 0.2 mW and 1.2 mW are connected to the relative intensity at 0 mW known for a ground-state spin of $I = 2$ (represented by a solid line). The relative intensities of ^{48}K have to follow a similar trend when going to 0 mW laser power. Compared to ^{46}K the relative intensities of ^{48}K converge to the value at 0 mW corresponding to a ground-state spin of $I = 1$ (represented by a dashed line). We therefore obtain the spin of $I = 1$ for ^{48}K , which supports the 1^- assignment recently proposed by Królas et al. [20] and excludes the 2^- adopted value in the 2006 nuclear data sheets [37].

The spectrum of ^{50}K depicted in Fig. 4 a) shows only a single peak. No fluorescence was observed in a broad scan of 1.4 GHz around the single peak. This is only possible for a ground-state spin of $I = 0$, thus supporting the 0^- assignment by Baumann et al. [22] and excluding the 1^- configuration proposed by Crawford et al. [23].

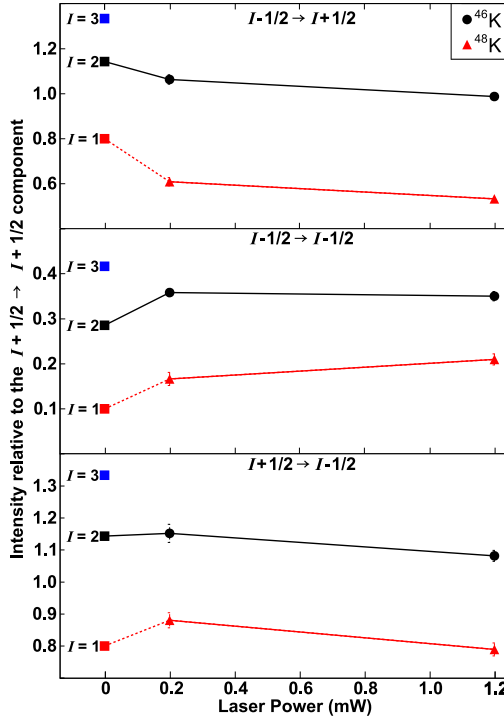


Figure 3: (Color online) Intensities of the hfs components of ${}^{46}\text{K}$ (black dots) and ${}^{48}\text{K}$ (red triangles) relative to the $I + 1/2 \rightarrow I + 1/2$ component. Data points at 0 mW laser power are expected intensities (Racah intensities) for different nuclear spin values. See text for details.

For the determination of the ground-state spin of ${}^{51}\text{K}$ the situation is more complex than in ${}^{48}\text{K}$. Spin $I = 1/2$ can be excluded since four, and not three, peaks are visible in the recorded spectra. Integer spins can be excluded as well, since only the unpaired proton contributes to the spin. Figure 4 b) shows the hyperfine spectrum of ${}^{51}\text{K}$. In our previous work [11] spin 3/2 was assigned mainly on the basis of the magnetic moment. To remove any ambiguity we consider here the relative line intensities, as in the case of ${}^{48}\text{K}$. Due to the exoticity of ${}^{51}\text{K}$, spectra were recorded only at the optimal laser power of 1.2 mW, hence a direct comparison with a particular isotope (e.g. ${}^{39}\text{K}$) for different laser powers is not possible. The solution is to compare the relative intensities of the hyperfine components of ${}^{51}\text{K}$ with those of several other isotopes at $P = 0$ mW (Racah intensities) and $P = 1.2$ mW.

Figure 5 shows these intensities of ${}^{38,39,46,47,48,51}\text{K}$ relative to the $I + 1/2 \rightarrow I + 1/2$ component as a function of laser power. Similar to Fig. 3, the data points are connected to their respective value at $P = 0$ mW with a solid line. The intensities measured for ${}^{51}\text{K}$ are denoted by asterisks. Within the error bars the relative intensities of ${}^{51}\text{K}$ agree with those for a ground-state spin of $I = 3/2$, corresponding to the spin of ${}^{39}\text{K}$. To define a confidence level for the spin determination the observed relative intensities were plotted against the spin.

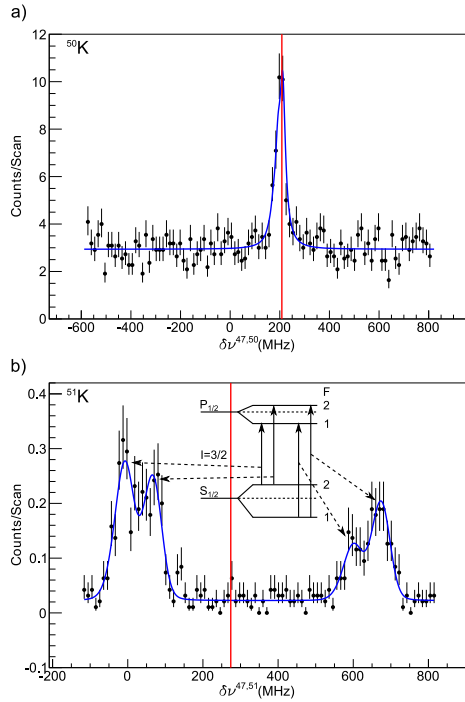


Figure 4: (Color online) Optical spectra of ^{50}K a) and ^{51}K b) as in Fig.2

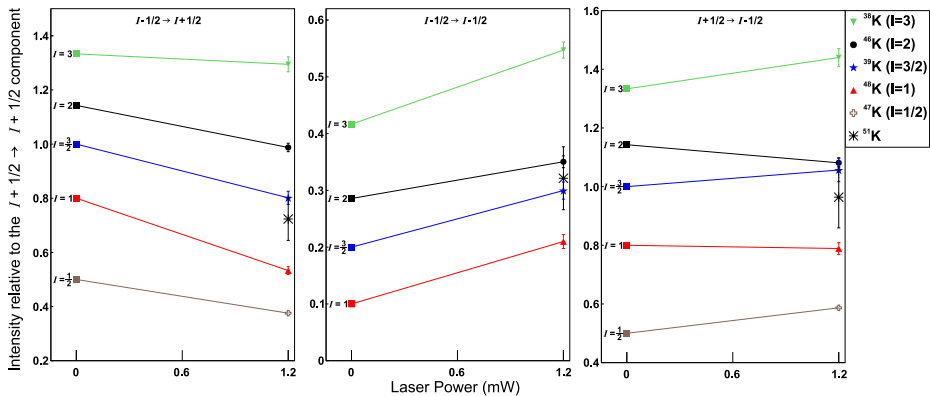


Figure 5: (Color online) Spin determination of ^{51}K based on the intensities of the hyperfine components of $^{38,39,46,47,48,51}\text{K}$ relative to the $I+1/2 \rightarrow I+1/2$ component. Theoretical intensity ratios for the corresponding nuclear spins are plotted at 0 mW, experimental ratios were determined at 1.2 mW laser power. For details see text.

Figure 6 shows the intensities of the hyperfine component $I - 1/2 \rightarrow I + 1/2$ of $^{38,39,46,47,48,51}\text{K}$ (left plot of Fig. 5) relative to the $I + 1/2 \rightarrow I + 1/2$ component. These relative intensities of $^{38,39,46,47,48}\text{K}$ were fitted with a linear function, represented by the dot-dashed line.

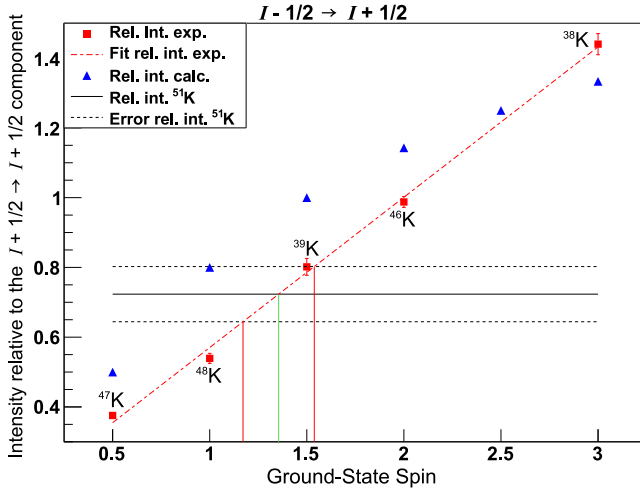


Figure 6: (Color online) Intensities of the hyperfine component $I - 1/2 \rightarrow I + 1/2$ of $^{38,39,46,47,48,51}\text{K}$ relative to the $I + 1/2 \rightarrow I + 1/2$ component as a function of ground-state spin. For details see text.

The relative intensity determined for ^{51}K is given as a horizontal line shown with its error band (dashed lines). The intersection of the relative intensity of ^{51}K with the fitted line projected on the spin axis defines $I = 3/2$ as the ground-state spin. The spin $5/2$ (or higher) is more than 2σ away, and therefore can be ruled out with a confidence of 95 %. The plots for the two remaining intensity ratios from Fig. 5 confirm this level of confidence. As a result, we determine the ground-state spin of ^{51}K to be $I = 3/2$, which supports the $3/2^+$ assignment made by Perrot et al. [24].

With the measured spins for $^{48,50}\text{K}$, along with the magnetic moment of ^{48}K , the discussion on the evolution of the $\pi d_{3/2}$ orbital when filling the $\nu p_{3/2}$ orbital can now be completed. The earlier reported spins and magnetic moments of ^{49}K and ^{51}K revealed a re-inversion of the $\pi s_{1/2}$ and $\pi d_{3/2}$ levels back to their normal ordering, as neutrons are added from $N = 30$ to $N = 32$ [11]. A comparison of the measured observables to large-scale shell-model calculations has shown that like in ^{47}K ($N = 28$), the $\pi s_{1/2}^{-1}$ hole configuration is the dominant component in the ^{49}K ground-state wave function, although its magnetic moment suggests that the wave function has a significant admixture of a $\pi d_{3/2}^{-1}$ hole configuration. In ^{51}K the wave function is dominated by the normal $\pi d_{3/2}^{-1}$ hole and from its magnetic moment a rather pure single-particle wave function can be inferred. The wave functions of the odd-odd $^{48,50}\text{K}$ isotopes have been investigated using the same effective shell-model calculations. A comparison to the experimental data along with a discussion on the occupation of the proton orbitals at $N = 29$ and $N = 31$ will be presented in a forthcoming paper (Papuga et al. [25]).

4. Isotope shifts and charge radii

The measured isotope shifts relative to ^{47}K and literature values referenced to ^{39}K [1, 3] are listed in Table 1, where statistical errors are given in round brackets. The systematic errors, arising mainly from the uncertainty of Doppler shifts depending on the beam energy, are given in square brackets.

The isotope shift between isotopes with atomic numbers A, A' is related to the change in the nuclear mean square charge radii through:

$$\delta\nu^{A,A'} = \nu^{A'} - \nu^A = K \frac{m_{A'} - m_A}{m_{A'} m_A} + F \delta\langle r^2 \rangle^{A,A'} \quad (1)$$

with ν^A and $\nu^{A'}$ representing the transition frequencies with respect to the fine structure levels, $K = K_{\text{NMS}} + K_{\text{SMS}}$ the sum of the normal and the specific mass shift, m_A and $m_{A'}$ the atomic masses, F the electronic factor, and $\delta\langle r^2 \rangle^{A,A'} = \langle r^2 \rangle^{A'} - \langle r^2 \rangle^A$ the change in the nuclear mean square charge radius. For the extraction of $\delta\langle r^2 \rangle^{A,A'}$ from the measured isotope shifts, the specific mass shift ($K_{\text{SMS}} = -15.4(3.8) \text{ GHz u}$) and the electronic factor ($F = -110(3) \text{ MHz fm}^{-2}$) calculated in [2] were used. The normal mass shift ($K_{\text{NMS}} = \nu^{47}\text{m}_e$) was calculated to $K_{\text{NMS}} = 213.55 \text{ GHz u}$ using the D1-frequency of ^{39}K measured in [38]. The masses for ^{37}K - ^{51}K were taken from [39]. The calculated values of $\delta\langle r^2 \rangle^{47,A}$ are shown in Table 1. For the isotope shifts from [1, 3] the same procedure was used to calculate the $\delta\langle r^2 \rangle^{47,A}$ in order to obtain a consistent set of $\delta\langle r^2 \rangle^{47,A}$ over the entire potassium chain. The statistical error on $\delta\langle r^2 \rangle^{47,A}$ (round brackets) originates from the statistical error on the isotope shift whilst the systematic error (square brackets) is dominated by the uncertainty on K_{SMS} and is correlated for all isotopes.

The root mean square (rms) charge radii $\langle r^2 \rangle^{1/2}$ of potassium obtained in this work are plotted in Fig. 7 together with those of argon [5], calcium [40], scandium [6], titanium [41], chromium [42], manganese [4], and iron [43]. The $\langle r^2 \rangle^{1/2}$ values have been obtained by using the originally published changes in mean square charge radii and absolute reference radii from the compilation of Fricke and Heilig [44]. The trends of the isotopic chains below $N = 28$ have been discussed in [5, 6]. In this region the behavior of the rms charge radii displays a surprisingly strong dependence on Z (Fig. 7) with a general increase as a function of N for Ar developing into a dominantly parabolic behavior for Ca and then progressing towards the anomalous downward sloping trends in Sc and Ti. Such dramatic variations of the radii are not observed in the regions around $N = 50, 82$ and 126 [45, 46].

To date, no single theoretical model has fully described the strongly Z -dependent behavior of radii across $Z = 20$ [6], although a variety of approaches have shown some success in describing the observed trends for specific isotopic chains.

To discuss the new results for $N > 28$ we plot the $\delta\langle r^2 \rangle$ of potassium given in Table 1 from $N = 23$ to $N = 32$ together with those of Ar, Mn, Ca, Ti, Cr and Fe referenced to the $N = 28$ shell closure, see Fig. 8. The correlated systematic error in the potassium data is represented by the gray shaded area surrounding the curve. Looking at the $\delta\langle r^2 \rangle$ curves one can see the above discussed Z dependence of the radii in a broad structure below $N = 28$. Common to all elements is the strong shell-closure effect at $N = 28$. Above $N = 28$ the $\delta\langle r^2 \rangle$ values show a steep increasing slope, which is similar for all the elements and thus nearly independent of the number of protons. Below $N = 28$ the $\delta\langle r^2 \rangle$ values show large differences between the elements illustrating the atypical Z dependence below $N = 28$.

What changes at $N = 28$? Up to $N = 28$ the protons and neutrons in the calcium region ($18 \leq Z \leq 26$) occupy the same orbitals (sd and $f_{7/2}$) resulting in a complex interplay of

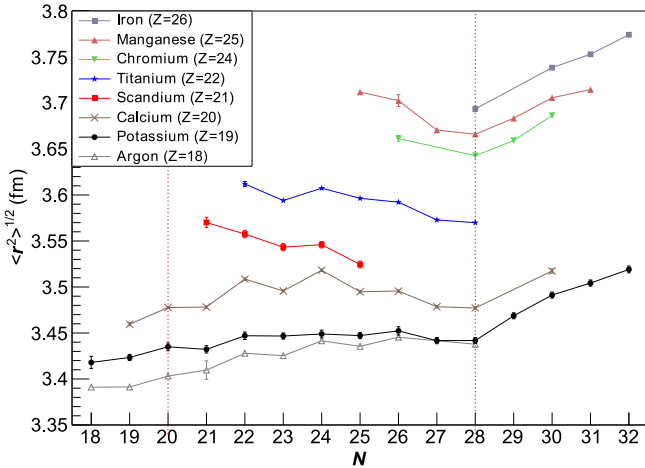


Figure 7: (Color online) Root mean square nuclear charge radii versus neutron number for the isotopes of Ar, K, Ca, Sc, Ti, Cr, Mn and Fe. Data for K results from this work.

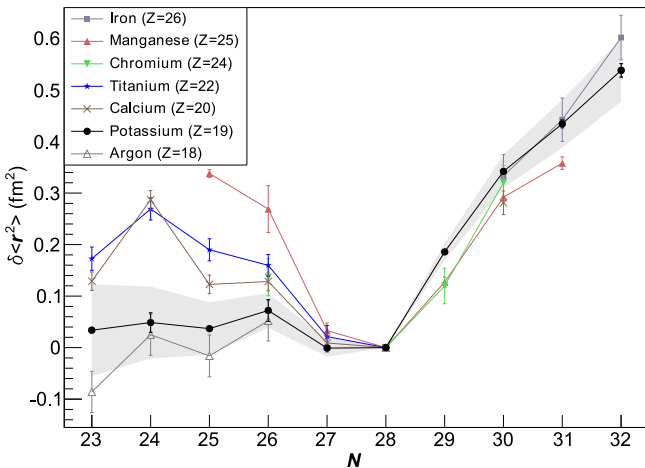


Figure 8: (Color online) Difference in mean square charge radii relative to $N = 28$ versus neutron number for the isotopes of Ar, K, Ca, Ti, Cr, Mn and Fe.

proton and neutron configurations. This fact is underlined by the shell-model calculations of Caurier et al. [9], where the characteristic radii trend (see Fig. 2. in [9]) in calcium between $N = 20$ and $N = 28$ is reproduced qualitatively by allowing multi-proton - multi-neutron excitations from the sd to the fp shell. Above $N = 28$ the neutrons fill the $p_{3/2}$ orbital. Here the changes in mean square radii show little or no dependence on Z , indicating that charge radii are purely driven by a common and collective polarization of the proton

distribution by the neutrons in the $p_{3/2}$ orbital with little or no dependence on the specific proton configuration at the Fermi surface. This absence of strong proton configuration dependence is further emphasized by the consistency of the $^{47,49}\text{K}$ radii, having an inverted ground-state proton configuration, with the radii of the remaining K isotopes as well as all other measured radii in the region. The present data do not allow any conclusion on a possible shell closure at $N = 32$, as discussed in [12–14]. Theoretical and experimental evidence of a shell effect at $N = 32$ exists for Ca, Ti and Cr from the systematics of the first 2^+ state energies $E_x(2_1^+)$ or two-neutron separation energies S_{2n} with the strongest effect in Ca [12, 14–16].

Looking at the branch of $\delta\langle r^2 \rangle$ of K above $N = 28$ one can see that the point for ^{48}K ($N = 29$) deviates from the general odd-even behavior in the K chain as well as the great majority of all nuclei. This general behavior of "normal" odd-even staggering is expressed by a smaller radius of the odd- N compared to the neighboring even- N isotopes. Obviously the value for ^{48}K is larger, corresponding to an "inverted" odd-even staggering. This feature might be related to the particular nature of the ground-state wave function of ^{48}K . Shell-model calculations [25] show that the ground states of ^{47}K and ^{49}K are dominated by an $s_{1/2}$ configuration, while for ^{48}K the dominant part comes from $d_{3/2}$.

The results of the rms charge radii are finally compared to theoretical calculations in the framework of the mean field (MF) model. Both the non-relativistic and relativistic MF approaches are considered because they are known to give rise to different descriptions of the spin-orbit field. The non-relativistic MF traditionally makes use of a phenomenological two-body spin-orbit term in the Skyrme force with a single parameter adjusted to experimental data, such as single-particle level splittings. The form of the spin-orbit term is, however, chosen purely by simplicity. In contrast, in the relativistic MF, the spin-orbit field emerges as a consequence of the underlying Lorentz invariance, and its form does not have to be postulated a priori. This approach, for the first time, led to a proper description of the generally observed charge-radii kinks at magic neutron numbers for the example of Pb [47]. As shown in Fig. 9, such a kink is also predicted by the relativistic MF calculation, based on the DD-ME2 interaction [48], for the K isotopic chain, though the effect is less pronounced than found in our measurement. In contrast, none of the standard Skyrme forces with the traditional spin-orbit term gives rise to a proper description of the kinks. Such a behavior is illustrated in Fig. 9, where the rms nuclear charge radii calculated with the Skyrme-HFB model [49], HFB-24, are compared with experimental data. The parameters of the Skyrme interaction (BSk24) were in this case determined primarily by fitting measured nuclear masses and the properties of infinite nuclear matter.

It has been shown that a generalization of the Skyrme interaction [50, 51] should also be able to map the relativistic spin-orbit field and improve the description of charge radii across the shell closures.

It should be mentioned that neither the relativistic nor the non-relativistic MF models reproduce the parabolic shape between $N = 20$ and 28, nor the odd-even staggering. In particular, both calculations make use of the equal filling approximation and violate the time-reversibility in the treatment of odd nuclei, and consequently are not adequate for a proper description of the odd-even effect.

5. Conclusion

The hyperfine structure and isotope-shift measurements on $^{38,39,42,44,46-51}\text{K}$ performed in the present work offer an insight into the development of the mean square charge radii in

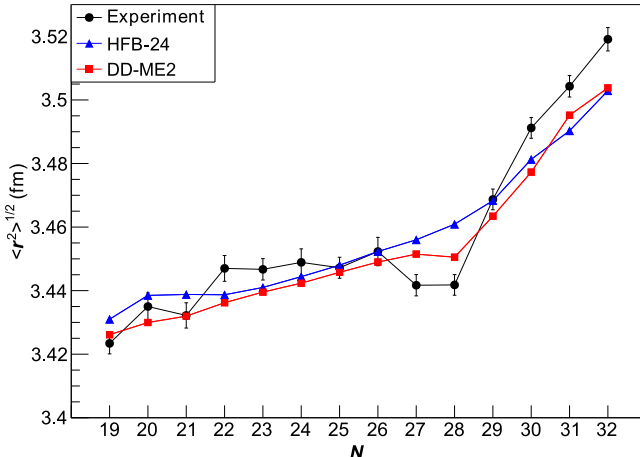


Figure 9: (Color online) rms nuclear charge radii versus neutron number (black dots) compared to theoretical models HFB-24 (blue triangles) and DD-ME2 (red squares).

potassium beyond the $N = 28$ shell closure. The now accessible range of K isotopes with neutron numbers $N = 18\text{--}32$, including the previous data on $^{37\text{--}47}\text{K}$ [1, 3], covers the full $f_{7/2}$ and $p_{3/2}$ orbitals. Our measurement contributes substantially to a systematic investigation of mean square nuclear charge radii in the calcium region beyond the $N = 28$ shell closure. The most striking effect is the difference in the behavior of the rms charge radii below and above $N = 28$. In addition the measured spins of $^{48,50}\text{K}$ together with the spins reported by Papuga et al. [11] allow now assigning spins and parities of excited levels in these isotopes based on a firm ground and resolve the inconsistency between earlier reported data.

This work was supported by the Max-Planck-Society, BMBF (05 P12 RDCIC), the Belgian IAP-projects P6/23 and P7/10, the FWO-Vlaanderen, the NSF grant PHY-1068217 RC 100629, and the EU Seventh Framework through ENSAR (no. 262010). We thank the ISOLDE technical group for their support and assistance.

- [1] F. Touchard, et al., Phys. Lett. B 108 (1982) 169 – 171.
- [2] A.-M. Martensson-Pendrill, et al., J. Phys. B 23 (1990) 1749.
- [3] J. A. Behr, et al., Phys. Rev. Lett. 79 (1997) 375–378.
- [4] F. Charlwood, et al., Phys. Lett. B 690 (2010) 346 – 351.
- [5] K. Blaum, et al., Nucl. Phys. A 799 (2008) 30 – 45.
- [6] M. Avgoulea, et al., J. Phys. G 38 (2011) 025104.
- [7] L. Zamick, Ann. Phys. 66 (1971) 784 – 789.
- [8] I. Talmi, Nucl. Phys. A 423 (1984) 189 – 196.
- [9] E. Caurier, et al., Phys. Lett. B 522 (2001) 240 – 244.

- [10] L. Zamick, Phys. Rev. C 82 (2010) 057304.
- [11] J. Papuga, et al., Phys. Rev. Lett. 110 (2013) 172503.
- [12] M. Honma, T. Otsuka, B. Brown, T. Mizusaki, Eur. Phys. J. A 25 (2005) 499–502.
- [13] A. Gade, T. Glasmacher, Prog. Part. Nucl. Phys. 60 (2008) 161 – 224.
- [14] O. Sorlin, M.-G. Porquet, Prog. Part. Nucl. Phys. 61 (2008) 602 – 673.
- [15] F. Wienholtz, et al., Nature 498 (2013) 346–349.
- [16] D. Steffenbeck, et al., Nature 502 (2013) 207–210.
- [17] A. Gade, et al., Phys. Rev. C 74 (2006) 034322.
- [18] T. Otsuka, et al., Phys. Rev. Lett. 95 (2005) 232502.
- [19] T. Otsuka, et al., Phys. Rev. Lett. 97 (2006) 162501.
- [20] W. Królas, et al., Phys. Rev. C 84 (2011) 064301.
- [21] R. Broda, et al., Phys. Rev. C 82 (2010) 034319.
- [22] P. Baumann, et al., Phys. Rev. C 58 (1998) 1970–1979.
- [23] H. Crawford, et al., Act. Phys. Pol. B40 (2009) 481.
- [24] F. Perrot, et al., Phys. Rev. C 74 (2006) 014313.
- [25] J. Papuga, et al., in preparation for Phys. Rev. C, 2014.
- [26] R. Neugart, Nucl. Instrum. Methods 186 (1981) 165 – 175.
- [27] E. Kugler, Hyp. Interact. 129 (2000) 23–42.
- [28] H. Franberg, et al., Nucl. Instrum. Methods B 266 (2008) 4502 – 4504.
- [29] A. Nieminen, et al., Nucl. Instrum. Methods B 204 (2003) 563 – 569.
- [30] K. T. Flanagan, et al., Phys. Rev. Lett. 103 (2009) 142501.
- [31] A. C. Mueller, et al., Nucl. Phys. A 403 (1983) 234 – 262.
- [32] A. Klose, et al., Nucl. Instrum. Methods A 678 (2012) 114 – 121.
- [33] N. Bendali, H. T. Duong, J. L. Vialle, J. Phys. B 14 (1981) 4231.
- [34] H. Kopfermann, Nuclear Moments, New York: Academic Press, 1958.
- [35] U. Köpf, et al., Z. Phys. 226 (1969) 297–327.
- [36] P. C. Magnante, H. H. Stroke, J. Opt. Soc. Am. 59 (1969) 836–841.
- [37] T. Burrows, Nucl. Data Sheets 107 (2006) 1747 – 1922.
- [38] S. Falke, et al., Phys. Rev. A 74 (2006) 032503.

- [39] M. Wang, et al., Chinese Physics C 36 (2012) 1603–2014.
- [40] L. Vermeeren, et al., Phys. Rev. Lett. 68 (1992) 1679–1682.
- [41] Y. Gangrsky, et al., J. Phys. G 30 (2004) 1089.
- [42] I. Angeli, At. Data Nucl. Data Tables 87 (2004) 185 – 206.
- [43] D. M. Benton, et al., J. Phys. B 30 (1997) 5359.
- [44] G. Fricke, K. Heilig, Nuclear Charge Radii, Landolt-Börnstein: Numerical Data and Functional Relationships in Science and Technology - New Series, Vol. 20, Springer, 2004.
- [45] I. Angeli, et al., J. Phys. G 36 (2009) 085102.
- [46] E. Otten, Nuclear Radii and Moments of Unstable Isotopes, volume 8 of *Treatise on Heavy-Ion Science*, Plenum Press, New York, p. 517.
- [47] M. Sharma, G. Lalazissis, P. Ring, Phys. Lett. B 317 (1993) 9–13.
- [48] G. A. Lalazissis, T. Nikšić, D. Vretenar, P. Ring, Phys. Rev. C 71 (2005) 024312.
- [49] S. Goriely, N. Chamel, J. M. Pearson, Phys. Rev. C 88 (2013) 024308.
- [50] P.-G. Reinhard, H. Flocard, Nucl. Phys. A 584 (1995) 467–488.
- [51] M. M. Sharma, G. Lalazissis, J. König, P. Ring, Phys. Rev. Lett. 74 (1995) 3744–3747.

A.2 Unpublished results - Mean square charge radii of $^{48,51}\text{K}$ for different spins

In addition to the determination of the ground-state spin of $^{48,51}\text{K}$ from the intensity ratios described in the article, another approach which could point to the exclusion of some of the potential spins is simply the difference in the mean square charge radius. The analysis of $^{48,51}\text{K}$ performed for different spins yielded significantly different values for the extracted isotope shift.

The data of ^{48}K were fitted by taking into account $I = 1$ and 2 , while in the case of ^{51}K , the nuclear spins of $I = 3/2, 5/2$ and $7/2$ were considered. The change in the mean square charge radii obtained for all these optional spins are presented in Fig. A.1. The shaded area represents the uncertainty on $\delta\langle r^2 \rangle$ due to the uncertainties on the atomic constants which were used, $F = -110(3)$ MHz fm $^{-2}$ and $K_{SMS} = -15.4(38)$ GHz·u [52].

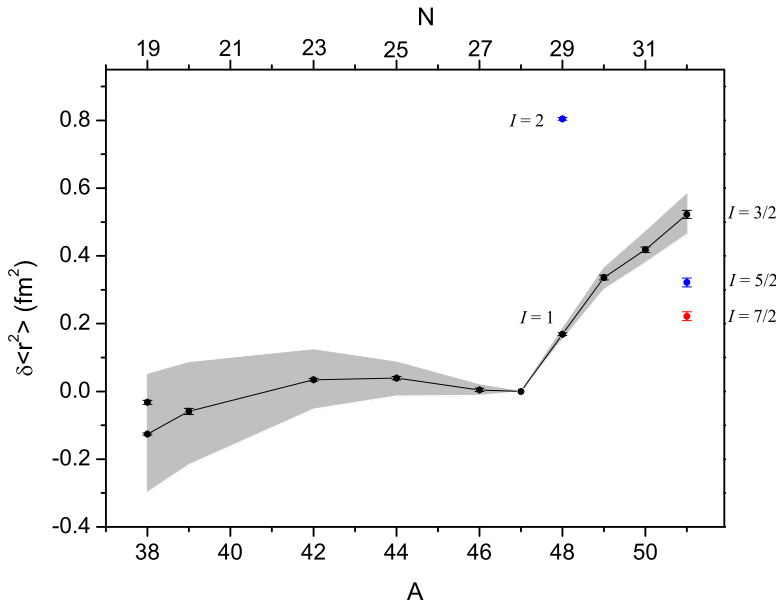


Figure A.1: Change in the mean square charge radii for different spins of ^{48}K and ^{51}K . These results confirmed the conclusions based on the intensity ratios, where it was found that the ground-state spin of ^{48}K is $I = 1$ and of ^{51}K is $I = 3/2$. The uncertainties on the experimental result are statistical, while the gray area is from the uncertainties on F and K_{SMS} .

For ^{48}K , the value for $I = 2$ gives an unphysical jump in the size of the nucleus, which rejects this option for the ground-state spin and confirms $I = 1$ as it was obtained from the intensity ratios.

However, for ^{51}K , this is not the case. Due to the fact that $N = 32$ is a potential shell gap, which would cause a decrease of the $\delta\langle r^2 \rangle$, we could exclude only $I = 7/2$, but not $I = 5/2$.

To further investigate the possible spin values for ^{51}K , the experimental and calculated magnetic moments for all three spin values were compared. The results are presented in Table II in Article I (section 4.3). The magnetic moments for $I = 5/2$ and $7/2$ clearly deviate from the experimental values. In addition, the shell-model calculations predicted the states with these particular spins to be around 2 MeV. Furthermore, the intensity ratios presented in Fig. 5 in Article IV (section A.1) are in agreement with the values obtained for ^{39}K ($I = 3/2$) and deviate from other considered spins. It should be mentioned that for the analysis of the hyperfine parameters the data were always fitted with the intensities left as free parameters.

Appendix B

Multiple Voigt line shape

In contrast to the Voigt profile which is symmetrical, the multiple Voigt line shape is suitable for the description of asymmetrical peaks. In the potassium data, the collisional excitations in the CEC could potentially induce asymmetry in the peaks on the left side. To address this potential issue, the multiple Voigt profile was constructed. The probability for multipole collisions of an atom is given by Poisson's distribution [99]

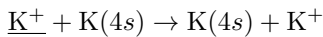
$$P(x) = \frac{e^{-x} x^n}{n!} \quad (\text{B.1})$$

where x is the Poisson factor which depends on the length and vapour density, while n represents the number of collisional excitations and it takes values $n = 0, 1, 2, 3$. The Poisson factor was deduced from the fitted ^{47}K data to be $x = 0.506$ and $x = 0.607$ for data from 2010 and 2012, respectively [68]. The amplitude of the side peaks was fixed according to Eq. (eq: Poisson dist) and the distance between them to 3.06 eV corresponding to the excited state $5p\ ^2P_{1/2}$. Due to the collisions, the ions will lose some energy, thus the side peaks will always appear on the low-frequency side of the main peak.

For the multiple Voigt fit in Fig. 3.11, the mean peak which is without collisional excitations ($n = 0$) is presented in red, while next three are for $n = 1, 2$ and 3 plotted in black, purple and green, respectively. The sum peak is shown in blue.

Applying the studies done by Bendaly and co-authors [99] about the charge exchange processes on $(\text{Na}^+ - \text{Na})$ system, in the K isotopes we can expect:

- resonant channel:



- non-resonant channel:
 $\underline{K^+} + K(4s) \rightarrow \underline{K(4p)} - \Delta E + K^+ \rightarrow \underline{K(4s)} - \Delta E + K^+ + h\nu_{4p,4s}$
- inelastic collisions - before the CEC:
 $\underline{K^+} + K(4s) \rightarrow \underline{K^+} - \Delta E + K(4p) \rightarrow \underline{K^+} - \Delta E + K(4s) + h\nu_{4p,4s}$
- inelastic collisions - after the CEC:
 $\underline{K(4s)} + K(4s) \rightarrow \underline{K(4s)} - \Delta E + K(4p) \rightarrow \underline{K(4s)} - \Delta E + K(4s) + h\nu_{4p,4s}$

In the given reactions on the left side, the incident ion (atomic) beam is underlined, while on the right side, it represents the outgoing atoms/ions.

Appendix C

Additional spectra

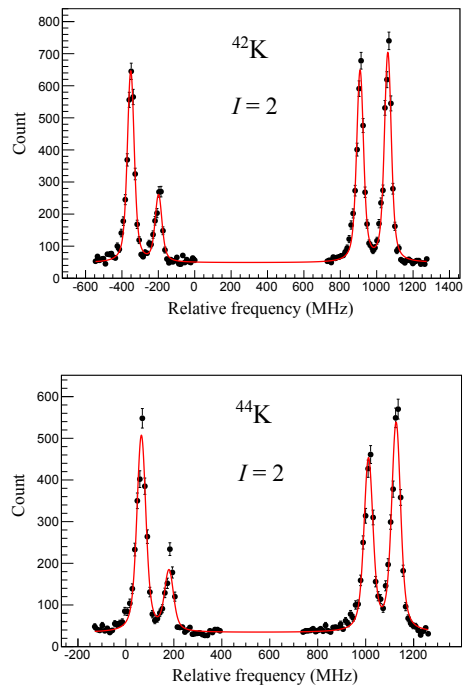


Figure C.1: The hyperfine spectra of ^{42}K and ^{44}K shown relative to the centroid of ^{39}K .

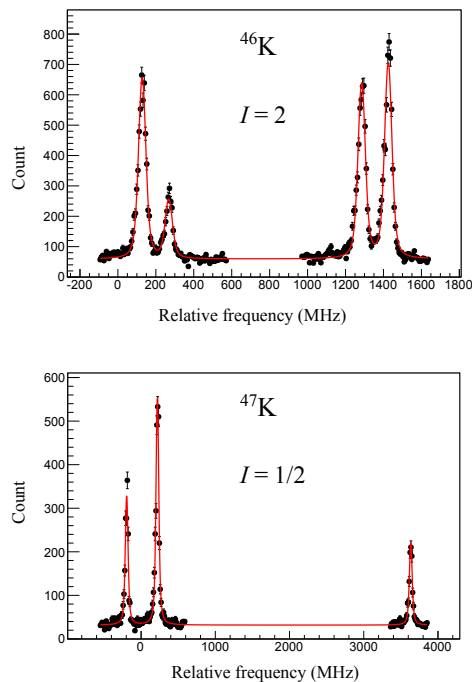


Figure C.2: The hyperfine spectra of ^{46}K and ^{47}K shown relative to the centroid of ^{39}K .

Appendix D

Shell-model calculation

D.1 Centroids

Centroids of the monopole part of the NN interaction are calculated using Eq. (4.4) for isotopes from $N = 21$ up to $N = 34$ for both effective interactions (SDPF-NR and SDPF-U) used in the shell-model calculations. The results are listed in Table D.1. In Table, ΔV is defined as $V_{d_{3/2}j_\nu}^{\pi\nu} - V_{s_{1/2}j_\nu}^{\pi\nu}$, where j_ν is the neutron orbit.

Table D.1: Calculated centroids for isotopes with $21 \leq N \leq 34$ for SDPF-NR and SDPF-U effective interactions. Results are presented in MeV.

N	interaction	centroids		ΔV
$21 \leq N \leq 28$	NR	$V_{d_{3/2}f_{7/2}}^{\pi\nu}$	$V_{s_{1/2}f_{7/2}}^{\pi\nu}$	-0.56
	U	-1.66	-1.09	
$29 \leq N \leq 32$	NR	$V_{d_{3/2}p_{3/2}}^{\pi\nu}$	$V_{s_{1/2}p_{3/2}}^{\pi\nu}$	0.03
	U	-1.21	-1.24	
$33 \leq N \leq 34$	NR	$V_{d_{3/2}p_{1/2}}^{\pi\nu}$	$V_{s_{1/2}p_{1/2}}^{\pi\nu}$	0.70
	U	-1.19	-1.89	
		-1.06	-0.98	-0.08

D.2 Wave function configuration

Shell-model calculations provide insight into the character of the ground-state wave functions. The overview of the results for potassium isotopes is presented in Table D.2 where the contributions of the components of the wave function which originate from a hole in the same proton orbit are summed up. In Table D.3 and D.4 the dominant component together with a few stronger ones are listed for isotopes with $N < 28$ and $28 \leq N \leq 32$, respectively. Table D.5 summarized the configuration of the two lowest states of $I = 2$ in ^{48}K . It should be noted that the configurations with a contribution in the total-wave function of less than 1% are not shown in the output file.

Table D.2: Summary of the composition of the ground-state wave function arising from different proton components, $\pi 2s_{1/2}^{-1} \otimes \nu(sd)$ and $\pi 1d_{3/2}^{-1} \otimes \nu(sd)$ for isotopes with $N \leq 20$, while for isotopes with $N > 20$ the contributions are described as $\pi 2s_{1/2}^{-1} \otimes \nu(pf)$ and $\pi 1d_{3/2}^{-1} \otimes \nu(pf)$. Larger deviation between the predictions from two interactions is only found for isotopes with $N > 28$. The configurations with contribution less than 1% in the total wave function are not shown in the output file, and therefore the total probability does not always add to 100

Isotope	I^π	SDPF-NR		SDPF-U	
		$\pi 2s_{1/2}^{-1}$ (%)	$\pi 1d_{3/2}^{-1}$ (%)	$\pi 2s_{1/2}^{-1}$ (%)	$\pi 1d_{3/2}^{-1}$ (%)
^{38}K	3^+	0	98	0	98
^{39}K	$3/2^+$	0	100	0	100
^{40}K	4^-	2	98	1	98
^{41}K	$3/2^+$	3	95	3	95
^{42}K	2^-	7	91	7	90
^{43}K	$3/2^+$	4	92	4	92
^{44}K	2^-	8	85	7	89
^{45}K	$3/2^+$	8	88	4	90
^{46}K	2^-	7	85	7	85
^{47}K	$1/2^+$	78	13	80	13
^{48}K	1^-	24	64	18	73
^{49}K	$1/2^+$	65	21	72	15
^{50}K	0^-	7	84	4	91
^{51}K	$3/2^+$	2	90	1	93

Table D.3: The main components of the ground-state wave function listed for isotopes with $N < 28$. Clear dominance of the configuration expected from the simple shell model is found for all isotopes. There is almost no difference obtained for different interactions.

Isotope	N	I^π	configuration ($\pi \otimes \nu$)	SDPF-NR (%)	SDPF-U (%)
^{38}K	19	3^+	$d_{3/2}^{-1} \otimes d_{3/2}^{-1}$	97	97
			$d_{3/2}^{-1} \otimes d_{5/2}^{-1}$	1	1
^{39}K	20	$3/2^+$	$d_{3/2}^{-1} \otimes d_{3/2}^4$	100	100
^{40}K	21	4^-	$d_{3/2}^{-1} \otimes f_{7/2}$	98	98
			$s_{1/2}^{-1} \otimes f_{7/2}$	2	1
^{41}K	22	$3/2^+$	$d_{3/2}^{-1} \otimes f_{7/2}^2$	87	89
			$d_{3/2}^{-1} \otimes p_{3/2}^2$	4	3
^{42}K	23	2^-	$d_{3/2}^{-1} \otimes f_{7/2}^3$	81	82
			$d_{3/2}^{-1} \otimes f_{7/2}^2 p_{3/2}$	6	5
			$s_{1/2}^{-1} \otimes f_{7/2}^3$	5	5
^{43}K	24	$3/2^+$	$d_{3/2}^{-1} \otimes f_{7/2}^4$	76	78
			$d_{3/2}^{-1} \otimes f_{7/2}^2 p_{3/2}^2$	6	4
			$d_{3/2}^{-1} \otimes f_{7/2}^2 f_{5/2}^2$	5	4
^{44}K	25	2^-	$d_{3/2}^{-1} \otimes f_{7/2}^5$	71	74
			$d_{3/2}^{-1} \otimes f_{7/2}^4 p_{3/2}$	6	6
			$s_{1/2}^{-1} \otimes f_{7/2}^5$	4	4
^{45}K	26	$3/2^+$	$d_{3/2}^{-1} \otimes f_{7/2}^{-2}$	69	73
			$d_{3/2}^{-1} \otimes f_{7/2}^4 p_{3/2}^2$	7	5
			$d_{3/2}^{-1} \otimes f_{7/2}^4 p_{1/2}^2$	5	5
^{46}K	27	2^-	$d_{3/2}^{-1} \otimes f_{7/2}^{-1}$	69	71
			$s_{1/2}^{-1} \otimes f_{7/2}^{-2} p_{3/2}$	7	7
			$d_{3/2}^{-1} \otimes f_{7/2}^{-2} p_{3/2}$	6	6

Table D.4: Composition of the ground-state wave function for $^{47-51}\text{K}$, predicted by the SDPF-NR and SDPF-U effective interactions. The most dominant configurations are shown as the $\pi \otimes \nu$ orbits and their percentage in the total wave function.

Isotope	N	I^π	SDPF-NR		SDPF-U	
			configuration ($\pi \otimes \nu$)	(%)	configuration ($\pi \otimes \nu$)	(%)
^{47}K	28	$1/2^+$	$s_{1/2}^{-1} \otimes f_{7/2}^8$	70	$s_{1/2}^{-1} \otimes f_{7/2}^8$	73
			$d_{3/2}^{-1} \otimes f_{7/2}^{-1} p_{3/2}$	13	$d_{3/2}^{-1} \otimes f_{7/2}^{-1} p_{3/2}$	13
			$s_{1/2}^{-1} \otimes f_{7/2}^{-2} l_{3/2}^2$	5	$s_{1/2}^{-1} \otimes f_{7/2}^{-2} p_{3/2}^2$	4
			$s_{1/2}^{-1} \otimes f_{7/2}^{-2} f_{5/2}^2$	3	$s_{1/2}^{-1} \otimes f_{7/2}^{-2} f_{5/2}^2$	3
^{48}K	29	1^-	$d_{3/2}^{-1} \otimes p_{3/2}$	39	$d_{3/2}^{-1} \otimes p_{3/2}$	52
			$s_{1/2}^{-1} \otimes p_{3/2}$	17	$s_{1/2}^{-1} \otimes p_{3/2}$	14
			$d_{3/2}^{-1} \otimes f_{7/2}^{-1} p_{3/2}^2$	14	$d_{3/2}^{-1} \otimes f_{7/2}^{-1} p_{3/2}^2$	11
			$d_{3/2}^{-1} \otimes f_{7/2}^{-2} l_{3/2}^{-1}$	5	$d_{3/2}^{-1} \otimes p_{1/2}$	3
^{49}K	30	$1/2^+$	$s_{1/2}^{-1} \otimes f_{7/2}^{-1} p_{3/2}^2$	5	$s_{1/2}^{-1} \otimes f_{7/2}^{-1} p_{3/2}^2$	3
			$s_{1/2}^{-1} \otimes p_{3/2}^2$	51	$s_{1/2}^{-1} \otimes p_{3/2}^2$	62
			$d_{3/2}^{-1} \otimes f_{7/2}^{-1} p_{3/2}^{-1}$	17	$d_{3/2}^{-1} \otimes f_{7/2}^{-1} p_{3/2}^{-1}$	12
			$s_{1/2}^{-1} \otimes f_{7/2}^{-2} l_{3/2}^4$	6	$s_{1/2}^{-1} \otimes p_{1/2}^2$	6
^{50}K	31	0^-	$s_{1/2}^{-1} \otimes p_{1/2}^2$	4	$s_{1/2}^{-1} \otimes f_{7/2}^{-2} p_{3/2}^2 f_{5/2}^2$	3
			$s_{1/2}^{-1} \otimes f_{7/2}^{-2} p_{3/2}^2 f_{5/2}^2$	3	$d_{3/2}^{-1} \otimes p_{3/2}^2$	2
			$d_{3/2}^{-1} \otimes p_{3/2}^{-1}$	64	$d_{3/2}^{-1} \otimes p_{3/2}^{-1}$	77
			$s_{1/2}^{-1} \otimes p_{3/2}^2 p_{1/2}$	7	$d_{3/2}^{-1} \otimes p_{3/2}^2 p_{1/2}$	4
^{51}K	32	$3/2^+$	$d_{3/2}^{-1} \otimes f_{7/2}^{-1} p_{3/2}^{-1} p_{1/2}$	6	$s_{1/2}^{-1} \otimes p_{3/2}^2 p_{1/2}$	4
			$d_{3/2}^{-1} \otimes p_{3/2}^2 p_{1/2}$	5	$d_{3/2}^{-1} \otimes f_{7/2}^{-2} p_{3/2}^{-1} f_{5/2}^2$	3
			$d_{3/2}^{-1} \otimes f_{7/2}^{-2} p_{3/2}^{-1} f_{5/2}^2$	4	$d_{3/2}^{-1} \otimes f_{7/2}^{-1} p_{3/2}^{-1} p_{1/2}$	2
			$d_{3/2}^{-1} \otimes p_{3/2}^4$	65	$d_{3/2}^{-1} \otimes p_{3/2}^4$	75
			$a_{3/2}^{-1} \otimes p_{3/2}^2 p_{1/2}^2$	11	$d_{3/2}^{-1} \otimes p_{3/2}^2 p_{1/2}^2$	8
			$d_{3/2}^{-1} \otimes p_{3/2}^{-1}$	5	$d_{3/2}^{-1} \otimes p_{3/2}^{-1}$	4
			$d_{3/2}^{-1} \otimes f_{7/2}^{-2} p_{3/2}^4 f_{5/2}^2$	4	$d_{3/2}^{-1} \otimes f_{7/2}^{-2} p_{3/2}^4 f_{5/2}^2$	3
			$d_{3/2}^{-1} \otimes f_{7/2}^{-2} p_{3/2}^4 p_{1/2}^2$	3	$d_{3/2}^{-1} \otimes f_{7/2}^{-1} p_{3/2}^{-1} p_{1/2} f_{5/2}$	2

Table D.5: Wave function configuration of the three lowest states in ^{48}K from the shell-model calculations using two interactions, SDPF-NR and SDPF-U. Experimental results: $I = 1$ and $\mu_{\text{exp}} = -0.8997(3)$ [45] μ_N .

Interaction	I	E (keV)	$\mu (\mu_N)$	$s_{1/2}^{-1}$ (%)	$d_{3/2}^{-1}$ (%)	configuration	(%)
SDPF-NR	2	0	+0.46	72	16	$s_{1/2}^{-1} \otimes p_{3/2}$	66
						$d_{3/2}^{-1} \otimes f_{7/2}^{-1} p_{3/2}^2$	13
						$s_{1/2}^{-1} \otimes f_{7/2}^{-2} p_{3/2}^{-1}$	3
	1	407	-0.77	24	64	$d_{3/2}^{-1} \otimes p_{3/2}$	39
						$s_{1/2}^{-1} \otimes p_{3/2}$	17
						$d_{3/2}^{-1} \otimes f_{7/2}^{-1} p_{3/2}^2$	14
	2	408	-0.71	10	80	$d_{3/2}^{-1} \otimes p_{3/2}$	62
						$s_{1/2}^{-1} \otimes f_{7/2}^{-1} p_{3/2}^2$	8
						$d_{3/2}^{-1} \otimes f_{7/2}^{-2} p_{3/2}^{-1}$	6
SDPF-U	2	0	+0.49	74	16	$s_{1/2}^{-1} \otimes p_{3/2}$	69
						$d_{3/2}^{-1} \otimes f_{7/2}^{-1} p_{3/2}^2$	11
						$d_{3/2}^{-1} \otimes p_{3/2}$	5
	2	340	-0.61	9	83	$d_{3/2}^{-1} \otimes p_{3/2}$	70
						$s_{1/2}^{-1} \otimes f_{7/2}^{-1} p_{3/2}^2$	5
						$d_{3/2}^{-1} \otimes f_{7/2}^{-1} p_{3/2}^2$	5
	1	395	-0.55	18	73	$d_{3/2}^{-1} \otimes p_{3/2}$	52
						$s_{1/2}^{-1} \otimes p_{3/2}$	14
						$d_{3/2}^{-1} \otimes f_{7/2}^{-1} p_{3/2}^2$	11

Bibliography

- [1] M. Goeppert Mayer, "On closed shells in nuclei ii," *Phys. Rev.*, vol. 75, p. 1969, 1949. pages 1, 4
- [2] O. Haxel, J. Jensen, and H. Suess, "On the "magic numbers" in nuclear structure," *Phys. Rev.*, vol. 75, p. 1766, 1949. pages 1, 4
- [3] S. Raman, C. W. Nestor, and P. Tikkanen, "Transition probabilities from the ground to the first-excited 2^+ state of even-even nuclides," *Atomic Data and Nuclear Data Tables*, vol. 78, pp. 1–128, 2001. pages 2, 7
- [4] K. L. G. Heyde, *The Nuclear Shell Model*. Springer-Verlag Berlin Heidelberg, 1990. pages 2, 3, 15, 16, 17, 19, 67
- [5] A. Bohr and B. R. Mottelson, *Nucelar Structure*. World Scientific Publishing Co. Pte. Ltd., 1998. pages 3, 4, 15
- [6] R. F. Casten, *Nuclear Structure From A Simple Perspective, Second edition*. Oxford Science publications, 2005. pages 4, 5, 62
- [7] M. Goeppert Mayer, "Nuclear configurations in the spin-orbit coupling model. i. empirical evidence," *Phys. Rev.*, vol. 78, pp. 16–21, 1950. pages 4
- [8] O. Sorlin and M.-G. Porquet, "Nuclear magic numbers: New features far from stability," *Prog. Part. Nucl. Phys.*, vol. 61, pp. 602–673, 2008. pages 6, 8, 60
- [9] D. Guillemaud-Mueller, M. Detraz, M. Langevin, F. Naulin, M. De Saint-Simon, C. Thibault, F. Touchard, and M. Epherre, " β decay schemes of very neutron-rich sodium isotopes and their descendants," *Nucl. Phy*, vol. 426, pp. 37–76, 1984. pages 6
- [10] C. Détraz, D. Guillemaud, G. Huber, R. Klapisch, M. Langevin, F. Naulin, C. Thibault, L. C. Carraz, and F. Touchard, "Beta decay of $^{27-32}\text{Na}$ and their descendants," *Phys. Rev. C*, vol. 19, pp. 164–176, 1979. pages 6, 7

- [11] A. Poves and J. Retamosa, "The onset of deformation at the $N = 20$ neutron shell closure far from stability," *Phys. Lett. B*, vol. 184, pp. 311–315, 1987. pages 7
- [12] K. Heyde and J. Wood, "Intruder states and shape coexistence in the region $N \sim 20$, $Z \sim 12$," *J. Phys. G: Nucl. Part. Phys.*, vol. 17, pp. 135–143, 1991. pages 7
- [13] E. K. Warburton, J. A. Becker, and B. A. Brown, "Mass systematics for $A = 29 - 44$ nuclei: The deformed $A \sim 32$ region," *Phys. Rev. C*, vol. 41, pp. 1147–1166, 1990. pages 7
- [14] "Evaluated nuclear structure data file (ensdf) retrieval." <http://www.nndc.bnl.gov/ensdf/>. pages 7, 10, 11
- [15] P. Fallon, E. Rodriguez-Vieitez, A. O. Macchiavelli, A. Gade, J. A. Tostevin, P. Adrich, D. Bazin, M. Bowen, C. M. Campbell, R. M. Clark, J. M. Cook, M. Cromaz, D. C. Dinca, T. Glasmacher, I. Y. Lee, S. McDaniel, W. F. Mueller, S. G. Prussin, A. Ratkiewicz, K. Siwek, J. R. Terry, D. Weisshaar, M. Wiedeking, K. Yoneda, B. A. Brown, T. Otsuka, and Y. Utsuno, "Two-proton knockout from ^{32}Mg : Intruder amplitudes in ^{30}Ne and implications for the binding of $^{29,31}\text{F}$," *Phys. Rev. C*, vol. 81, p. 041302, 2010. pages 7
- [16] T. Otsuka *et al.*, "Novel features of nuclear forces and shell evolution in exotic nuclei," *Phys. Rev. Lett.*, vol. 104, p. 012501, 2010. pages 8
- [17] T. Glasmacher, B. A. Brown, M. J. Chromika, P. D. Cottle, M. Fauerbach, R. W. Ibbotson, K. W. Kernper, D. J. Morrissey, H. Scheit, D. W. Sklenicka, and M. Steiner, "Collectivity in ^{44}S ," *Phys. Lett. B*, vol. 395, pp. 163–168, 1997. pages 8
- [18] H. Scheit, T. Glasmacher, B. A. Brown, J. A. Brown, P. D. Cottle, P. G. Hansen, R. Harkewicz, M. Hellström, R. W. Ibbotson, J. K. Jewell, K. W. Kemper, D. J. Morrissey, M. Steiner, P. Thirolf, and M. Thoennessen, "New region of deformation: The neutron-rich sulfur isotopes," *Phys. Rev. Lett.*, vol. 77, pp. 3967–3970, 1996. pages 8
- [19] B. Bastin, S. Grévy, D. Sohler, O. Sorlin, Z. Dombrádi, N. L. Achouri, J. C. Angélique, F. Azaiez, D. Baiborodin, R. Borcea, C. Bourgeois, A. Buta, A. Bürger, R. Chapman, J. C. Dalouzy, Z. Dlouhy, A. Drouard, Z. Elekes, S. Franchoo, S. Iacob, B. Laurent, M. Lazar, X. Liang, E. Liénard, J. Mrazek, L. Nalpas, F. Negoita, N. A. Orr, Y. Penionzhkevich, Z. Podolyák, F. Pougheon, P. Roussel-Chomaz, M. G. Saint-Laurent, M. Stanoiu, I. Stefan, F. Nowacki, and A. Poves, "Collapse of the $N = 28$ shell closure in ^{42}Si ," *Phys. Rev. Lett.*, vol. 99, p. 022503, 2007. pages 8, 11, 12

- [20] K. T. Flanagan, P. Vingerhoets, M. Avgoulea, J. Billowes, M. L. Bissell, K. Blaum, B. Cheal, M. De Rydt, V. N. Fedosseev, D. H. Forest, Ch. Geppert, U. Köster, M. Kowalska, J. Krämer, K. L. Kratz, A. Krieger, E. Mané, B. A. Marsh, T. Materna, L. Mathieu, P. L. Molkanov, R. Neugart, G. Neyens, W. Nörterhäuser, M. D. Seliverstov, O. Serot, M. Schug, M. A. Sjoedin, J. R. Stone, N. J. Stone, H. H. Stroke, G. Tungate, D. T. Yordanov, and Y. M. Volkov, “Nuclear spins and magnetic moments of $^{71,73,75}\text{cu}$: Inversion of $\pi 2p_{3/2}$ and $\pi 1f_{5/2}$ levels in ^{75}cu ,” *Phys. Rev. Lett.*, vol. 103, p. 142501, 2009. pages 8
- [21] D. F. Measday and T. J. Stocki, “ γ rays from muon capture in natural ca, fe, and ni,” *Phys. Rev. C*, vol. 73, p. 045501, 2006. pages 9, 12
- [22] A. Huck, G. Klotz, A. Knipper, C. Miehe, and G. Walter, “Levels in ^{45}K and ^{46}K excited by the β decay of ^{45}Ar and ^{46}Ar ,” *Phys. Rev. C*, vol. 21, p. 2, 1980. pages 9, 12
- [23] L. Weissman, O. Arnd, U. Bergmann, A. Brown, R. Catherall, J. Cederkall, I. Dillmann, O. Hallmann, L. Fraile, S. Franchoo, L. Gaudefroy, U. Köster, K.-L. Kratz, B. Pfeiffer, and O. Sorlin, “ β decay of ^{47}Ar ,” *Phys. Rev. C*, vol. 70, p. 024304, 2004. pages 9, 12
- [24] L. C. Carraz, P. G. Hansen, A. Huck, B. Jonson, G. Klotz, A. Knipper, K. L. Kratz, C. Miéhé, S. Mattsson, G. Nyman, H. Ohm, A. M. Poskanzer, A. Poves, H. L. Ravn, C. Richard-Serre, A. Schröder, G. Walter, and W. Ziegert, “The ^{49}K beta decay,” *Physics Letters B*, vol. 109, no. 6, pp. 419 – 422, 1982. pages 9
- [25] R. Broda, J. Wrzesiński, A. Gadea, N. Mărginean, B. Fornal, L. Corradi, A. M. Stefanini, W. Królas, T. Pawłat, B. Szpak, S. Lunardi, J. J. Valiente-Dobon, D. Mengoni, E. Farnea, M. P. Carpenter, G. De Angelis, F. Della Vedova, E. Fioretto, B. Guiot, R. V. F. Janssens, P. F. Mantica, P. Mason, G. Montagnoli, D. R. Napoli, R. Orlandi, I. Pokrovskiy, G. Pollarolo, E. Sahin, F. Scarlassara, R. Silvestri, S. Szilner, C. A. Ur, M. Trotta, and S. Zhu, “Proton-hole states in the $N = 30$ neutron-rich isotope ^{49}K ,” *Phys. Rev. C*, vol. 82, p. 034319, Sep 2010. pages 10
- [26] F. Perrot, F. Maréchal, C. Jollet, P. Dessagne, J.-C. Angélique, G. Ban, P. Baumann, F. Benrachi, U. Bergmann, C. Borcea, A. Buță, J. Cederkall, S. Courtin, J.-M. Daugas, L. M. Fraile, S. Grévy, A. Jokinen, F. R. Lecolley, E. Liénard, G. Le Scornet, V. Méot, Ch. Miehé, F. Negoită, N. A. Orr, S. Pietri, E. Poirier, M. Ramdhane, O. Roig, I. Stefan, and W. Wang, “ β -decay studies of neutron-rich K isotopes,” *Phys. Rev. C*, vol. 74, p. 014313, 2006. pages 10

- [27] L. G. Multhauf, K. G. Tirsell, S. Raman, and J. B. McGrory, “Potassium 48,” *Phys. Lett. B*, vol. 57, pp. 44–46, 1975. pages 10
- [28] W. Królas, R. Broda, B. Fornal, R. V. F. Janssens, A. Gadea, S. Lunardi, J. J. Valiente-Dobon, D. Mengoni, N. Mărginean, L. Corradi, A. M. Stefanini, D. Bazzacco, M. P. Carpenter, G. De Angelis, E. Farnea, E. Fioretto, F. Galtarossa, T. Lauritsen, G. Montagnoli, D. R. Napoli, R. Orlandi, T. Pawłat, I. Pokrovskiy, G. Pollarolo, E. Sahin, F. Scarlassara, D. Seweryniak, S. Szilner, B. Szpak, C. A. Ur, J. Wrzesiński, and S. Zhu, “Coupling of the proton-hole and neutron-particle states in the neutron-rich ^{48}K isotope,” *Phys. Rev. C*, vol. 84, p. 064301, 2011. pages 10
- [29] P. Baumann, M. Boumajma, F. Didierjean, A. Huck, A. Knipper, M. Ramdhane, G. Walter, G. Marguier, C. Richard-Serre, and B. A. Brown, “Meson-exchange enhancement in first-forbidden β transitions: The case of ^{50}K and ^{38}Ca ,” *Phys. Rev. C*, vol. 58, pp. 1970–1979, 1998. pages 10
- [30] H. Crawford, R. Janssens, P. Mantica, J. Berryman, R. Broda, M. Carpenter, B. Fornal, G. Grinyer, N. Hoteling, B. Kay, T. Lauritsen, K. Minamisono, I. Stefanescu, J. Stoker, W. Walters, and S. Zhuc, “ β decay studies of neutron-rich nuclei near ^{52}Ca ,” *Acta Physica Polonica B*, vol. 40, p. 481, 2009. pages 10
- [31] F. Touchard, P. Guimbal, S. Büttgenbach, R. Klapisch, M. De Saint Simon, J. M. Serre, C. Thibault, H. T. Duong, P. Juncar, S. Liberman, J. Pinard, and J. L. Vialle, “Isotope shifts and hyperfine structure of $^{38-47}\text{K}$ by laser spectroscopy,” *Phys. Lett. B*, vol. 108, p. 169, 1982. pages 10, 39, 40, 43, 45, 47, 48
- [32] J. A. Behr, A. Gorelov, T. Swanson, O. Häusser, K. P. Jackson, M. Trinczek, U. Giesen, J. M. D’Auria, R. Hardy, T. Wilson, P. Choboter, F. Leblond, L. Buchmann, M. Dombsky, C. D. P. Levy, G. Roy, B. A. Brown, and J. Dilling, “Magneto-optic trapping of β -decaying $^{38}\text{K}^m$, ^{37}K from an online isotope separator,” *Phys. Rev. Lett.*, vol. 79, pp. 375–378, 1997. pages 10, 48, 113
- [33] M. Schäfer, W.-D. Schmidt-Ott, T. Dörfler, T. Hild, T. Pfeiffer, R. Collatz, H. Geissel, M. Hellström, Z. Hu, H. Irnich, N. Iwasa, M. Pfützner, E. Roeckl, M. Shibata, B. Pfeiffer, K. Asahi, H. Izumi, H. Ogawa, H. Sato, H. Ueno, and H. Okuno, “Polarization in fragmentation, g factor of ^{35}K ,” *Phys. Rev. C*, vol. 57, pp. 2205–2214, 1998. pages 10
- [34] J. Dietrich, R. Neugart, and E. W. Otten, “Nuclear spins and magnetic moments of ^{20}Na and ^{36}K by β -radiation detected optical pumping,” *Nucl. Phys. A*, vol. 246, pp. 187–209, 1975. pages 10

- [35] A. Beckmann, K. D. Böklen, and D. Elke, "Precision measurements of the nuclear magnetic dipole moments of ${}^6\text{Li}$, ${}^7\text{Li}$, ${}^{23}\text{Na}$, ${}^{39}\text{K}$ and ${}^{41}\text{K}$," *Zeitschrift für Physik A Hadrons and Nuclei*, vol. 270, pp. 173–186, 1974. pages 10, 44, 53, 54, 57, 58
- [36] Y. W. Chan, V. W. Cohen, and H. B. Silsbee, "Hyperfine structure and nuclear magnetic moment of ${}^{42}\text{K}$," *Phys. Rev.*, vol. 184, p. 1102, 1969. pages 10, 43, 57, 58
- [37] J. T. Eisinger, B. Bederson, and B. T. Feld, "The magnetic moment of ${}^{40}\text{K}$ and the hyperfine structure anomaly of the potassium isotopes," *Phys. Rev.*, vol. 86, p. 73, 1952. pages 10, 54, 57, 58
- [38] M. Wang, G. Audi, A. H. Wapstra, F. Kondev, M. MacCormick, X. Xu, and B. Pfeiffer, "The ame2012 atomic mass evaluation," *Chinese Physics C*, vol. 36, p. 1603, 2012. pages 11, 36
- [39] R. K. Bansal and J. B. French, "Even-parity-hole states in $f_{7/2}$ -shell nuclei," *Phys. Lett.*, vol. 11, pp. 145–148, 1964. pages 11
- [40] F. Pellegrini, "Separation energies between the $2s_{1/2}$ and $1d_{3/2}$ hole states in the odd potassium isotopes," *Phys. Rev. C*, vol. 19, pp. 2412–2413, 1979. pages 11
- [41] A. Gade, B. A. Brown, D. Bazin, C. M. Campbell, J. A. Church, D. C. Dinca, J. Enders, T. Glasmacher, M. Horoi, Z. Hu, K. W. Kemper, W. F. Mueller, T. Otsuka, L. A. Riley, B. T. Roeder, T. Suzuki, J. R. Terry, K. L. Yurkewicz, and H. Zwahlen, "Evolution of the $e(1/2_1^+)$ – $e(3/2_1^+)$ energy spacing in odd-mass K, Cl, and P isotopes for $N = 20 - 28$," *Phys. Rev. C*, vol. 74, p. 034322, 2006. pages 11
- [42] S. Szilner, L. Corradi, F. Haas, G. Pollarolo, L. Angus, S. Beghini, M. Bouhelal, R. Chapman, E. Caurier, S. Courtin, E. Farnea, E. Fioretto, A. Gadea, A. Goasduff, D. Jelavić Malenica, V. Kumar, S. Lunardi, N. Mărginean, D. Mengoni, T. Mijatović, G. Montagnoli, F. Recchia, E. Sahin, M.-D. Salsac, F. Scarlassara, J. F. Smith, N. Soić, A. M. Stefanini, C. A. Ur, and J. J. Valiente-Dobón, "Structure of chlorine isotopes populated by heavy ion transfer reactions," *Phys. Rev. C*, vol. 87, p. 054322, 2013. pages 11, 12
- [43] O. Sorlin, Z. Dombrádi, D. Sohler, F. Azaiez, J. Timár, Y.-E. Penionzhkevich, F. Amorini, D. Baiborodin, A. Bauchet, F. Becker, M. Belleguic, C. Borcea, C. Bourgeois, Z. Dlouhy, C. Donzaud, J. Duprat, L. Gaudefroy, D. Guillemaud-Mueller, F. Ibrahim, M. Lopez, R. Lucas, S. Lukyanov, V. Maslov, J. Mrazek, C. Moore, F. Nowacki, F. Pougeon,

- M. Saint-Laurent, F. Sarazin, J. Scarpaci, G. Sletten, M. Stanoiu, C. Stodel, M. Taylor, and C. Theisen, “Structure of the neutron-rich $^{37,39}\text{P}$ and $^{43,45}\text{Cl}$ nuclei,” *The European Physical Journal A - Hadrons and Nuclei*, vol. 22, pp. 173–178, 2004. pages 11, 12
- [44] J. Fridmann, I. Wiedenhover, A. Gade, L. T. Baby, D. Bazin, B. A. Brown, C. M. Campbell, J. M. Cook, P. D. Cottle, E. Diffenderfer, D.-C. Dinca, T. Glasmacher, P. G. Hansen, K. W. Kemper, J. L. Lecouey, W. F. Mueller, H. Olliver, E. Rodriguez-Vieitez, J. R. Terry, J. A. Tostevin, and K. Yoneda, ““Magic” nucleus ^{42}Si ,” *Nature*, vol. 435, pp. 922–924, 2005. pages 11, 12
- [45] R. Neugart and G. Neyens, “Nuclear moments,” *Lecture Notes in Physics*, vol. 2, pp. 135–189, 2006. pages 15, 19, 20, 21, 31, 36
- [46] B. Castel and I. S. Towner, *Modern Theories of Nuclear Moments*. Oxford Science publications, 1990. pages 15
- [47] P. Mohr and B. Taylor, “CODATA recommended values of the fundamental physical constants: 1998,” *Reviews of Modern Physics*, vol. 72, pp. 351–495, 2000. pages 16
- [48] A. Mooser, S. Ulmer, K. Blaum, K. Franke, H. Kracke, C. Leiteritz, W. Quint, C. C. Rodegheri, C. Smorra, and J. Walz, “Direct high-precision measurement of the magnetic moment of the proton,” *Nature*, vol. 509, pp. 596–599, 2014. pages 16
- [49] A. de Shalit and I. Talmi, *Nuclear Shell Theory*. Academic Press, New York, 1963. pages 19
- [50] P. C. Magnante and H. H. Stroke, “Isotope shift between ^{209}Bi and 6.3 day ^{206}Bi ,” *J. Opt. Soc. Am.*, vol. 59, pp. 836–841, 1969. pages 23
- [51] K. Kreim, M. L. Bissell, J. Papuga, K. Blaum, M. De Rydt, R. F. Garcia Ruiz, S. Goriely, H. Heylen, M. Kowalska, R. Neugart, G. Neyens, W. Nörtershäuser, R. Rajabali, M. M. and Sánchez Alarcón, H. H. Storoke, and D. T. Yordanov, “Nuclear charge radii of potassium isotopes beyond $N = 28$,” *Phys. Lett. B*, vol. 731, pp. 97–102, 2014. pages 23, 49
- [52] A.-M. Martensson-Pendrill, L. Pendrill, S. Salomonson, A. Ynnerman, and H. Warston, “Reanalysis of the isotope shift and nuclear charge radii in radioactive potassium isotopes,” *J. Phys. B: At. Mol. Phys.*, vol. 23, pp. 1749–1761, 1990. pages 25, 145
- [53] E. C. Seltzer, “K x-ray isotope shifts,” *Phys. Rev.*, vol. 188, p. 1916, 1969. pages 25

- [54] E. W. Otten, *Nuclei Far From Stability*, vol. Vol. 8; Treatise on Heavy-Ion Science. Plenum Press, New York, 1989. pages 26
- [55] W. H. King, *Isotope Shifts in Atomic Spectra*. Plenum Press, 1984. pages 27
- [56] P. Van Duppen and K. Riisager, “Physics with rex-isolde: from experiment to facility,” *Journal of Physics G: Nuclear and Particle Physics*, vol. 38, p. 024005, 2011. pages 29
- [57] A. Herlert, “The isolde facility,” *Nuclear Physics News*, vol. 20, pp. 5–12, 2010. pages 29
- [58] H. Franberg *et al.*, “Off-line commissioning of the isolde cooler,” *Nucl. Instrum. Methods Phys. Res. B*, vol. 266, pp. 4502–4504, 2008. pages 30
- [59] P. Vingerhoets *et al.*, “Nuclear spins, magnetic moments, and quadrupole moments of Cu isotopes from N = 28 to N = 46: Probes for core polarization effects,” *Phys. Rev. C*, vol. 82, p. 064311, 2010. pages 32
- [60] A. Evensen, R. Catherall, P. Drumm, P. V. Duppen, O. Jonsson, E. Kugler, J. Lettry, O. Tengblad, V. Tikhonov, and H. Ravn, “Release and yields from thorium and uranium targets irradiated with a pulsed proton beam,” *Nucl. Instrum. Methods Phys. Res. B*, vol. 126, pp. 160 – 165, 1997. pages 33
- [61] S. Falke, E. Tiemann, C. Lisdat, H. Schnatz, and G. Grosche, “Transition frequencies of the d lines of ^{39}K , ^{40}K , and ^{41}K measured with a femtosecond laser frequency comb,” *Phys. Rev. A*, vol. 74, p. 032503, 2006. pages 38, 53, 54
- [62] F. James, *MINUIT - Function Minimization and Error Analysis*; CERN (1994). pages 38
- [63] M. R. Zaghloul, “On the calcualtion of the voigt line profile: a single proper integral with a damped sine integrand,” *Mon. Not. R. Astron. Soc.*, vol. 375, pp. 1043–1048, 2007. pages 40, 41
- [64] R. J. Wells, “Rapid approximation to the voigt/ feddeeva function and its derivatives,” *Journal of Quantitative Spectroscopy and Radiative Transfer*, vol. 62, pp. 29–48, 1999. pages 41
- [65] T. Ida, M. Ando, and H. Toraya, “Extended pseudo-voigt function for approximating the voigt profile,” *Journal of Applied Crystallography*, vol. 33, pp. 1311–1316, 2000. pages 41

- [66] J. A. Gubner, “A new series for approximating voigt functions,” *J. Phys. A: Math. Gen.*, vol. 27, p. L745, 1994. pages 41
- [67] P. Thompson, D. E. Cox, and J. B. Hastings, “Rietveld refinement of Debys-Scherre synchrotron X-ray data from Al_2O_3 ,” *J. Appl. Cryst.*, vol. 20, pp. 79–83, 1987. pages 41
- [68] K. Kreim, *Collinear Laser Spectroscopy of Potassium, Nuclear Charge Radii beyond $N = 28$* . PhD thesis, Universität Heidelberg, 2014. pages 42, 147
- [69] R. L. Kurucz and B. Bell, “Atomic line data, kurucz cd-rom no. 23. cambridge, mass.: Smithsonian astrophysical observatory,” 1995. <http://www.cfa.harvard.edu/amp/ampdata/kurucz23/sekur.html>. pages 42
- [70] E. A. Phillips, O. Ames, and S. S. Glickstein, “Spin, hyperfine structure, and nuclear magnetic dipole moment of 7.7-min i38k,” *Phys. Rev.*, vol. 138, p. 773, 1965. pages 43, 57, 58
- [71] A. Bohr and V. F. Weisskopf, “The influence of nuclear structure on the hyperfine structure of heavy elements,” *Phys. Rev.*, vol. 77, pp. 94–98, 1950. pages 52, 53, 56
- [72] A. Bohr, “Nuclear magnetic moments and atomic hyperfine structure,” *Phys. Rev.*, vol. 81, p. 331, 1951. pages 52, 54
- [73] J. E. Rosenthal and G. Breit, “The isotope shift in hyperfine structure,” *Phys. Rev.*, vol. 41, pp. 459–470, 1932. pages 53
- [74] H. T. Duong, C. Ekström, M. Gustafsson, T. T. Inimura, P. Juncar, P. Lievens, I. Lindgren, S. Matsuki, T. Murayama, R. Neugart, T. Nilsson, T. Nomura, M. Pellarin, S. Penselin, J. Persson, J. Pinard, I. Ragnarsson, O. Redi, H. H. Stroke, J. L. Vialle, and the ISOLDE Collaboration, “Atomic beam magnetic resonance apparatus for systematic measurement of hyperfine structure anomalies (bohr-weisskopf effect),” *Nucl. Instrum. Methods Phys. Res. B*, vol. 325, pp. 465–474, 1993. pages 53
- [75] F. Bitter, “Nuclear magnetic moments and hyperfine structure of the rubidium isotopes,” *Phys. Rev.*, vol. 75, p. 1326, 1949. pages 53
- [76] V. J. Ehlers, Y. Kabasakal, H. A. Shugart, and O. Tezer, “Hyperfine structure of ^{67}ga and ^{72}ga ,” *Phys. Rev.*, vol. 176, pp. 25–42, 1968. pages 53
- [77] S. Ochs, R. Logan, and P. Kusch, “The h.f.s. anomaly of the potassium isotopes,” *Phys. Rev.*, vol. 78, p. 184, 1950. pages 57, 58

- [78] E. Caurier, G. Martínez-Pinedo, F. Nowacki, A. Poves, and A. P. Zuker, “The shell model as a unified view of nuclear structure,” *Rev. Mod. Phys.*, vol. 77, pp. 427–488, 2005. pages 60, 62
- [79] M. Dufour and A. P. Zuker, “Realistic collective nuclear hamiltonian,” *Phys. Rev. C*, vol. 54, pp. 1641–1660, 1996. pages 60
- [80] F. Nowacki and E. Caurier, “Present status of shell model techniques,” *Acta Physica Polonica B*, vol. 30, pp. 705–714, 1999. pages 62
- [81] W. D. M. Rae, “Nushellx,” 2008. <http://www.garsington.eclipse.co.uk/>. pages 62
- [82] J. Retamosa, E. Caurier, F. Nowacki, and A. Poves, “Shell model study of the neutron-rich nuclei around $N = 28$,” *Phys. Rev. C*, vol. 55, p. 1266, 1997. pages 63
- [83] S. Nummela, P. Baumann, E. Caurier, P. Dessagne, A. Jokinen, A. Knipper, G. Le Scornet, C. Miehé, F. Nowacki, M. Oinonen, Z. Radivojevic, M. Ramdhane, G. Walter, and J. Äystö, “Spectroscopy of $^{34,35}\text{Si}$ by β decay: $sd - fp$ shell gap and single-particle states,” *Phys. Rev. C*, vol. 63, p. 044316, 2001. pages 63
- [84] F. Nowacki and A. Poves, “New effective interaction for $0\hbar\omega$ shell-model calculations in the $sd - pf$ valence space,” *Phys. Rev. C*, vol. 79, p. 014310, Jan 2009. pages 63
- [85] B. Wildenthal, “Empirical strengths of spin operators in nuclei,” *Prog. Part. Nucl. Phys.*, vol. 11, pp. 5–51, 1984. pages 63
- [86] A. Poves and A. Zuker, “Theoretical spectroscopy and the fp shell,” *Phys. Rep.*, vol. 70, pp. 235–314, 1981. pages 63
- [87] S. Kahana, H. C. Lee, and C. K. Scott, “Effect of woods-saxon wave functions on the calculation of $a = 18, 206, 210$ spectra with a realistic interaction,” *Phys. Rev.*, vol. 180, pp. 956–966, 1969. pages 63
- [88] K. Yoro, “Spin-tensor decomposition of effective interaction for 0p shell nuclei,” *Nucl. Phys.*, vol. 333, pp. 67–76, 1980. pages 68
- [89] E. Osnes and D. Strottman, “Spin-tensor analysis of realistic shell model interactions,” *Phys. Rev. C*, vol. 45, pp. 662–670, 1992. pages 68
- [90] B. A. Brown, W. A. Richter, R. E. Julies, and B. H. Wildenthal, “Semi-empirical effective interactions for the 1s-0d shell,” *Ann. Phys. (NY)*, vol. 182, pp. 191–236, 1988. pages 68

- [91] N. A. Smirnova, B. Bally, K. Heyde, F. Nowacki, and K. Sieja, “Shell evolution and nuclear forces,” *Phys. Lett. B*, vol. 686, p. 109, 2010. pages 68
- [92] N. Smirnova, K. Heyde, B. Bally, F. Nowacki, and K. Sieja, “Nuclear shell evolution and in-medium nn interaction,” *Phys. Rev. C*, vol. 86, p. 034314, 2012. pages 68
- [93] A. Umeya and K. Muto, “Triplet-even channel attraction for shell gaps,” *Phys. Rev. C*, vol. 69, p. 024306, 2004. pages 68
- [94] T. Otsuka, T. Suzuki, R. Fujimoto, H. Grawe, and Y. Akaishi, “Evolution of nuclear shells due to the tensor force,” *Phys. Rev. Lett.*, vol. 95, p. 232502, 2005. pages 69, 70
- [95] J. D. Holt, T. Otsuka, A. Schwenk, and T. Suzuki, “Three-body forces and shell structure in calcium isotopes,” *J. Phys. G*, vol. 39, p. 085111, 2012. pages 129
- [96] F. Wienholtz, D. Beck, K. Blaum, Ch. Borgmann, M. Breitenfeldt, R. B. Cakirli, S. George, F. Herfurth, J. D. Holt, M. Kowalska, S. Kreim, D. Lunney, V. Manea, J. Menéndez, D. Neidherr, M. Rosenbusch, L. Schweikhard, A. Schwenk, J. Simonis, J. Stanja, R. N. Wolf, and K. Zuber, “Masses of exotic calcium isotopes pin down nuclear forces,” *Nature*, vol. 498, pp. 346–349, 2013. pages 129
- [97] M. Rosenbusch and ISOLTRAPcollaboration, “Masses of exotic potassium isotopes.” in preparation. pages 129
- [98] R. F. Garcia Ruiz, “Ground-state electromagnetic moments of calcium isotopes.” Submitted to Physical Review C. pages 129
- [99] N. Bendali, H. T. Duong, P. Juncar, J. M. Saint Jalm, and J. L. Vialle, “ $\text{Na}^+ - \text{Na}$ charge exchange processes studied by collinear laser spectroscopy,” *J. Phys. B*, vol. 19, pp. 233–238, 1986. pages 147

FACULTY OF SCIENCE
DEPARTMENT OF PHYSICS AND ASTRONOMY
INSTITUTE FOR NUCLEAR AND RADIATION PHYSICS
Celestijnenlaan 200D box 2418
3001 Leuven

